

A MODEL OF ENERGY AND ANGULAR DISTRIBUTIONS OF FLUXES TO THE
SUBSTRATE AND RESULTING SURFACE TOPOLOGY FOR PLASMA ETCHING
SYSTEMS

BY

ROBERT JOHN HOEKSTRA

B.S., University of Illinois at Urbana-Champaign, 1992
B.S., University of Illinois at Urbana-Champaign, 1992
M.S., University of Illinois at Urbana-Champaign, 1995

THESIS

Submitted in partial fulfillment of the requirements
for the degree of Doctor of Philosophy in Electrical Engineering
in the Graduate College of the
University of Illinois at Urbana-Champaign, 1998

Urbana, Illinois

Red Border Form

A MODEL OF ENERGY AND ANGULAR DISTRIBUTIONS OF FLUXES TO THE SUBSTRATE AND RESULTING SURFACE TOPOLOGY FOR PLASMA ETCHING SYSTEMS

Robert J. Hoekstra, Ph.D.
Department of Electrical and Computer Engineering
University of Illinois at Urbana-Champaign, 1998
M. J. Kushner, Advisor

Plasma etching using high-density plasma (HDP) reactors is becoming predominant in the semiconductor fabrication industry due to its capability to produce highly anisotropic features at current and future linewidths (0.5 to 0.17 μm). The Computational Optical and Discharge Physics Group (CODPG) has developed a modularized computational simulation, the Hybrid Plasma Equipment Model (HPEM), to examine these systems. The two offline modules developed, the Plasma Chemistry Monte Carlo Model (PCMCM) and the Monte Carlo Feature Profile Model (MC-FPM), focus on the effect of the plasma on the wafer surface. Using the output from the main plasma simulation, the PCMCM self-consistently determines the energy and angular distributions of all plasma species at the wafer. This distribution information can then be used by the MC-FPM to determine the time evolution of etch features on the wafer based on an energy- and angular-dependent surface chemistry. This chemistry has been developed using experimental results by other researchers as described in this paper.

An important process in semiconductor manufacturing is the etching of silicon and polysilicon for device fabrication. Chlorine-based chemistries are commonly used in industry today due to the capability of highly anisotropic feature etching allowing the necessary submicron feature production. In current HDP reactors, “microtrench” formation, sidewall slope, and charging effects play an important role in device performance. The MC-FPM has been used to examine the mechanisms, such as specular reflection and energy and angular dependence of etch yield, involved in the shaping of the etch feature. Parameterization of these mechanisms and comparison to experiment have

allowed “cradle-to-grave” (reactor parameters to feature shape) predictive capability with the HPEM, PCMCM, and MC-FPM coupled models for HDP etching processes.

ACKNOWLEDGMENTS

I would like to acknowledge the National Science Foundation (NSF), Semiconductor Research Corporation (SRC), University of Wisconsin Engineering Research Center (ERC) for Plasma Aided Manufacturing, Office of Naval Research, Air Force Office of Scientific Research (AFOSR)/Defense Advanced Research Projects Administration (DARPA) Multidisciplinary University Research Initiative, and Sandia/SEMATECH Cooperative Research Development Agreement (CREDA) on Plasma Modeling.

I would like to thank my advisor, Prof. Mark Kushner, for his great patience and phenomenal understanding of plasma physics, great and small. I am also grateful to all my fellow ODP lab mates through the years: Dr. Mike Grapperhaus, Dr. Eric Keiter, Dr. Shahid Rauf, Ron Kinder, Xudong Xu, Da Zhang, Junqing Lu, Kelly Voyles, Dr. Fred Huang, Dr. Helen Hwang, Dr. Ann Gentile, Dr. Phillip Stout, Dr. Irène Pérès, Dr. Peter Ventzek, Dr. Jong Won Shon, Dr. Seung Choi, Dan Cronin, and last but not least Jean Sexton.

Thanks must also go to Rhonda Reynolds for all the support she has given and Laury Barry who was never satisfied with anything but 100%, and all those others who kept me sane throughout trying times: Diane Kuddoo, Shawn Finrock, Scott Fawley, Mike Malitz, and Rob Liebermann. Of course, I could not forget the wonderful wine group, most notably Tony Curtis, Tom and Lisa Magliery as well as their little ones, Doug Freedman, Milt Epstein, Joyce Bezdicek, and honorary member Adan for reminding me about the good things in life.

Finally, I would like to thank my parents, Ralph and Carol, for all their support even when they doubt my wisdom. They have given me the ability to stand up for myself and not be one of the herd. My sister Mary deserves thanks for her keen sense of what I

am doing wrong. Thanks also to those bundles of unreserved affection, Mandy and Riley,
and to Max whose affection has been much more reserved.

TABLE OF CONTENTS

	Page
1. INTRODUCTION	1
1.1. Plasma Processing	1
1.2. Plasma Etching Research	3
1.3. Plasma Processing Models	5
1.3.1. Plasma models	5
1.3.2. Hybrid Plasma Equipment Model history	6
1.3.3. Topography models	7
1.4. Summary	9
1.5. References	18
2. HYBRID PLASMA EQUIPMENT MODEL	24
2.1. Introduction	24
2.2. Description of Main Modules	25
2.2.1. The electromagnetics module	25
2.2.2. The electron energy transport module	27
2.2.3. The fluid-chemical kinetics simulation	28
2.3. Results for and Inductively Coupled Plasma Etching Reactor	31
2.4. References	36
3. PLASMA CHEMISTRY MONTE CARLO MODEL	37
3.1. Introduction	37
3.2. Description of the Model	37
3.2.1. Computational mesh	38
3.2.2. Particle launch	38
3.2.3. Particle motion	40
3.2.4. Gas phase reactions	41
3.2.5. Surface interactions	44
3.2.6. Collected statistics	47
3.3. Typical Results	47
3.4. References	58
4. MONTE CARLO FEATURE PROFILE MODEL	60
4.1. Introduction	60
4.2. Description of the Model	60
4.2.1. Computational mesh	60
4.2.2. Particle initialization	61
4.2.3. Particle motion	62
4.2.4. Surface interactions	64
4.2.5. Chlorine etching of polysilicon	65
4.3. Typical Results	66
4.3.1. Plasma species flux distributions	67
4.3.2. Predicted etch trench profiles	69
4.4. References	84

5. PROCESSES IN PLASMA ETCHING OF SILICON	85
5.1. Introduction	85
5.2. Specular Reflection	86
5.3. Angular-Dependent Etch Yield	88
5.4. Angular and Energy Dependence of Specular Reflection	88
5.5. Comparison to Experiment	89
5.6. Surface Charging and Perturbation of Feature Evolution	90
5.7. Summary	91
5.8. References	105
6. THREE-DIMENSIONAL FEATURE PROFILE EVOLUTION	106
6.1. Introduction	106
6.2. Description of the Three-Dimensional Model	107
6.3. Profiles for Finite-Length Three-Dimensional Etch Features	108
6.4. Ion Angular Distribution Effects for Finite Length Trenches	111
6.5. Summary	113
6.6. References	123
7. CONCLUSIONS	124
VITA	127

1. INTRODUCTION

1.1. Plasma Processing

As device feature sizes for very large scale integration (VLSI) fabrication continue to decrease to 0.15 μm and below, the processes used to etch these features must continue to improve. This situation has resulted in the industry moving from wet or chemical etching¹ to plasma etching or dry etch processes to meet the demands of the current and future VLSI fabrication. In both etch processes, a photosensitive mask is used to delineate regions of material to be etched to produce semiconductor device features. In wet or chemical etching, the wafer is immersed in a liquid bath which chemically reacts with the exposed surfaces. This type of process produces isotropic etch rates and can lead to dramatic undercutting and broadening of features as shown in Fig. 1.1(a).

An early alternative to chemical etching was sputter removal of material.² By utilizing high energy ion beams (100s-1000s eV), material can be anisotropically removed by physical bombardment. However, for the high energies required to produce large enough etch rates to be industrially feasible, the surface becomes damaged several tenths of microns deep and implantation of the bombarding species leads to high defect and impurity densities. In 1979, Coburn and Winters³ found that a synergistic effect was produced when combining an argon ion beam with a fluorine atom flux from hot XeF_2 gas. The etch rate shown in Fig. 1.2 due to the combined fluxes was an order of magnitude larger than that produced by either individual flux. It was also found by Coburn and Winters that the required activation of the process by the ion flux allowed the anisotropic nature of the sputtering process to be retained. This process was dubbed ion-enhanced etching or reactive ion etching (RIE).⁴⁻⁷

In 1974, Hosokawa *et al.*⁸ found that a fluorine plasma in a parallel plate reactor could be a useful source of both energetic ion fluxes and reactive neutral species when the

wafer was placed on the powered electrode due to the sheath formed near the substrate surface. The sheath is a region near the surface where the high mobile electrons are depleted to form a potential barrier allowing a quasineutral time-averaged flux of charged species to the wall. The potential can be increased further through negative biasing of the surface. This sharp potential gradient, which can be 10s to 100s V over $< 100\text{s } \mu\text{m}$,⁹⁻¹² causes the positive ion flux to maintain a narrow angular distribution¹³ at the wafer leading to anisotropic etching and vertical sidewalls as portrayed in Fig. 1.1(b).

Low-density parallel plate reactors were originally used for plasma etching, however recently high-density plasma (HDP) reactors have been developed. Among the most common HDPs are inductively coupled plasmas (ICP), which are being investigated for use as sources for etching of dielectrics and metals for semiconductor microelectronics fabrication.¹⁴⁻²³ ICP reactors typically operate at low gas pressures ($< 10\text{-}20$ mTorr) and high plasma densities ($10^{11}\text{-}10^{12}$ cm^{-3}) as compared to earlier capacitive systems, which operate at 100s mTorr and produce lower plasma densities ($10^9\text{-}10^{10}$ cm^{-3}). The plasma is generated by either a solenoidal or flat spiral coil, as shown in Fig. 1.3, operated at 100s kHz to 10s MHz. The resulting RF azimuthal electric field produced, which can extend several centimeters into the plasma chamber, accelerates the electrons and thereby deposits power through gas phase collisions between the electrons and the gas. A separate RF bias (a few MHz to 10s MHz) is applied to the substrate to accelerate ions anisotropically into the wafer that is being processed. A feature of this type of reactor is that the magnitude of the ion flux and ion energies incident onto the wafer can, in principle, be separately controlled. The former is determined by the inductively coupled power from the coil. The latter is controlled by the amplitude of the RF bias applied to the substrate. An example of a flat coil ICP reactor is shown in Fig. 1.4. Other HDP sources are available including electron cyclotron resonance²⁴⁻²⁵ (ECR) and helicon²⁶⁻²⁷ sources, but the ICP source is currently the dominant HDP source in the semiconductor industry.

1.2. Plasma Etching Research

After the initial discovery of RIE, the experimental examination of plasma interactions with a semiconductor progressed rapidly. Several gas chemistries have become most prevalent, including fluorine, chlorine, and fluorocarbons as the main components in most etch processes. Initially, fluorine was used for many etch processes but has fallen out of favor for submicron feature etching due to a large thermal etch component.²⁸ Fluorocarbon-containing gases have been used extensively for both silicon and silicon dioxide etching utilizing oxygen²⁹ and hydrogen³⁰ additions to control selectivity. Plumb and Ryan³¹ were the first to propose a comprehensive gas phase reaction mechanism for the CF_4 chemistry. Oehrlein *et al.*³²⁻³⁵ have conducted extensive research based on optical and neutral and ion beam results describing the etching process of silicon and silicon dioxide by fluorocarbons. These competing processes include etching by the fluorine and fluorocarbon ions versus the deposition of a passivating layer of teflon-like material. Sawin *et al.* have also examined the effects of redeposition processes in fluorine-containing plasmas for both silicon and silicon dioxide etching.³⁶⁻³⁷

Chlorine has recently become the gas of choice in silicon and polysilicon etching due to its properties of low thermal etch rate and high ion-enhanced etch rate. BCl_3 can be added to control the production of Cl in the plasma and therefore control the plasma potential³⁸ while addition of HBr limits thermal etch effects such as undercutting as well as the formation of microtrenches.³⁹⁻⁴¹ Extensive examination of the processes involved in chlorine etching of silicon and polysilicon has been ongoing over the last decade to determine the effects of ion/neutral flux ratio, ion energy, and ion angular distribution on the etch process. Coburn proposed that the etch rate in plasma etching can be directly related to the ion/neutral flux ratio impinging on the surface⁴² and demonstrated that relationship for chlorine etching of silicon.⁴³ Dane and Mantei produced an empirical

model based on this relationship as well as the power flux due to the ions.⁴⁴ They were able to closely match experimental etch rates through the use of three fitting parameters. Their model and its use for determination of etch rates for the Plasma Chemistry Monte Carlo Model (PCMCM) are more thoroughly described in Chapter 3.

Two other important factors determining the etch yield by the chlorine ions are impinging energy and angle, which can control both the relative etch rate and shape for profile evolution. Donnelly *et al.*⁴⁵ proposed an energy dependence of $\alpha(E^{1/2}-E_{th}^{1/2})$ where $\alpha = 0.05$ and $E_{th} = 10$ eV based on results of neutral and ion-beam experiments. Balooch *et al.*⁴⁶ and Chang and Sawin⁴⁷ have also shown similar relationships for experiment. However, Manenschijn *et al.* found a linear relationship⁴⁸ for etch yield verses ion energy in a parallel plate reactor. In all of these experiments, the limited number of data points and large ranges of error for measurements make it difficult to determine the exact relationship. Recently, Chang *et al.*^{47,49} have utilized beam experiments to determine the angular dependence of the ion etch yield. They have found that unlike the sputter process, ion-enhanced etching of silicon by chlorine has a maximum yield at normal impinging angles and, beginning at 40°, falls off to zero at 90°. They have also determined that the angular etch yield for silicon dioxide is very similar to sputtering results, and for etching of photoresist the angular dependence falls somewhere in between the former two.⁵⁰ This angular dependence plays an important role in the formation of etch features, as is described in Chapter 5.

1.3. Plasma Processing Models

As plasma processing systems have increased in complexity and cost, it has become prohibitive to develop new reactors by only physical experimentation.

Development of numerical models to simulate these systems has progressed quickly over the last 10 years, allowing predictive capability. Use of these models allows costly physical development and manufacturing to be reduced as seen in almost every technological industry.

1.3.1. Plasma models

Initially, plasma modeling was limited to analytical one-dimensional (1D) models based on limited physics such as drift-diffusion. To become useful as predictive tools, two-dimensional (2D) numerical models are necessary, and the first for examination of RF discharges was developed by Tsai and Wu⁵¹ in 1990. Soon after, Dalvie *et al.*⁵² also produced a drift-diffusion-based 2D model and described the effects of enhanced ionization for large radii in parallel plate systems. Boeuf *et al.*⁵³ also produced a 2D numerical model demonstrating the effects of dc self bias which compared well to experiments for parallel plate plasma systems. Passchier and Goedheer⁵⁴ and Goedheer *et al.*⁵⁵ developed a 2D drift-diffusion model of a parallel plate argon discharge which utilized semi-implicit solutions of Poisson's equation to accelerate solution speed. Lymberopoulos and Economu⁵⁶ developed the first finite element model of a parallel plate system and demonstrated comparison to the Gaseous Electronics Conference (GEC) reference cell. Ventzek *et al.*⁵⁷⁻⁵⁸ produced the first 2D model of inductively coupled discharge and included capacitive coupling effects and later included the effects of momentum for ions and neutrals. Kortshagen *et al.*⁵⁹ developed a model utilizing a nonlocal kinetic model for the electrons and demonstrating the deviation from equilibrium fluid models, while Economu *et al.*⁶⁰ developed the first direct simulation Monte Carlo (DSMC) model of heavy body transport in an HDP system utilizing fluid model results to describe the plasma distributions.

1.3.2. Hybrid Plasma Equipment Model history

Hybrid simulations which include both Monte Carlo and fluid models have been used extensively in modeling plasma systems. Fluid models solved either through finite element or finite difference methods tend to be far faster than Monte Carlo methods, but for very low pressures (< 100 s mTorr) the mean free path becomes comparable to the system dimensions. At this point, the plasma fluid can no longer be considered to be at thermodynamic equilibrium. By using Monte Carlo methods to examine the electron kinetics and/or the heavy body transport, the nonequilibrium effects can be accounted for when coupled with the fluid models.

The Hybrid Plasma Equipment Model (HPEM) was initially developed in 1993 at the University of Illinois by Ventzek *et al.*⁵⁷ as a 2D numerical model which included a fluid module which solved the drift-diffusion equation for charged species and a Monte Carlo module which determined the electron kinetics based on electric fields due to an inductively coupled source. Also in 1993, capacitive coupling of the coils as well as heavy body transport was addressed by the inclusion of an offline fluid transport.⁵⁸ Collison and Kushner⁶¹ included the effects of ion momentum and the interaction of positive and negative ions while Hoekstra *et al.*⁶² developed an offline module, the Plasma Chemistry Monte Carlo Model (PCMCM) described in Chapter 3, to examine the distributions of plasma species fluxes and their interaction with the reactor surfaces. The HPEM was extended to three dimensions in 1996⁶³ allowing examination of innately three-dimensional (3D) effects such as azimuthally asymmetric power deposition or gas flow. Grapperhaus and Kushner⁶⁴ integrated an RF sheath model with the fluid module of the HPEM in 1997 to allow realistic simulation of RF bias application to the substrate. Noncollisional heating of the electrons was incorporated by Rauf and Kushner⁶⁵ in 1998. An offline module, the Monte Carlo Feature Profile Model (MC-FPM) described in Chapter 4, was developed by Hoekstra and Kushner⁶⁶ to self-consistently examine the 2D and 3D feature evolution on

the wafer due to plasma species fluxes. Rauf and Kushner have recently extended the circuit model and external controls to allow nonsinusoidal or multifrequency waveforms as input power⁶⁷ as well as feedback control modeling.⁶⁸

1.3.3. Topography Models

Computational models to describe topography evolution of a surface have been used in many fields. Often two different points of view are taken. The simplest view is that of a bulk material with a boundary with a gas where changes in the surface are determined by piecewise removal or addition to the surface. The other point of view is that of a boundary layer with motion determined by a location-dependent normal velocity or propagation of the surface boundary. In simulation of topography evolution, the first view usually leads to Monte Carlo modeling approaches while the second results in “geometric” or partial differential equation solvers.

One method of topography modeling is often described as the “string” or “geometric” method. For these models, the surface of the feature is represented by nodes attached by straight lines. The motion of the nodes is then determined by semi-empirically determined analytic formulae which relate the flux properties at the surface to a normal velocity for the node. One model of this type is SPEEDIE, developed by Ulacia and McVittie⁶⁹ as well as Singh *et al.*⁷⁰, which has been used to examine etching and deposition related to metallization processes in VLSI fabrication. SPEEDIE originally utilized Monte Carlo methods to determine fluxes at the surface and calculate nodal motion and has been used to examine the relative importance of surface reemission in SiO₂ chemical vapor deposition. In 1991, Islamraja *et al.*⁷¹ included the capability of producing analytic expressions for surface fluxes based on radiative heat transfer equations. A comparison of experimental scanning electron microscope (SEM) images of etching of overhang test structures to SPEEDIE simulation¹⁹ results is shown in Fig. 1.4. Another

model of this type, EVOLVE, developed by Cale *et al.*⁷² has also shown the capability to simulate deposition in VLSI fabrication.

Solution of partial differential equations (PDEs) which determine the surface motion have also been used in topography models. As in the string method, it is necessary to calculate a normal velocity at all points along the surface. Finite difference methods are generally used to solve a PDE which describes the motion of the surface. The first form of the models were based on the method of characteristics which requires that the normal velocity of the surface is independent of the properties of the surface such as curvature. The method of characteristic was first used by Ross⁷³ in 1988 to simulate profile evolution for sputtering while Shaqfeh and Jurgensen⁷⁴ used the method to examine the effects of mask erosion during plasma processing. Abraham-Shrauner⁷⁵ has utilized the method of characteristics to examine ion flux-limited versus neutral flux-limited regimes for a generalized etch process results for which are shown in Fig. 1.5. Hamaguchi *et al.*⁷⁶⁻⁷⁷ developed a shock tracking method which allowed treatment of sharp corners as shocks through the use of diffusive velocity profiles to control their propagation. An important method which allows treatment of these effects by embedding the surface in a higher-dimensional function is the level set method developed by Osher and Sethian.⁷⁸ By solving the PDE for a higher-dimensional function, the lower-dimensional discontinuities do not develop in the solution. Diffusive effects to alleviate these discontinuities can also be included by utilizing a curvature-dependent velocity for the surface motion. Utilization of the level set method for feature-scale modeling of semiconductor processes including etching, deposition, and lithography has been demonstrated⁷⁹⁻⁸⁰ and are shown in Fig. 1.6.

Monte Carlo methods for feature-scale simulation are the most straightforward methods of modeling topography. Tracking particles and interacting them with a surface grid based on a reactive coefficient scheme allows a very direct translation of the physical system to a model. There are negative aspects to these methods, however, most notably

very long simulation times and statistical noise, which are inversely related. A benefit of these methods is the capability to easily integrate new physical processes in the model, whereas the earlier described string and PDE methods require much greater finesse and time to develop velocity functions to account for new processes. In 1988, Cotler *et al.*⁸¹ developed a Monte Carlo topography model to examine argon ion sputtering of silicon and later extended the model to include chemical processes to compare physical, chemical, and physically enhanced chemical processes.⁸² May *et al.*⁸³ developed a sputter etch topography model for argon impinging on silicon showing the effects of ion angular distribution on trench undercutting. Chang *et al.*⁸⁴ and Marowala *et al.*⁸⁵ have developed a similar model to the MC-FPM described in this paper which models chlorine etching of polysilicon using reaction rates based on ion/neutral flux ratios and analytically derived species flux distributions. The MC-FPM also models chlorine etching of polysilicon including energy and angular dependent etch rates and utilizes flux distributions produced by the HPEM, allowing direct determination of feature evolution for given plasma reactor input parameters. Recently, Hwang and Giapis⁸⁶⁻⁸⁸ have reported on results for their model of the effects of nonuniform charging within etch feature profiles and the development of horizontal “notch” formation using a parallel Monte Carlo algorithm.

1.4. Summary

In Chapter 2, a brief description of the HPEM is presented to allow full explanation of the coupled nature of the plasma processing models in this paper. The hybrid composition of the model, allowing full description of nonequilibrium plasma systems such as high-density ICP reactors, is described and example results for a flat coil configuration are presented.

In Chapter 3, the PCMCM is described indicating the use of Monte Carlo techniques and the coupling with the HPEM to allow self-consistent determination of the

energy and angular distributions of plasma species fluxes at the wafer. Particle energy and angular distributions are presented for a flat coil geometry with a chlorine etch process as well as radially dependent etch rate calculations based on Dane and Mantei's model⁴⁴ for variation of input parameters such as ICP power, RF bias power, and pressure.

Chapter 4 describes the MC-FPM, which allows self-consistent determination of feature profile evolution in plasma processing utilizing the results of the PCMCM. Results demonstrating the effect of subwafer and superwafer topography, such as backside cooling channels and wafer clamps, are shown for chlorine etching of infinite trench features utilizing the 2D version of the MC-FPM. The perturbation of the incoming energy and angular distributions of the ion fluxes results in asymmetrical features as well as a decrease in the effective etch rate.

Chapter 5 describes the effects of the processes involved in chlorine etching of silicon and the resulting feature evolution. The energy and angular dependence of etch yield show dramatic effects on the resulting shape of the feature as well as on the rate of etching. The development of "microtrenches" at the corners of trench features is explored indicating the contribution of specular reflection of ions from feature sidewalls. Initial determination of the effects of nonuniform flux of charged species on the feature surface is presented with respect to the development of potential differences within the feature and the resulting perturbation of the charged species path and feature evolution.

In Chapter 6, the 3D extension of the MC-FPM is presented indicating the necessity of 3D models to describe the evolution of finite-length trenches and other finite features. The "three-plane" corners of these features show the greatest deviation from the results of the 2D model.

In Chapter 7, conclusions are made about the overall significance of the work and recommendations for future work are discussed.

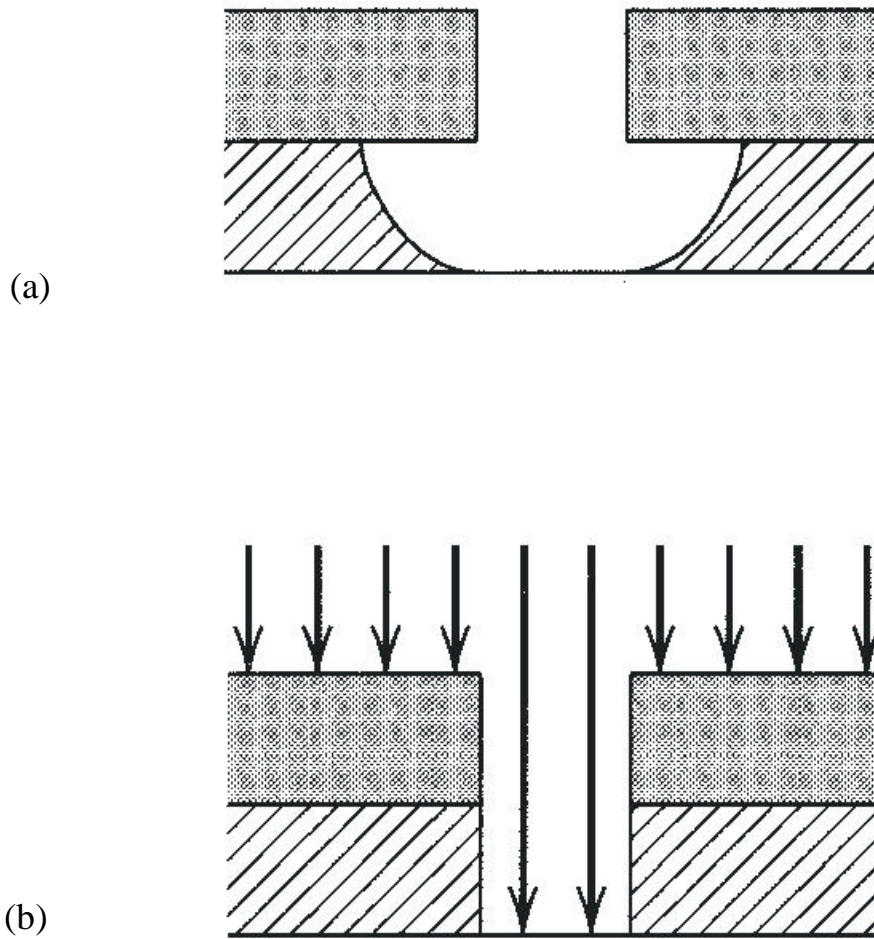


Fig 1.1. Etched profiles indicative of (a) wet or chemical etching and (b) dry or plasma etching.

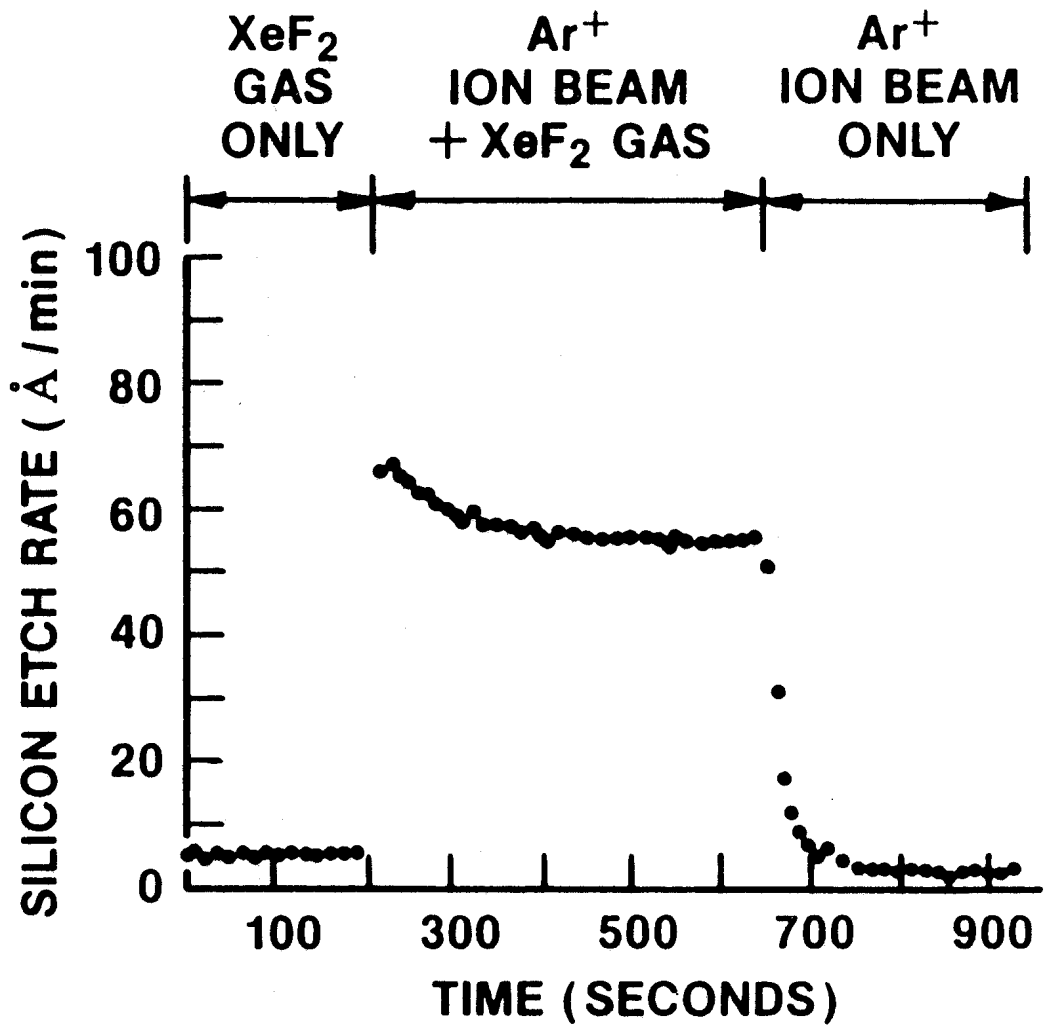


Fig. 1.2. Experimental results for ion-enhanced plasma etching (Coburn and Winters,³ 1979).

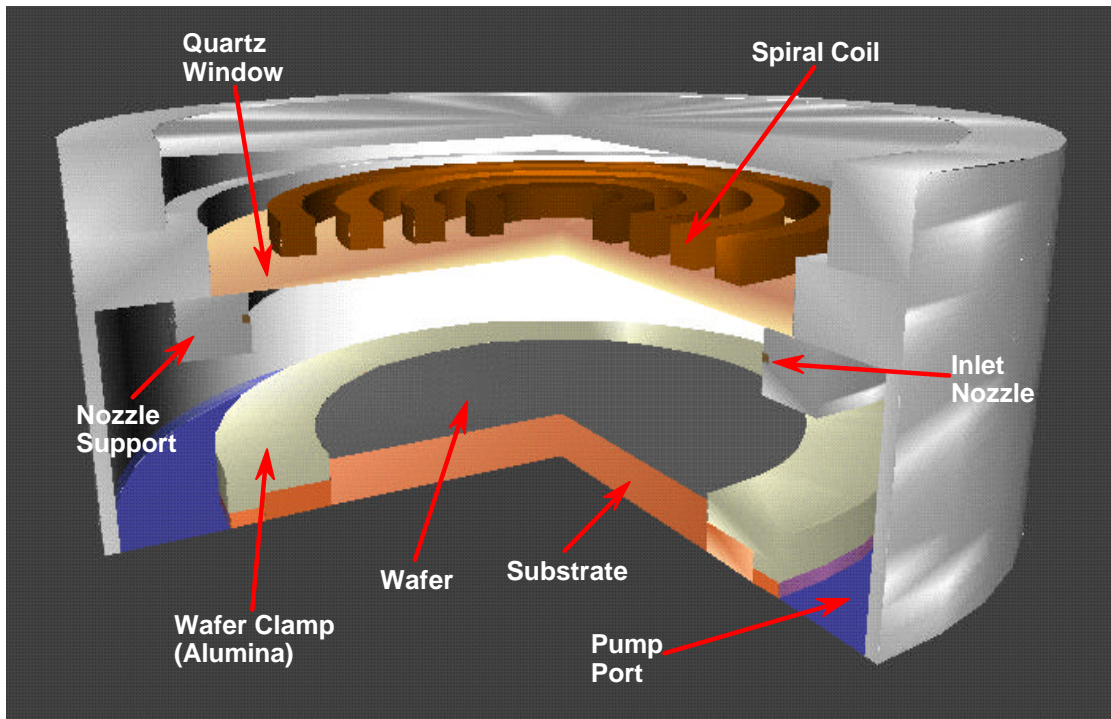
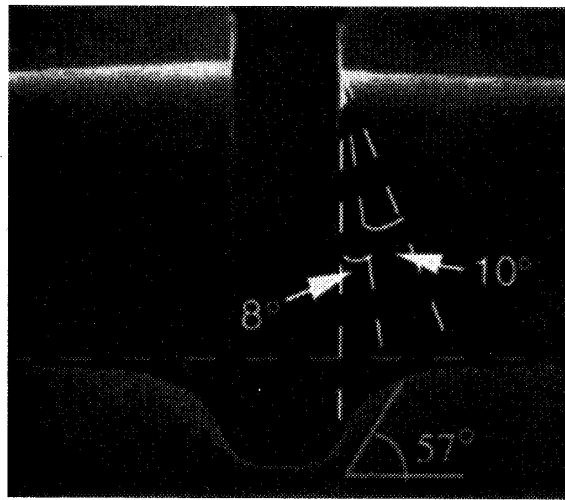
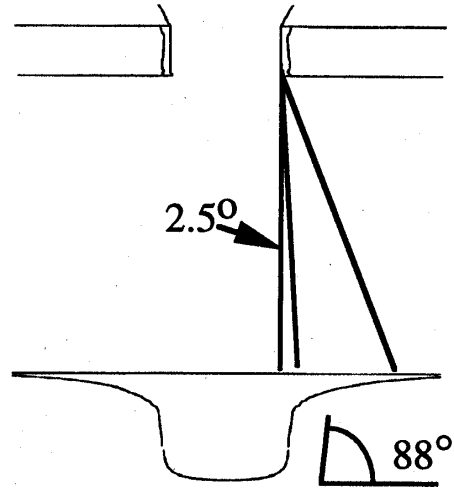


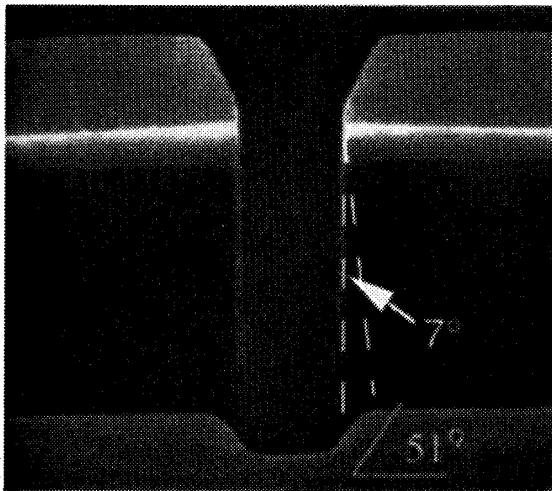
Fig 1.3. Three-dimensional representation of a planar coil inductively coupled plasma reactor.



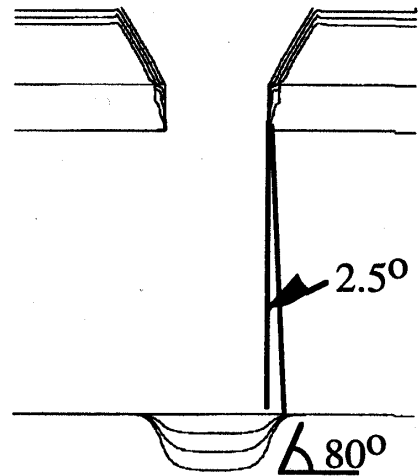
(a) 2 μm



(c)



(b) 2 μm



(d)

Fig. 1.4. Comparison of SEM overhang etch structures with SPEEDIE model results for (a,c) 100-mTorr parallel plate and (b,d) 7-mTorr ICP etching (Zheng *et al.*,⁷¹ 1995).

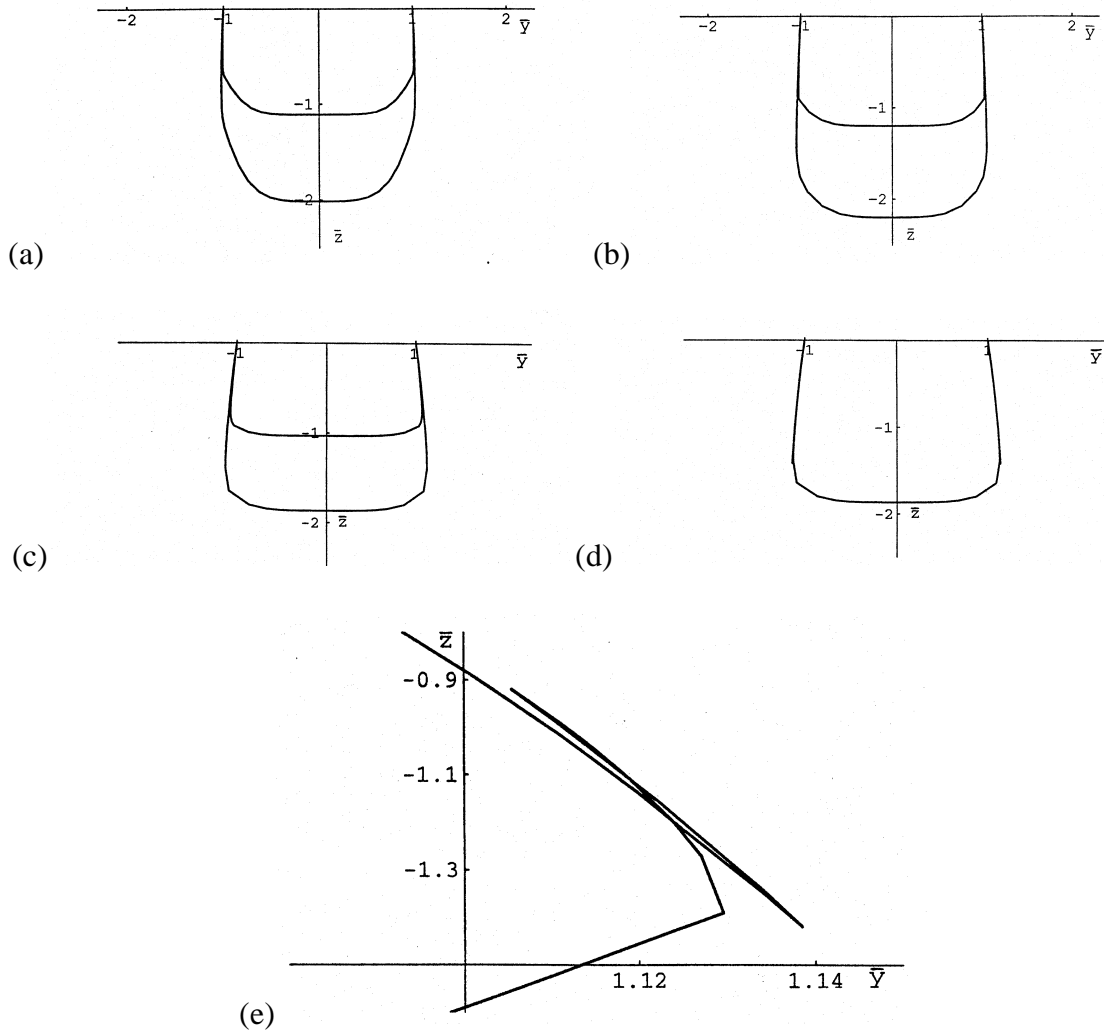


Fig. 1.5. Method of characteristics simulation results for increasing anisotropic ion etch rate to isotropic neutral etch rate ratio from (a) 1:5 to (b) 1:1 to (c) 5:1. For the 5:1 etch profile (d) looping occurs. (e) An enlarged view of the looping (Abraham-Shrauner,⁷⁶ 1997).

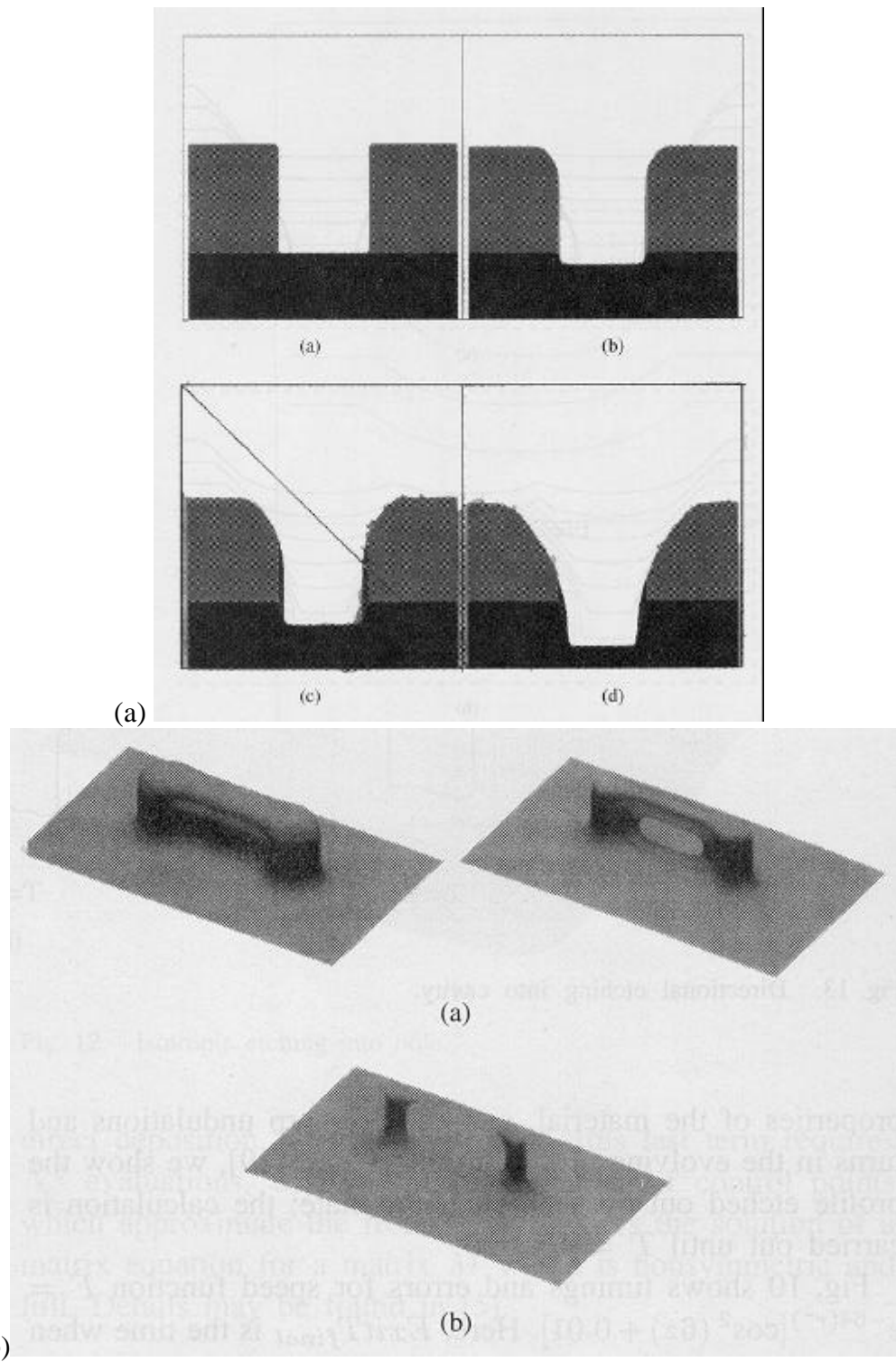


Fig. 1.6. Examples of (a) 2-dimensional and (b) 3-dimensional etch simulation results using the level set method (Sethian and Adalsteinsson,⁸¹ 1997).

1.5. References

1. J. Hopwood, *Plasma Sources Sci. Technol.* **1**, 109 (1992).
2. R. Frerichs and C. J. Kircher, *J. Appl. Phys.* **36**, 3541 (1963).
3. J. W. Colburn and H. F. Winters, *J. Appl. Phys.* **50**, 3189 (1979).
4. J. Keller, M. S. Barnes, and J. C. Forster, 42th Gaseous Electronics Conference, paper NA-5, Urbana, IL, 1990.
5. J. H. Keller, J. C. Forster, and M. S. Barnes, *J. Vac. Sci. Technol. A* **11**, 2487 (1993).
6. M. S. Barnes, J.C. Forster, and J. H. Keller, *Appl. Phys. Lett.* **62**, 2622 (1993).
7. J. A. O'Neill, M. S. Barnes, and J. H. Keller, *J. Appl. Phys.* **73**, 1621 (1993).
8. N. Hosokawa, R. Matsuzaki, and T. Asamaki, *Jpn. J. Appl. Phys. Suppl.* **2**, 435 (1974).
9. M. A. Lieberman, *IEEE Trans. Plasma Sci.* **16**, 638 (1988).
10. V. A. Godyak and N. Sternberg, *IEEE Trans. Plasma Sci.* **18**, 159 (1990).
11. K. Börnig, *Appl. Phys. Lett.* **60**, 1553 (1992).
12. N. Sternberg and V. A. Godyak, *IEEE Trans. Mag.* **30**, 3100 (1994).
13. R. Patrick, R. Schoenborn, and H. Toda, *J. Vac. Sci. Technol. A* **11**, 1296 (1993).
14. J. B. Carter, J.P. Holland, E. Peltzer, B. Richardson, E. Bogle, H. T. Nguyen, Y. Melaku, D. Gates, and M. Ben-Dor, *J. Vac. Sci. Technol. B* **11**, 1301 (1993).
15. Y. Ra, S. G. Bradley, and C.-H. Chen, *J. Vac. Sci. Technol. A*, **12**, 1328 (1994).
16. D. F. Beale, A. E. Wendt, and L. J. Mahoney, *J. Vac. Sci. Technol. A* **12**, 2775 (1994).

17. J. Hopwood, Appl. Phys. Lett. **62**, 940 (1993).
18. U. Kortshagen, Plasma Sci. Sources Technol. **4**, 172 (1995).
19. J. Zheng, R. P. Brinkman, and J. P. McVittie, J. Vac. Sci. Technol. A **13**, 859 (1995).
20. J. Caughman, Proceedings of the 41st National Symposium of the American Vacuum Society, Denver, CO, October 1994, paper PS-MoP5.
21. J. R. Woodworth, M. E. Riley, P. A. Riley, and G. A. Hebner, J. Appl. Phys. **81**, 5950 (1997).
22. A. Manenschijn and W. J. Goedheer, J. Appl. Phys. **69**, 2923 (1991).
23. M. J. Kushner, J. Appl. Phys. **58**, 4024 (1985).
24. J. Asmussen, J. Vac. Sci. Technol. A **7**, 883 (1989).
25. J. Asmussen, T. A. Grotjohn, P. Mak, and J. Perrin, IEEE Trans. Plasma Sci. **25**, 1196 (1997)
26. R. W. Boswell and F. F. Chen, IEEE Trans. Plasma Sci. **25**, 1229 (1997).
27. F. F. Chen and R. W. Boswell, IEEE Trans. Plasma Sci. **25**, 1245 (1997).
28. M. A. Lieberman and A. J. Lichtenberg, *Principles of Plasma Discharges and Materials Processing* (John Wiley and Sons, New York, 1994).
29. P. Gadgil, D. Dane, and T. D. Mantei, J. Vac. Sci. Technol. A **10**, 1303 (1992).
30. M. Kimizuka and Y. Ozaki, J. Vac. Sci. Technol. B **15**, 221 (1997).
31. I. C. Plumb and R. K. Ryan, Plasma Chem. Plasma Process **6**, 205 (1986).
32. J. P. Simko and G. S. Oehrlein, J. Electrochem. Soc. **138**, 2748 (1991).
33. G. S. Oehrlein, Y. Zhang, D. Vender, and M. Haverlag, J. Vac. Sci. Technol. A **12**, 323 (1994).
34. G. S. Oehrlein, Y. Zhang, D. Vender, and O. Joubert, J. Vac. Sci. Technol. A **12**, 333 (1994).

35. T. E. F. M. Standaert, M. Schaepkens, N. R. Rueger, P. G. M. Sebel, G. S. Oehrleing, and J. M Cook, *J. Vac. Sci. Technol. A* **16**, 239 (1998).
36. D. C. Gray, H. H. Sawin, and J. W. Butterbaugh, *J. Vac. Sci. Technol. A* **9**, 779 (1991).
37. J. W. Butterbaugh, D. C. Gray, and H. H. Sawin, *J. Vac. Sci. Technol. B* **9**, 1461 (1991).
38. C. B. Fleddermann and G. A. Hebner, *J. Vac. Sci. Technol. A* **15**, 1955 (1997).
39. D. X. Ma, T. A. Lin, and C. H. Chen, *J. Vac. Sci. Technol. A* **10**, 1217 (1992).
40. L. Y. Tsou, *J. Electrochem. Soc.* **136**, 3003 (1989).
41. C. C. Cheng, K. V. Guinn, and V. M. Donnelly, *J. Vac. Sci. Technol. B* **13**, 1970 (1995).
42. J. W. Coburn, *J. Vac. Sci. Technol. A* **12**, 1417 (1994).
43. J. W. Coburn, *J. Vac. Sci. Technol. B* **12**, 1384 (1994).
44. D. Dane and T. D. Mantei, *Appl. Phys. Lett.* **65**, 478 (1994).
45. C. C. Cheng, K. V. Guinn, V. M. Donnelly, and I. P. Herman, *J. Vac. Sci. Technol. A* **12**, 2630 (1994).
46. M. Balooch, M. Moalem, Wei-E. Wang, and A. V. Hamza, *J. Vac. Sci. Technol. A* **14**, 229 (1996).
47. J. P. Chang and H. H. Sawin, *J. Vac. Sci. Technol. A* **15**, 610 (1997).
48. A. Manenschijn, E. van der Drift, G. G. A. M. Janssen, and S. Radelaar, *J. Appl. Phys.* **69**, 7996 (1991).
49. J. P. Chang, J. C. Arnold, G. C. H Zau, H.-S. Shin, and H. H. Sawin, *J. Vac. Sci. Technol. A* **15**, 1853 (1997).

50. J. P. Chang and H. H. Sawin, 44th Annual Symposium of the American Vacuum Society (San Jose, October 1997), paper PS-ThA1.
51. J. H. Tsai and C. Wu, Phys. Rev. A **41**, 5626 (1990).
52. M. Dalvie, M. Surendra, and G. S. Selwyn, Appl. Phys. Lett. **62**, 3207 (1993).
53. J. P. Boeuf, L. C. Pitchford, A. Fiala, and Ph. Belenguer, Surf. And Coat. Technol. **59**, 32 (1993).
54. J. D. P. Passchier and W. J. Goedheer, J. Appl. Phys. **74**, 3744 (1993).
55. W. J. Goedheer, P. M. Meijer, J. Bezemer, J. Diederick, P. Passchier, and W. G. H. M. van Sark, IEEE Trans. Plasma Sci. **23**, 644 (1995)
56. D. P. Lymberopoulos and D. J. Economou, Appl. Phys. Lett. **63**, 2478 (1993).
57. P. L. G. Ventzek, T. J. Sommerer, R. J. Hoekstra, and M. J. Kushner, Appl. Phys. Lett. **63**, 605 (1993).
58. P. L. G. Ventzek, R. J. Hoekstra, and M. J. Kushner, J. Vac. Sci. Technol. B **12**, 461 (1993).
59. U. Kortshagen, I. Pukropski, and L. D. Tsendin, Phys. Rev. E **51**, 6063 (1995).
60. D. J. Economou, T. J. Bartel, R. S. Wise, and D. P. Lymberopoulos, IEEE Trans. Plasma Sci. **23**, 581 (1995).
61. W. Z. Collison and M. J. Kushner, Appl. Phys. Lett. **68**, 903 (1996).
62. R. J. Hoekstra and M. J. Kushner, J. Appl. Phys. **79**, 2275 (1995).
63. M. J. Kushner, W. Z. Collison, M. J. Grapperhaus, J. P. Holland, and M. S. Barnes, J. Appl. Phys. **80**, 1337 (1996).
64. M. J. Grapperhaus and M. J. Kushner, J. Appl. Phys. **81**, 569 (1997).
65. S. Rauf and M. J. Kushner, J. Appl. Phys. **81**, 5966 (1997).

66. R. J. Hoekstra and M. J. Kushner, *J. Vac. Sci. Technol. A* **15**, 1913 (1997).
67. S. Rauf and M. J. Kushner, *J. Appl. Phys.* **83**, 5087 (1998).
68. S. Rauf and M. J. Kushner, *IEEE Trans. Semiconduct. Manufact.* **11**, 486 (1998).
69. J. I. Ulacia and J. P. McVittie, *J. Appl. Phys.* **65**, 1484 (1989).
70. V. K. Singh, E. S. G. Shaqfeh, and J. P. McVittie, *J. Vac. Sci. Technol. B* **10**, 1091 (1992).
71. M. M. Islamraja, M. A. Cappelli, J. P. McVittie, and K. C. Saraswat, *J. Appl. Phys.* **70**, 7137 (1991).
72. T. S. Cale, G. B. Raupp, and T. H. Gandy, *J. Appl. Phys.* **68**, 3645 (1990).
73. D. S. Ross, *J. Electrochem. Soc.* **135**, 1260 (1988).
74. E. S. G. Shaqfeh and C. W. Jurgensen, *J. Appl. Phys.* **66**, 4664 (1989).
75. B. Abraham-Strauner, *IEEE Trans. Plasma Sci.* **25**, 433 (1997).
76. S. Hamaguchi, M. Dalvie, R. T. Farouki, and S. Sethuraman, *J. Appl. Phys.* **74**, 5172 (1993).
77. S. Hamaguchi and M. Dalvie, *J. Vac. Sci. Technol. A* **12**, 2745 (1994).
78. S. Osher and J. A. Sethian, *J. Comp. Phys.* **79**, 12 (1988).
79. D. Adalsteinsson and J. A. Sethian, *J. Comp. Phys.* **120**, 128 (1995).
80. J. A. Sethian and D. Adalsteinsson, *IEEE Trans. Semiconduct. Manufact.* **10**, 167, (1997).
81. T. J. Colter, M. S. Barnes, and M. E. Elta, *J. Vac. Sci. Technol. B* **6**, 542 (1988).
82. T. J. Colter and M. E. Elta, *J. Vac. Sci. Technol. B* **8**, 523 (1990).
83. P. W. May, D. Field, and D. F. Klemperer, *J. Phys. D* **26**, 598 (1993).
84. J. P. Chang, A. P. Mahorowala, and H. H. Sawin, *J. Vac. Sci. Technol. A* **16**, 217 (1997).

85. A. P. Mahorowala, J. P. Chang, and H. H. Sawin, 44th Annual Symposium of the American Vacuum Society (San Jose, October 1997), paper PS-MoA5.
86. G. S. Hwang and K. P. Giapis, *J. Appl. Phys.* **82**, 572 (1997).
87. G. S. Hwang and K. P. Giapis, *J. Vac. Sci. Technol. B* **15**, 70 (1997).
88. G. S. Hwang and K. P. Giapis, *Appl. Phys. Lett.* **71**, 2928 (1997).

2. HYBRID PLASMA EQUIPMENT MODEL

2.1. Introduction

The Hybrid Plasma Equipment Model (HPEM) has been developed by the Computational Optical and Discharge Physics Group (CODPG) to numerically investigate plasma processing reactors in two and three dimensions.¹⁻¹⁴ The HPEM is composed of a series of coupled modules which are iterated to reach a converged steady-state solution based on input parameters. In this chapter, an overview of the main body of the HPEM will be given to introduce a basis for the offline models produced for this thesis as well as to describe the production of input for those models. A schematic of the modules which make up the HPEM is shown in Fig 2.1.

The HPEM's main loop is made up of three general modules: the electromagnetics module (EMM), the electron energy transport module (EETM), and the fluid-chemical kinetics simulation (FKS), as well as several supporting modules which interact with one of the main modules. The EMM calculates inductively coupled electric and magnetic fields as well as static magnetic fields caused by the inductive coils and permanent magnets or dc currents respectively. The EETM spatially resolves the electron energy transport by either solving the electron energy conservation equation or using a Monte Carlo simulation to track electron trajectories over many RF cycles to generate the spatially-dependent electron energy distribution functions (EEDFs). Finally, the FKS solves the continuity and momentum equations coupled with Poisson's equation to determine the spatially dependent density of charged and neutral species as well as electrostatic fields. The coupling between the modules occurs through the following. The fields produced by the EMM and FKS are used in the EETM while the EEDFs produced by the EETM are used to calculate electron impact source functions for the FKS. Finally, the spatial density distributions produced by the FKS are used to calculate the conductivity for the EMM.

The modules not included in the main loop include: the Plasma Chemistry Monte Carlo Model (PCMCM), the Monte Carlo Feature Profile Model (MC-FPM), the particle contamination modules,¹¹⁻¹² the surface kinetics module,¹³ and the Virtual Plasma Equipment Model¹⁴ (VPEM), which allows realistic simulation of the power systems and possible process control systems surrounding the tool. The PCMCM and MC-FPM are used to produce more detail concerning the flux distributions and their effect on surface topology and are described in greater detail in Chapters 3-5

2.2. Description of Main Modules

As mentioned in the proceeding section, the HPEM is made of three main modules: the electromagnetics module (EMM), the electron energy transport module (EETM), and the fluid-chemical kinetics simulation (FKS). The following subsections will give an overview of each module.

2.2.1. The electromagnetics module

The Electromagnetics module determines both the azimuthal electric fields due to the inductively coupled coils and the radial and axial magnetic fields due to permanent magnets or quasistatic current loops. To determine the time harmonic azimuthal fields, Maxwell's equation for electric fields is solved under time harmonic conditions and for the azimuthal direction only:

$$-\nabla \cdot \frac{1}{\mathbf{m}} \nabla E_f = \mathbf{w}^2 \mathbf{e} E_f - j \mathbf{w} J_f \quad (2.1)$$

where \mathbf{m} indicates the material permeability, E_f indicates the time harmonic azimuthal field, \mathbf{w} is the frequency of the driving current, \mathbf{e} is the permittivity, and J_f is the total current

due to the driving current and the conduction current, where the conduction current is assumed to be $J_{cf} = \sigma E_f$ where σ is the conductivity. The conductivity is determined either by the collisional approximation of

$$\mathbf{S} = \frac{q_e^2 n_e}{m_e} \frac{1}{\mathbf{n}_{me} + i\omega} \quad (2.2)$$

or calculated from the electron currents and electric fields in the FKS. The azimuthal electric field solution is determined by the iterative method of successive overrelaxation (SOR) where convergence is assumed when the relative change is less than 10^{-6} .

The static magnetic fields in the axial and radial directions are also determined in the EMM. Assuming azimuthal symmetry allows the magnetic field to be represented by a vector potential \mathbf{A} with only an azimuthal component. \mathbf{A} can be solved using

$$\nabla \times \frac{1}{m} \nabla \times \mathbf{A} = \mathbf{j} \quad \text{where} \quad \mathbf{B} = \nabla \times \mathbf{A}, \quad (2.3)$$

where j is the source terms due to closed current loops at mesh points representing permanent magnets. This equation is also solved using SOR.

A circuit module (CM) is included in the EMM which models a matchbox circuit as well as the coils. The impedance of the matchbox is matched to the coil impedance allowing the deposited power to be maximized. The source voltage is also adjusted from iteration to iteration allowing the power specified by the input file to be matched and maintained.

2.2.2. The electron energy transport module

The HPEM determines distribution properties of the electrons by one of two methods. The first of these methods is by solution of the electron energy conservation equation in the electron energy equation module (EEEM). The other method utilizes Monte Carlo techniques to launch electron particles and collect statistics in the electron Monte Carlo simulation (EMCS).

The EEEM solves the zero-dimensional Boltzmann equation for a range of E/N , electric field divided by plasma density, to tabulate the EEDFs over this range and allow the determination of electron transport properties. This information is used in the solution of the electron energy equation

$$\nabla k \nabla T_e + \nabla \cdot (\mathbf{G} T_e) = P_{heating} - P_{loss}, \quad (2.4)$$

where k is the thermal conductivity, \mathbf{G} is the electron flux determined by the FKS, T_e is the electron temperature equal to three halves the average energy determined from the EEDF, $P_{heating}$ is the power added due to conductive heating equal to $\mathbf{sE} \cdot \mathbf{E}$ where the conductivity is determined in the FKS and the electric field is the sum of the azimuthal field from the EMM and the radial and axial field found in the FKS, and the P_{loss} is the power loss due to collisions by the electrons. Inclusion of the thermal conductivity allows determination of the spatial distribution of the electron energy under thermodynamic equilibrium.

The alternative EMCS calculates the electron transport and energy distribution properties utilizing a Monte Carlo method by releasing and statistically tracking electron pseudoparticles. A few thousand pseudoparticles are released with a Maxwellian velocity distribution and spatially distributed according to the distribution of the electron density

determined in the FKS. The particles are moved under a Lorentzian force due to the time-dependent electric and static magnetic fields using a second-order predictor corrector or leap-frog method. Collision rates are determined by calculating the sum of the maximum rates of all possible collisions and using the null collision method to adjust for the specific energy-dependent collision rate. The particles are statistically tracked to determine the spatial distribution of the total collision frequency, the electron temperature, and the reaction-specific electron impact rate coefficients based on the convolution of the energy-dependent cross section with the EEDF at the specified location.

2.2.3. The fluid-chemical kinetics simulation

In the FKS, the continuum transport equations for the gas species are solved simultaneously with the electrostatic potential to determine the spatial distribution of species densities as well as the momentum flux fields within the reactor. For electron transport, the drift-diffusion equation is solved while for the ion transport, the effects of momentum and energy transport can be included. Neutral species transport can be included through Navier-Stokes momentum and energy equations as well. To self-consistently consider the electrostatic fields, either Poisson's equation can be included, or quasineutrality allowing ambipolar fields can be assumed.

The continuity equation for all species is

$$\frac{\partial N_i}{\partial t} = -\nabla \cdot \mathbf{\Gamma}_i + S_i, \quad (2.5)$$

which can be used to solve for the species densities where \mathbf{G}_i and S_i are the respective fluxes and sources for species i . The source terms are determined by the electron impact

collision rates produced by the EEDFM and “heavy-body” interactions based on user input reaction rates.

The electron flux \mathbf{G}_i is determined by the drift diffusion equation

$$\Gamma_i = \mathbf{m}_i q_i N_i \mathbf{E} - D_i \nabla N_i, \quad (2.6)$$

where \mathbf{m}_i is the mobility (including the effects the magnetostatic fields), q_i is the charge, N_i is the density, and D_i is the diffusion coefficient for species i . The ion and neutral flux calculation can be calculated using the drift diffusion equation or by including the effects of momentum by the replacement of the diffusional term with terms for pressure, advection, and collisionality:

$$\frac{\partial \Gamma_i}{\partial t} = -\frac{1}{m_i} \nabla \cdot (N_i k_i T_i) + \nabla \cdot \bar{\boldsymbol{\tau}} - \nabla \cdot (N_i \mathbf{v}_i) + \frac{q_i}{m_i} N_i \mathbf{E} - \sum_j \frac{m_j}{m_i + m_j} N_i N_j (\mathbf{v}_i - \mathbf{v}_j) \mathbf{n}_{ij}. \quad (2.7)$$

For this equation, m_i , k_i , T_i , and \mathbf{v}_i indicate the mass, thermal conductivity, temperature, and velocity \mathbf{G}_i/N_i , respectively, for species i , while m_j , N_j , and \mathbf{v}_j indicate the mass, density, and velocity, respectively, of the collision partner j with a collision frequency of \mathbf{n}_{ij} . The viscosity $\bar{\boldsymbol{\tau}}$ is included for neutrals only.

Determination of the time-dependent electrostatic fields is accomplished either by solution of Poisson’s equation or based on quasineutrality allowing an ambipolar field approximation to be applied. The solution of Poisson’s equation is calculated semi-implicitly by approximating the charge density \mathbf{r} at time $t+\Delta t$ linearly as

$$\mathbf{r}^{t+\Delta t} = \mathbf{r}^t + \Delta t \left. \frac{\partial \mathbf{r}}{\partial t} \right|^{t,t+\Delta t}; \quad \left. \frac{\partial \mathbf{r}}{\partial t} \right|^{t,t+\Delta t} = -\nabla \cdot \mathbf{j}^{t,t+\Delta t} \quad (2.8)$$

where \mathbf{j} is the total current density equal to $\sum_i q_i \Gamma_i^{t, t+\Delta t}$ for all charged species in the plasma region and equal to $\sigma \nabla \phi^{t+\Delta t}$ for all other regions. The species flux terms come from either the drift diffusion equation or the momentum equation with the electric field replaced by $\nabla \phi^{t+\Delta t}$, producing the implicit nature of the solution while the species densities and temperatures are used at time t . By making the potential fully implicit in this scheme while using explicit terms for the assumedly more slowly varying species properties such as density and temperature, the time step used in the SOR solution can be lengthened beyond the dielectric relaxation time and greatly accelerate solution over the fully explicit formulation.

To accelerate the electrostatic calculation further, an ambipolar field approximation has also been implemented.¹⁰ If it is assumed that the plasma is quasi-neutral at all locations, the electron density can be set equal to the total ion density at all locations. To maintain this charge neutrality requires that

$$-(\nabla \cdot \Gamma_e + S_e) = \sum_i q_i \left[\nabla \cdot \Gamma_i + S_i \right], \quad (2.9)$$

where S_e and S_i are the electron and ion sources, respectively, due to both internal and external sources such as electron beams. The flux terms are replaced by their drift diffusion approximations and the terms are rearranged to get

$$\nabla \cdot \sum_j \left(q_j^2 \mathbf{m}_j N_j \right) \nabla \phi = \nabla \cdot \sum_j \left(q_j D_j \nabla N_j \right) + \sum_j q_j S_j, \quad (2.10)$$

where the summations are taken over all charged species including both electrons and ions. By reducing the system to a steady-state solution, the dielectric relaxation time is removed as a limit allowing much larger timesteps to be taken, only limited by the Courant limit.

A semianalytic sheath model⁷ (SM) has also been integrated with the FKS to more realistically represent the fields and fluxes at gas-solid boundaries under conditions where the actual sheath thickness is less than the mesh spacing. The sheath model tracks the charging and discharging of the sheath during the RF cycle assuming collisionless transversal by the ions through the sheath and a Boltzmann distribution for the electrons. A multispecies form of Riley's unified sheath model¹⁵ is used to relate the sheath charge Q and boundary conditions to the potential drop. This potential drop across the sheath produced by the semianalytic sheath model is then applied as a jump condition at plasma-wall boundaries in solving Poisson's equation for the entire reactor.

2.3. Results for an Inductively Coupled Plasma Etching Reactor

Results from the HPEM for a test case using an inductively coupled etch tool for Chlorine-based etching of polysilicon are presented in this section. The geometry we used resembles the Lam Research Corporation 9400 TCP (Transformer Coupled Plasma) Etching Tool, and is shown in Fig. 2.2. The plasma is generated by the 13.5-MHz inductively coupled electric field produced by a flat spiral coil on top of a quartz window above and parallel to the substrate. The 20-cm-diameter wafer sits on an RF-biased substrate, also at 13.56 MHz, 180° out of phase to the coil. The wafer is surrounded by an alumina focus ring. Gas is injected through a shower-head arrangement just below the coils with a flow rate of 100 sccm and pumped out at the base of the reactor. We have investigated pure Cl₂ at pressures of 5-20 mTorr. The rate coefficients for gas phase

neutral chemical and ion-molecule reactions used in the model are the same as listed in Ventzek *et al.*⁴

The base case for our study uses the pure chlorine gas mixture at 10 mTorr, 600-W ICP power with an RF bias of 100 W resulting in a 70-V amplitude on the substrate. The power deposition, positive ion density (Cl^+ , and Cl_2^+), and the positive ion source obtained from the HPEM are shown in Fig. 2.3. The resistive inductively coupled power deposition has a maximum of 1.2 W/cm^3 and is located approximately 1 cm below the quartz window due to the finite skin depth of the inductively coupled field into the plasma. Due to the long mean free path of electrons at 10 mTorr, the electron impact source for Cl_2^+ is more extended than that for power deposition.

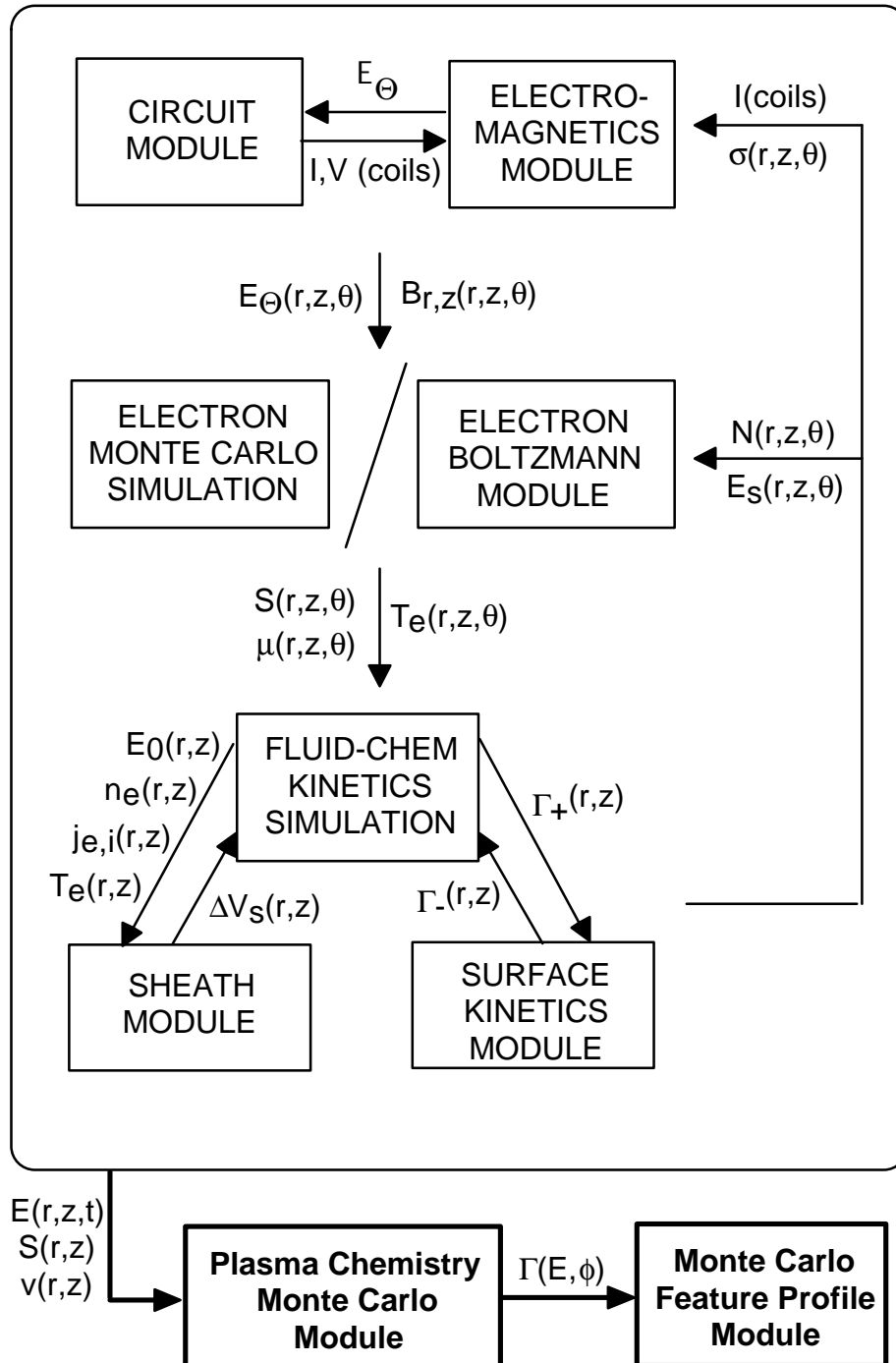


Fig. 2.1. Flowchart of HPEM modules. The HPEM consists of three main modules including the electromagnetics module, the EEDF module, and the fluid-chemical kinetics module. The hybrid model iterates successively through the modules until convergence is achieved.

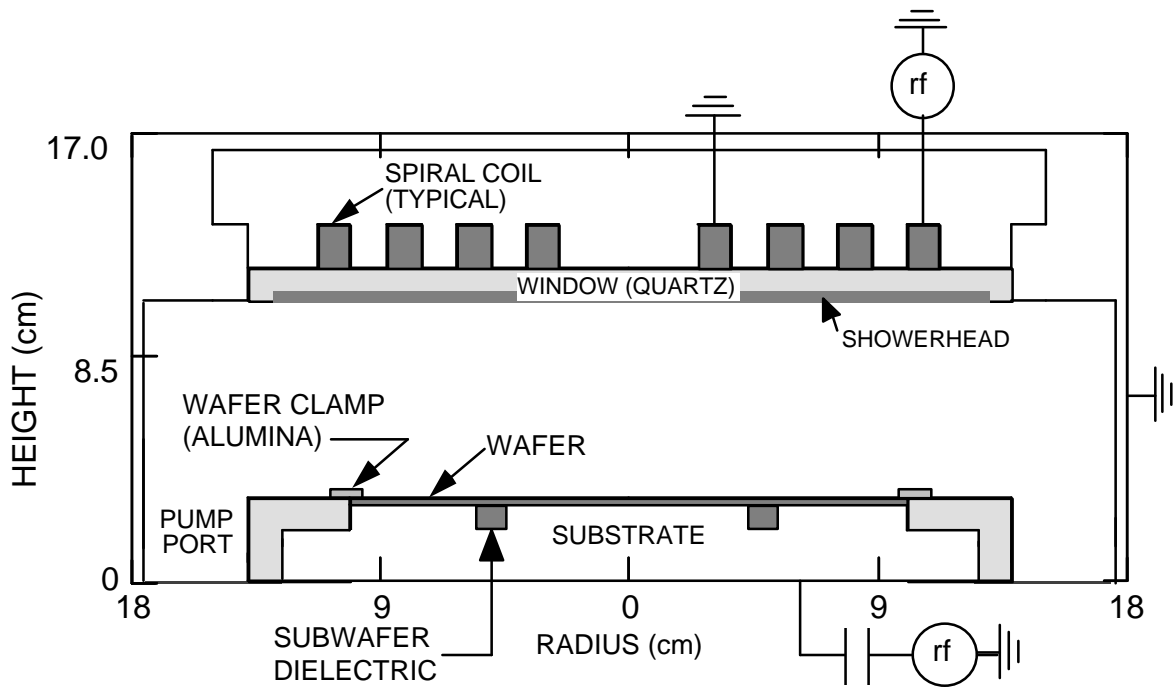


Fig. 2.2. Schematic of inductively coupled plasma reactor used for the simulations. The indicated wafer clamp and subwafer dielectric are included for specific cases to demonstrate physical phenomena.

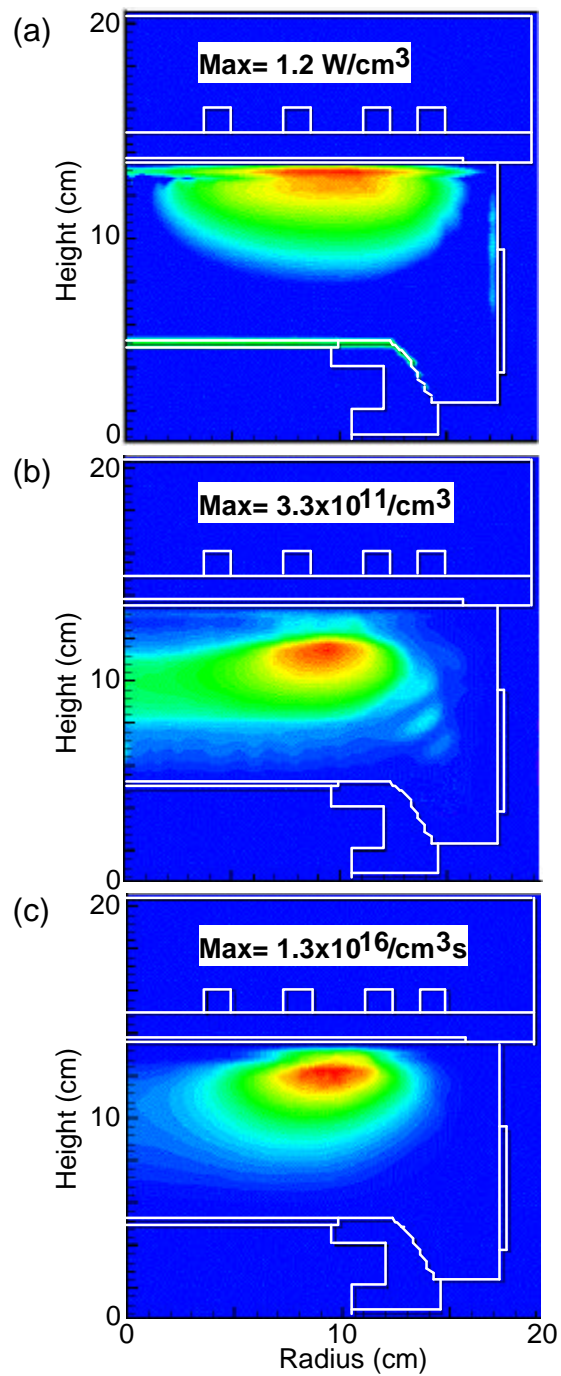


Fig. 2.3. Cl_2 plasma at 10 mTorr with an ICP power of 600 W and RF bias of 100 W. The contours represent (a) the total power deposition (inductive and capacitive), (b) the positive ion density, and (c) the electron impact source of positive ions.

2.4. References

1. T. J. Sommerer and M. J. Kushner, *J. Vac. Sci. Technol. A* **71**, 1654 (1992).
2. P. L. G. Ventzek, T. J. Sommerer, R. J. Hoekstra, and M. J. Kushner, *Appl. Phys. Lett.* **63**, 605 (1993).
3. P. L. G. Ventzek, R. J. Hoekstra, and M. J. Kushner, *J. Vac. Sci. Technol. B* **12**, 461 (1993).
4. P. L. G. Ventzek, M. J. Grapperhaus, and M. J. Kushner, *J. Vac. Sci. Technol. B* **16**, 3118 (1994).
5. W. Z. Collison and M. J. Kushner, *Appl. Phys. Lett.* **68** 903 (1996).
6. M. J. Kushner, W. Z. Collison, M. J. Grapperhaus, J. P. Holland, and M. S. Barnes, *J. Appl. Phys.* **80**, 1337 (1996).
7. M. J. Grapperhaus and M. J. Kushner, *J. Appl. Phys.* **81**, 569 (1997).
8. S. Rauf and M. J. Kushner, *J. Appl. Phys.* **81**, 5966 (1997).
9. M. J. Kushner, W. Z. Collison, M. J. Grapperhaus, J. P. Holland, and M. S. Barnes, *J. Appl. Phys.* **80**, 1337 (1996).
10. E. Keiter and M. J. Kushner, submitted to *J. Appl. Phys.*
11. H. H. Hwang and M. J. Kushner, *Appl. Phys. Lett.* **68**, 3716 (1996).
12. F. Y. Huang and M. J. Kushner, *J. Appl. Phys.* **81**, 5960 (1997).
13. D. Zhang and M. J. Kushner, in progress.
14. S. Rauf and M. J. Kushner, *IEEE Trans. Semiconduct. Manufact.* **11**, 486 (1998).
15. M. E. Riley, *Sandia Report SAND95-0775.UC-401*, 1995.

3. PLASMA CHEMISTRY MONTE CARLO MODEL

3.1. Introduction

The Plasma Chemistry Monte Carlo Model (PCMCM) was developed to examine the energy and angular distributions of the plasma species fluxes, including neutrals, ions, and excited-state species, as they transport in the plasma and impinge on the reactor surfaces. The PCMCM model uses two-dimensional (2D) electron impact source functions for charged, neutral, and excited species from the electron energy transport module (EETM), and the time-dependent electrostatic fields $E_s(r,z,t)$ and the advective flow fields $v_{r,z}(r,z)$ from the fluid-chemical kinetics simulation (FKS) from the Hybrid Plasma Equipment Model (HPEM). From this data, pseudoparticles are released in the reactor, and angular and energy distributions as well as fluxes are found for all plasma species at the reactor surfaces. Also, densities as well as momentum fluxes in the plasma can be calculated. The Monte Carlo simulation is iterated 10s of times, which allows plasma species densities and feedstock gas depletions to be calculated. The revised densities are used in the following iterations for collisions between Monte Carlo species and adjustment to feedstock densities. The resulting statistics for particle energy and angular distributions (PEADs) are used by the Monte Carlo Feature Profile Model (MC-FPM) as described in Chapter 4 to self-consistently determine radially-dependent feature evolution on the substrate for semiconductor plasma processes.

3.2. Description of the Model

The majority of the development of the PCMCM was performed for the author's master's thesis.¹ Therefore, only a brief description and examples will be presented here as well as mention of changes since the earlier publication.²

3.2.1. Computational mesh

The computational grid representing the reactor is identical to the one used by the main HPEM modules. It is made up of a rectilinear uniform mesh defining materials densities at centered mesh locations while electrostatic properties are defined one half cell away allowing more direct solution of the finite difference equations in the main modules.

3.2.2. Particle launch

Particles are launched in the reactor according to the spatial distribution of the source functions $S_i(r,z)$ obtained from the EEDFM. The number of particles of species i released in a given cell is based on the spatial distribution of the source function and the maximum number of particles allowed:

$$S_i^{\#}(r, z) = \max \left\{ S_{\min}^{\#}, P^{\#} \times \frac{S_i(r, z)V(r, z)}{S_{\text{total}}^{\#}} \times \frac{1}{Wt_i^S(r, z)} \right\}, \quad (3.1)$$

where $S_{\min}^{\#}$ is the minimum allowable number of particles released in a cell for each species, $P^{\#}$ is the total number of particles released, and $V(r,z)$ is the volume of the cell.

$$S_{\text{total}}^{\#} = \sum_{i,r,z} S_i(r, z)V(r, z)Wt_i^S(r, z), \quad (3.2)$$

gives the total weighted sum of the sources, and

$$Wt_i^S(r, z) = \frac{\log[S_i(r, z)]}{\log[S_{\max}]}, \quad (3.3)$$

where $S_{max} = \max_{i,r,z}[S_i(r,z)]$. Using this logarithmic weighting allows for a statistically significant number of particles to be released in low source cells. The actual particle weighting (number of molecules/sec) is then

$$Wt_i(r, z) = S_i(r, z)V(r, z) / S_i^{\#}(r, z). \quad (3.4)$$

Initial conditions for species densities are taken from the HPEM results. However, density statistics for the Monte Carlo species are determined by adding the weighting Wt_i times the transit time through the cell to give the pseudoparticle's contribution to that cell. These densities can be averaged in with the HPEM results, allowing the long mean free path effects accounted for in the PCMCM to be added. For negative values of $S_i(r,z)$ or loss regions for species i , reactions are created based on collisions with a dummy species which removes particles at the rate specified by $S_i(r,z)$.

Each particle is released with a random direction, position in the cell, and speed chosen from a Maxwellian distribution,

$$v = \sqrt{\frac{8 k_b T}{\mathbf{p} m_j} \ln \left(\frac{1}{(1-r)^2} \right)}, \quad (3.5)$$

where k_b is Boltzmann's constant, T is the temperature of the gas, m_j is the mass of species j , and r is a random number between zero and one. In general, the temperature used is around 300 K, or room temperature. The "bath" or fluid velocity at that cell, which is determined by the momentum flux results from the HPEM, is added to the thermal velocity, allowing the Monte Carlo particles to "see" the advective flow.

3.2.3. Particle motion

Once the particles are released they are allowed to transport based on the effects of local electric fields, collisions, and bounding surfaces. The acceleration of each charged particle is determined by the electric fields $E_r(r,z,t)$ and $E_z(r,z,t)$. The acceleration of the particle is derived from linear interpolation between the four field points surrounding the cell, and particles are time-stepped using two linear equations representing the change in position and velocity:

$$\mathbf{v}_i = \mathbf{v}_{i-1} + \frac{q\mathbf{E}}{m} \Delta t \quad \text{and} \quad \mathbf{x}_i = \mathbf{x}_{i-1} + \mathbf{v}_i \Delta t . \quad (3.6)$$

A time of flight is calculated as

$$\Delta t_{\min} = \min \left(\Delta t_{\Delta r}, \Delta t_{\Delta z}, \Delta t_{col}, 0.01 \cdot \mathbf{t}_{RF} \right) , \quad (3.7)$$

where $\mathbf{D}t_r$ and $\mathbf{D}t_z$ are the times to move a fraction of $\mathbf{D}r$ or $\mathbf{D}z$ (cell width), and $\mathbf{D}t_{col}$ is the time to the next collision,

$$\Delta t_{col} = r \left(\sum_k \mathbf{n}_{col,k} \right)^{-1} , \quad (3.8)$$

where $\mathbf{n}_{col,k}$ is the collision frequency for process k and r is a random number between zero and one. If the particle is moving through a region where the time-dependent electric

fields vary more than 1% over an RF cycle, the time-step is constrained to 1% of the RF period.

A particle can also collide with a surface. When a particle is moved, it can transition from a gas cell to a solid cell. If the particle has collided with the substrate and the time-dependent sheath potential and thickness data have been received from the FKS, the particle is time-stepped through the sheath potential before it interacts with the surface. The particle is moved to a position just inside the gas cell, and a surface reaction is determined as described below. A flowchart portraying pseudoparticle motion is shown in Fig. 3.1.

3.2.4. Gas phase reactions

Several types of gas phase reactions are included for the Monte Carlo (MC) particles, such as elastic, charge exchange, three-body association, as well as any other two-body reactions appropriate to the chemistry. Probability arrays for collision frequencies of each species are calculated using the reaction coefficients k_l and maximum collision partner densities $N_{i,max}$:

$$P_j = \sum_{l=1}^j k_l N_{i,max} . \quad (3.9)$$

However, for three-body reactions, the density of the third body must be added, in this case the total gas density N_{total} :

$$P_j = \sum_{l=1}^j k_l N_{i,max} N_{total} . \quad (3.10)$$

A time to next collision for each particle is calculated as $t = \mathbf{n}^{-1}_{total} \ln(r)$, where \mathbf{n}_{total} is the total collision frequency for all processes possible for that species and r is a random number. The process which has occurred is found by indexing the probability matrix for that species with a random number r , where $P_{i-1} < r \leq P_i$ indicates that process i has occurred. The actual occurrence of a reaction is then found by

$$r \leq \frac{N_i(r, z)}{N_{i, \max}}, \quad (3.11)$$

where r is a random number between zero and one. This allows for null collisions where the collision partner density is below its spatial maximum. When feedstock species or other non-MC species are created by the reaction, the particle is removed. If, however, one or two MC species are produced, the colliding particle's identity is changed and a new MC particle can be added. See Table 3.1 for the reaction scheme used in simulations of chlorine etching plasmas.

The elastic collisions between feedstock species and MC particles allow the particles to sense the density and, therefore, the mean free path \mathbf{l}_{mfp} as well as the advective flow of the gas through the system. The rate coefficients for elastic collisions are calculated using Lennard-Jones radii to simulate hard sphere collisions:

$$k_i = v_{thermal} \mathbf{p} \left[\frac{\mathbf{s}_1 + \mathbf{s}_2}{2} \right]^2, \quad (3.12)$$

where $v_{thermal}$ is the thermal velocity of the species and \mathbf{s}_k is the Lennard-Jones radii for species k . Lennard-Jones parameters were obtained from R. A. Sveha.³ In a collision, the mesh particle that has been collided with is given a velocity which is the sum of a random

thermal (Maxwellian) velocity, as described earlier, and the advective flow velocity at that mesh point. In this way, through an energy conservative collision, the MC particle “feels” the effects of the advective flow. The energy gained or lost by the particle is derived by calculating a random scattering angle,

$$\mathbf{q}_s = 2 \sin \left(\sqrt{r} \right) \cdot \min \left[\frac{m_{cp}}{m_i}, 1 \right], \quad (3.13)$$

where r is a random number (0,1), m_{cp} is the mass of the collision partner, and m_i is the mass of the particle. For cases in which the particle energy is greater than that of the collision partner, the energy loss is

$$\Delta E = -E_i [1 - \cos(\mathbf{q}_s)] \frac{m_r}{2\bar{m}}, \quad (3.14)$$

while for cases where the particle energy is less than that of the collision partner, the energy gain is

$$\Delta E = E_{cp} [1 - \cos(\mathbf{q}_s)] \frac{m_r}{2\bar{m}}, \quad (3.15)$$

where E_i is the energy of the particle, E_{cp} is the energy of the collision partner, m_r is the reduced mass, and \bar{m} is the average mass.

Charge exchange reactions, including both symmetric and asymmetric are included since they can produce high-energy (10s of eV) neutral species in the plasma. In a charge exchange collision between a neutral and a positive ion, there is very little energy transfer,

but the charged particle is neutralized while retaining its energy. For positive ion species such as Ar^+ in an argon plasma, this charge exchange rate can be high enough to allow hot neutral fluxes to surfaces to have a magnitude which is a significant fraction of the flux due to the corresponding ions. These high-energy fluxes of neutrals to the substrate could play an important role in surface chemistry and, therefore, etch and deposition rates.

3.2.5. Surface interactions

Surface reactions are carried out on the basis of two parameters, a reflection coefficient and a reactive sticking coefficient, both of which range from zero to one. When a particle collides with a reactor surface including the substrate, a randomly generated number is compared to the reflection coefficient. If the random number is smaller, the particle is reflected with no change in identity. If the random number is greater, another random number is generated and compared to the reactive sticking coefficient. A number larger than the sticking coefficient corresponds to the particle sticking to the surface without production of gas species. However, if the number is smaller, a gas species particle is produced based on the surface reaction that has occurred. These coefficients can be dependent on the surface material, mainly with respect to the differences in the wafer and reactor wall materials.

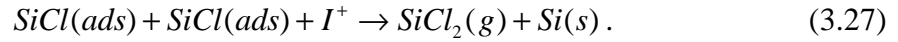
The reactive sticking coefficient serves several purposes. In all cases, ions are considered to be neutralized at surfaces with a small probability of sticking. Excited-states species are also returned as ground-state products. Other species, such as the Cl radical, can be allowed to return as etch products. In the cases run, the chlorine radical was allowed to stick to nonreactive surfaces with 0.005 probability, producing the recombination product Cl_2 50% of the time. For the reactive silicon wafer surface, the Cl reactive sticking coefficient is determined by the etch rate calculated from Dane and

Mantei's³ etch model described below. This, in effect, allows for macroloading of the plasma system by these etch products as found in experiments.

The etch model of Dane and Mantei⁴ for a chlorine plasma was used to calculate etch rates at the wafer and production rates of gaseous etch products. The etch model is based on a surface reaction scheme,



and



The $SiCl(ads)$ is Cl bonded to a Si on the wafer surface, and I^+ is any species of ion sticking the surface. This produces an etch rate formula which has a parallel resistive or series capacitive form,

$$ER = \left[\frac{1}{a\Gamma_{Cl}} + \frac{1}{b[J_i V_s - (JV)_{th}]} \right]^{-1}, \quad (3.18)$$

where $\mathbf{a} = 2300 \text{ \AA min}^{-1} \text{ mTorr}^{-1/2}$ and $\mathbf{b} = 23 \text{ \AA min}^{-1} \text{ mW}^{-1} \text{ cm}^2$ are fitting parameters, $(JV)_{th} = 85 \text{ mW cm}^{-2}$ is the threshold power flux to the wafer for the onset of etching, Γ_{Cl} is the Cl radical flux rate, and $J_i V_s$ is the actual power flux to the wafer which was approximated by Dane and Mantei as the ion current density to the wafer multiplied by the sheath voltage. Dane and Mantei were unable to measure Γ_{Cl} in their experimental setup and, therefore, used an approximation of $\Gamma_{Cl} \propto \sqrt{P_{Cl_2}}$ due to the Cl_2 dissociation

producing two Cl radicals. Therefore, their Γ_{Cl} is expressed in terms of $\text{mTorr}^{-1/2}$ and the α parameter has units of ($\text{\AA} \text{ min}^{-1} \text{ mTorr}^{-1/2}$). For these simulations, actual Cl radical fluxes in terms of ($\#\text{Cl cm}^{-2} \text{ s}^{-1}$) were calculated. Dane and Mantei's α parameter was converted to units of ($\text{\AA} \text{ min}^{-1} \text{ cm}^2 \text{ s}$) by calculating an estimated Γ_{Cl} in terms of ($\#\text{Cl cm}^{-2} \text{ s}^{-1}$). Based on a temperature of 600 K,

$$|v_{th,z}| = \sqrt{\frac{2 k_b T}{p m_{Cl}}} \approx 2.98 \times 10^5 \text{ cm/s.} \quad (3.19)$$

Using an estimated 50% dissociation of the Cl_2 at 1 mTorr gives a Cl radical density of $\sim 2.36 \times 10^{13} (\#\text{/cm}^3)$. The Cl radical flux to the wafer can be then estimated as

$$\Gamma_{Cl} \approx \frac{1}{2} N_{Cl} |v_{th,z}| = 3.5 \times 10^{17} \text{ cm}^{-2} \text{ s}^{-1} \quad \{ \text{at 1 mTorr} \}. \quad (3.20)$$

Using this estimated value for Γ_{Cl} , a new α can be found of $6.54 \times 10^{-15} (\text{\AA} \text{ min}^{-1} \text{ cm}^2 \text{ s})$. This is an upper-limit estimate, since it does not account for spatial nonuniformity of the Cl and the effects of macroloading at the wafer. This etch model was used to look at radial uniformity of etch rates as well as the effects of varying inductive power, substrate RF bias, and pressure.

In all cases, the particles are returned to the gas with an angle based on a modified cosine or Lambertian distribution,⁵

$$\Phi = \cos^{-1} \left[\left(1 - r a \int^{1/(b+1)} \right) \right], \quad (3.21)$$

in which r is a randomly generated number between zero and one, α is given by

$$\mathbf{a} = -\cos\left(\frac{\mathbf{q}_{\max}}{180p}\right)^{(b+1)}, \quad (3.22)$$

b is the exponential cosine factor, and \mathbf{q}_{\max} is the maximum normal angle which the particle can have. They are returned to the plasma with an energy chosen randomly from a Maxwellian distribution with temperature equal to that of the surface. Particles can also be allowed to return with a fraction of their prior energy, which allows for spectral scattering from the surface.

3.2.6. Collected Statistics

A myriad of statistics are determined during the simulation, both in the plasma and at the surfaces which allow analysis of the system “unhindered” by the problems of physical experimental measurement. In the plasma, spatial- and species-dependent statistics are found for the radial and axial momentum flux, the kinetic energy, the temperature, and the density. At the surfaces, spatial and species dependent statistics are found for angular distribution, flux, and energy distribution of particles. These statistics can be viewed graphically in two or three dimensions to help explain the effects of changes in the reactor parameters such as pressure, power, or reactor geometry.

3.3. Typical Results

In Section 2.3, the simulation of an inductively coupled plasma (ICP) etching reactor for the HPEM was described and plasma conditions were presented. For this

section, the HPEM results for that simulation case were used as input to the PCMCM, and the resulting surface flux statistics are presented and analyzed.

The fluxes to the wafer for positive ions and Cl atoms obtained with the PCMCM are shown in Fig. 3.2. Even though the ions are not generated uniformly, the substrate-to-source distance is sufficiently large that diffusion smoothes the ion flux profile to the wafer. There is a slight maximum at half the radius which mirrors the source function. The flux is dominated by Cl_2^+ , due to the fact that Cl_2^+ is produced in the nonsymmetric charge exchange of Cl_2 with Cl^+ . The flux of Cl is also fairly uniform. The transport of Cl radicals is diffusion dominated and, when combined with a low sticking coefficient at the walls, leads to high radial uniformity. The radially averaged energy distributions of the neutral Cl radical striking the substrate are shown in Fig. 3.3. The neutrals generally impact the wafer with a nearly Maxwellian velocity distribution with temperature of 600-700K. The heating is largely due to charge exchange reactions.

The IEDs averaged over the wafer for Cl_2^+ and Cl^+ are shown in Fig. 3.4 for a 100-W bias. The IEDs clearly show the characteristic bimodal distribution resulting from short ion transit times (with respect to the RF period) usually associated with lower-frequency operation in RIE discharges. The short ion transit times result from the thin sheaths for these conditions, ≈ 0.04 cm, produced by the high plasma density. For this sheath thickness the transit time for Cl^+ is ≤ 25 ns, which is shorter than the rf period 13.56 MHz (60 ns). This allows the ions to “sense” the instantaneous sheath potential. Since Cl_2^+ is twice as massive as Cl^+ , its transit time is longer, ≈ 32 ns, resulting in the Cl_2^+ ion “sensing” a more averaged sheath potential, producing an IED having a somewhat narrower width.

The average angle of incidence and energy of ions are essentially constant as a function of position on the wafer. The average angle of incidence of Cl_2^+ is $\approx 8^\circ$ for an RF bias of 100 W with an average impact energy of 30 eV. This corresponds to ions entering

the sheath with temperatures of 0.5-1.0 eV, which agrees with the experiments of O'Neill *et al.*⁵ For the unbiased substrate, the average incident angle is 29°, since the potential drop across the sheath is due only to the floating potential, producing ions with an average impact energy of 10 eV, with an ion temperature entering the sheath of 0.5-1.0 eV. The high temperature of the ions results largely from acceleration through the presheath. These results agree well with both direct measurements of the IED in unbiased systems and with the implied temperature of ions required to account for etch profiles.⁷⁻⁹

The mechanism of Dane and Mantei for chlorine etching of poly-Si was used to predict etching rates for the Ar/Cl₂ ICP discharges. The predicted radical and ion power fluxes incident on the wafer as a function of position for the standard case [Ar/Cl₂ = 70/30, 10 mTorr, ICP power = 500 W, RF bias (amplitude) = 100 V] are shown in Fig. 3.5. The Cl radical flux is uniform to within 10% over the 10 cm radius of the wafer, and maximum at the center of the reactor. The ion power flux (which shows numerical noise) has a local maximum at mid-radius as a consequence of the nonuniform power deposition. The Cl₂⁺ ion contributes approximately 60% of the power flux, in proportion to its total molecular flux. The predicted power flux limited etch rate (that is, the etch rate which one would predict with infinite Cl flux) is ≈ 5000 Å/min and reflects the nonuniform power flux to the wafer. The neutral limited etch rate (that is, the etch rate which one would predict with an infinite power flux) is ≈ 3000 Å/min and is uniform as a function of radius. The combined etch rate has an average value of 1850 Å/min. It is uniform to within 10% over 90% of the radius of the wafer, reflecting the uniformity of the Cl atom flux with some small enhancement due to the local extreme in the ion power flux. This etch rate corresponds to a flux rate of SiCl₂ from the surface of $1.5 \times 10^{16} \text{ cm}^{-2}\text{s}^{-1}$. For an ion flux of $\approx 7 \times 10^{16} \text{ cm}^{-2}\text{s}^{-1}$, the ratio of ion impacts to etched SiCl₂ is 4-5:1. This value compares well to the results of surface laser desorption studies,¹⁰ as well as the results of Dane and Mantei.⁴

By increasing the RF bias amplitude applied to the substrate, the power flux of ions can be proportionally increased without significantly changing the magnitude of either the ion or Cl atom flux. This increase in power flux should, in principle, increase the etch rate at lower RF biases where the etch rate is ion power flux limited, but not at high RF biases where the etch rate is neutral flux limited. Predicted etch rates as a function of RF bias (amplitude) for ICP powers of 150, 500, and 1000 W are shown in Fig. 3.6. At low RF biases, the ion power flux is near the threshold value of 85 mW/cm^2 . Increasing the RF bias increases the power flux and so increases the etch rate (the "ion starved" regime). At larger biases where the ion power flux greatly exceeds the threshold value, increasing the power flux at best yields a moderate increase in etch rate. The etch rate is then limited by the availability of Cl atoms (the "neutral starved" regime) and the etch rate approaches a constant value. The etch rates at low ICP power and low RF bias may be underestimated due to lack of a purely thermal component in the etch model as implied by there being a threshold ion power for etching.

Table 3.1. Gas phase reactions for Ar/Cl₂ gas mixture.

Process	Rate Coefficient ^a	Ref.
Ar* + Ar → Ar* + Ar	2.217 × 10 ⁻¹⁰	b
Ar ⁺ + Ar → Ar ⁺ + Ar	2.217 × 10 ⁻¹⁰	b
Cl ₂ ⁺ + Ar → Cl ₂ ⁺ + Ar	2.348 × 10 ⁻¹⁰	b
Cl + Ar → Cl + Ar	2.329 × 10 ⁻¹⁰	b
Cl ⁻ + Ar → Cl ⁻ + Ar	2.329 × 10 ⁻¹⁰	b
Cl ⁺ + Ar → Cl ⁺ + Ar	2.329 × 10 ⁻¹⁰	b
Cl* + Ar → Cl* + Ar	2.329 × 10 ⁻¹⁰	b
Ar* + Cl ₂ → Ar* + Cl ₂	2.348 × 10 ⁻¹⁰	b
Ar ⁺ + Cl ₂ → Ar ⁺ + Cl ₂	2.348 × 10 ⁻¹⁰	b
Cl ₂ ⁺ + Cl ₂ → Cl ₂ ⁺ + Cl ₂	2.356 × 10 ⁻¹⁰	b
Cl + Cl ₂ → Cl + Cl ₂	2.487 × 10 ⁻¹⁰	b
Cl ⁻ + Cl ₂ → Cl ⁻ + Cl ₂	2.487 × 10 ⁻¹⁰	b
Cl ⁺ + Cl ₂ → Cl ⁺ + Cl ₂	2.487 × 10 ⁻¹⁰	b
Cl* + Cl ₂ → Cl* + Cl ₂	2.487 × 10 ⁻¹⁰	b
Ar* + Ar* → Ar ⁺ + Ar + M ⁻	5.000 × 10 ⁻¹⁰	11
Cl ⁻ + Cl ⁺ → Cl + Cl	1.000 × 10 ⁻⁷	c,12
Cl ⁻ + Cl ₂ ⁺ → Cl + Cl ₂	1.000 × 10 ⁻⁷	c,12
Cl ⁻ + Ar ⁺ → Cl + Ar	1.000 × 10 ⁻⁷	c,12
Ar* + Cl ₂ → Ar + Cl ₂ ⁺ + M ⁻	7.100 × 10 ⁻¹⁰	13,14
Ar* + Cl → Ar + Cl*	7.000 × 10 ⁻¹²	14,15
Ar ⁺ + Cl ₂ → Ar + Cl ₂ ⁺	8.400 × 10 ⁻¹¹	16
Ar ⁺ + Cl ₂ → Ar + Cl ⁺ + Cl	6.400 × 10 ⁻¹¹	16
Ar ⁺ + Cl → Ar + Cl ⁺	2.000 × 10 ⁻¹⁰	c
Cl + Cl + M → Cl ₂ + M	1.280 × 10 ⁻³² cm ⁶ s ⁻¹	d,17
Cl ⁺ + Cl ₂ → Cl + Cl ₂ ⁺	5.400 × 10 ⁻¹⁰	18
Ar ⁺ + Ar → Ar + Ar ⁺	1.000 × 10 ⁻⁹	c,19
Cl ₂ ⁺ + Cl ₂ → Cl ₂ + Cl ₂ ⁺	1.000 × 10 ⁻⁹	c,19

^a Rate coefficients have units of cm³s⁻¹ unless otherwise noted.

^b Elastic collision rate coefficients were calculated based on Lennard-Jones parameters.

^c Estimated.

^d Three body rate coefficient with M being any other gas species.

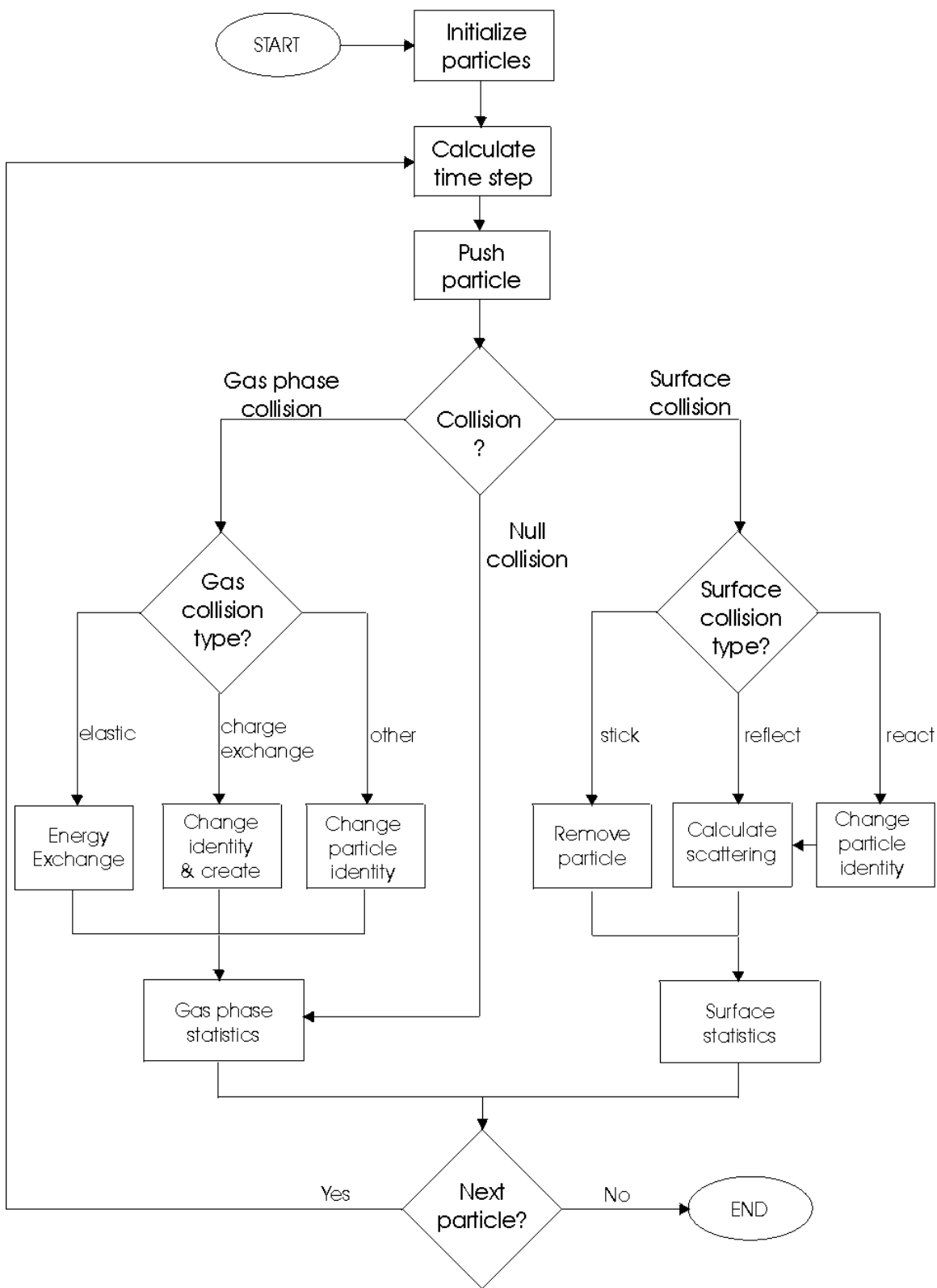


Fig 3.1. Flowchart of pseudoparticle path for the Plasma Chemistry Monte Carlo Model.

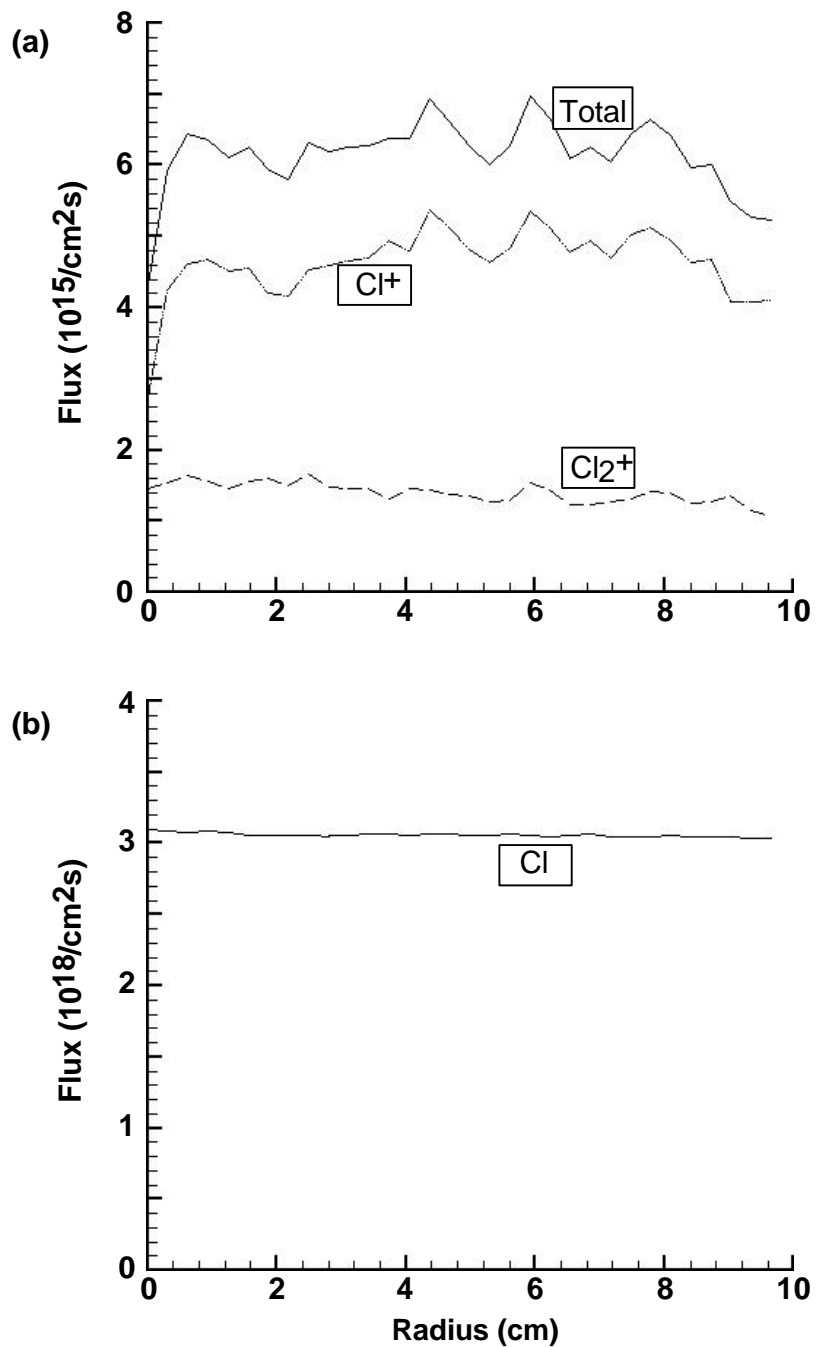


Fig. 3.2. Radial flux distribution at the wafer for (a) positive ions and (b) Cl radical.

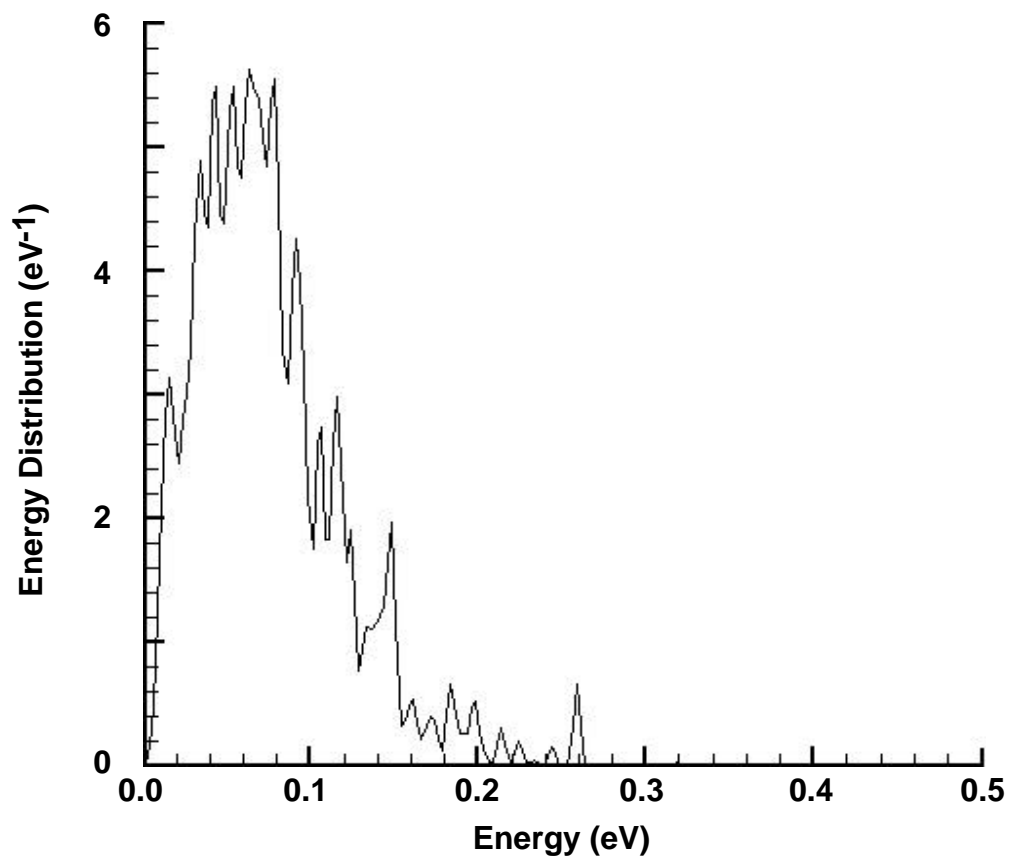


Fig 3.3. Energy distribution of Cl radical at the wafer.

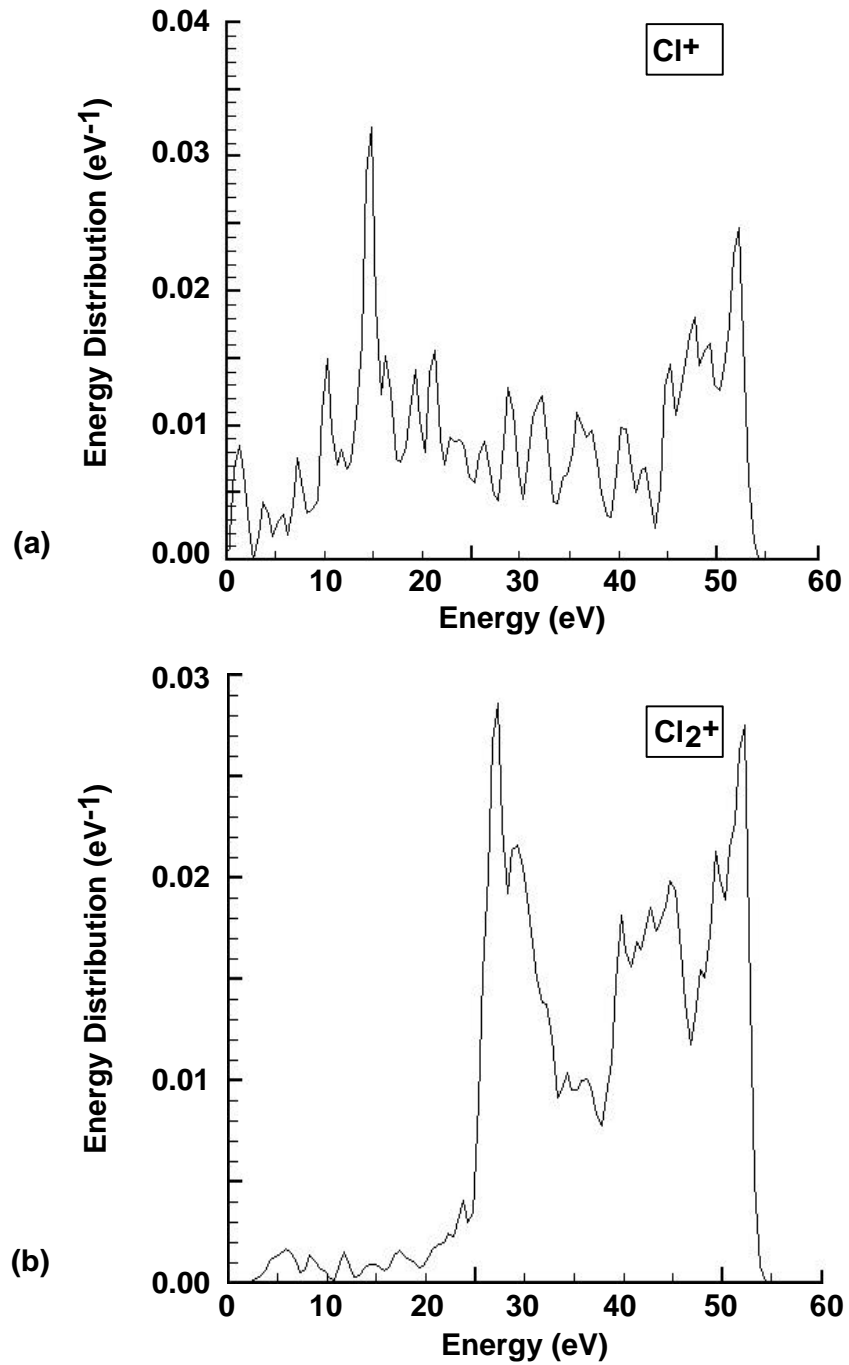


Fig. 3.4. Energy distributions for (a) Cl⁺ and (b) Cl₂⁺ at the wafer.

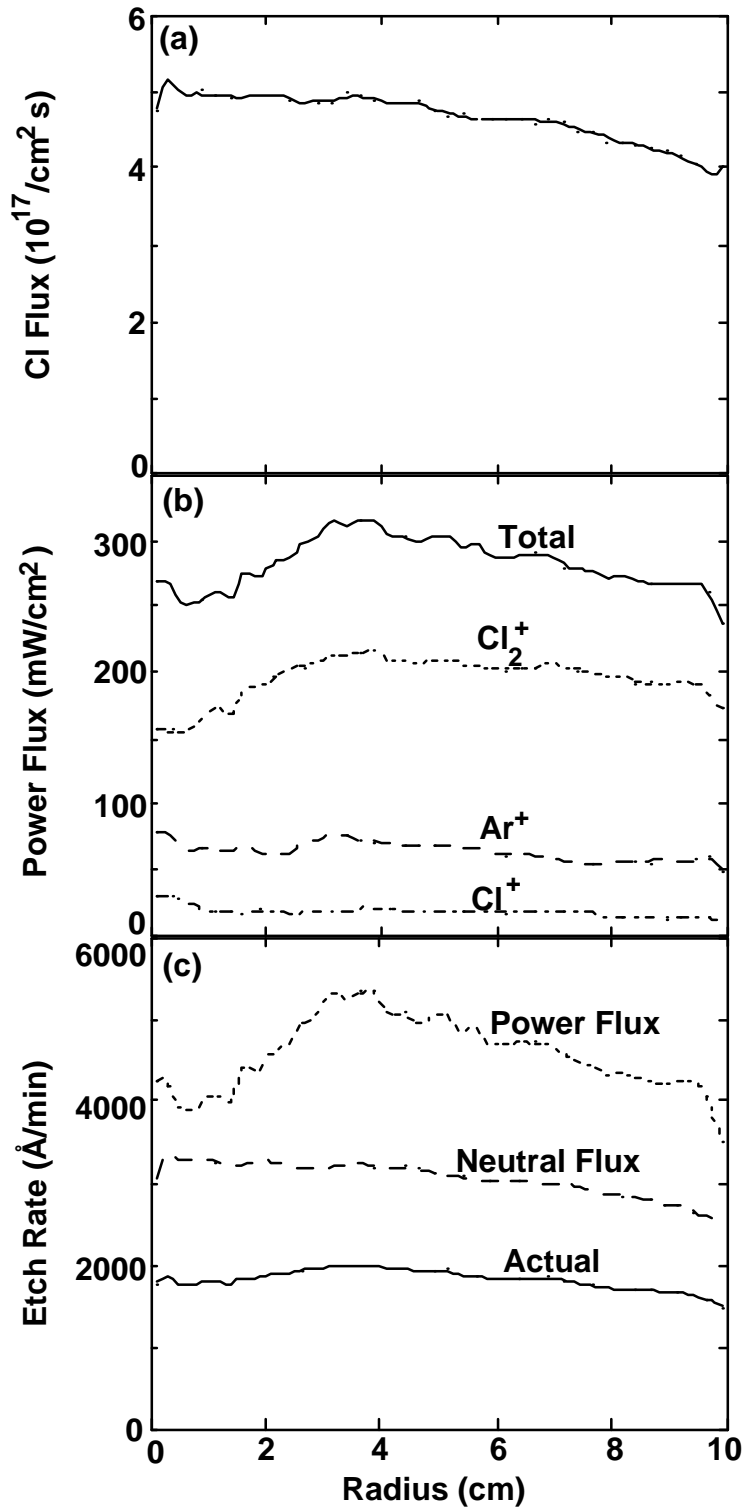


Fig. 3.5. Radial distribution of (a) Cl radical flux, (b) components and total power flux, and (c) limiting etch rates for power flux, neutral flux, and actual etch rate.

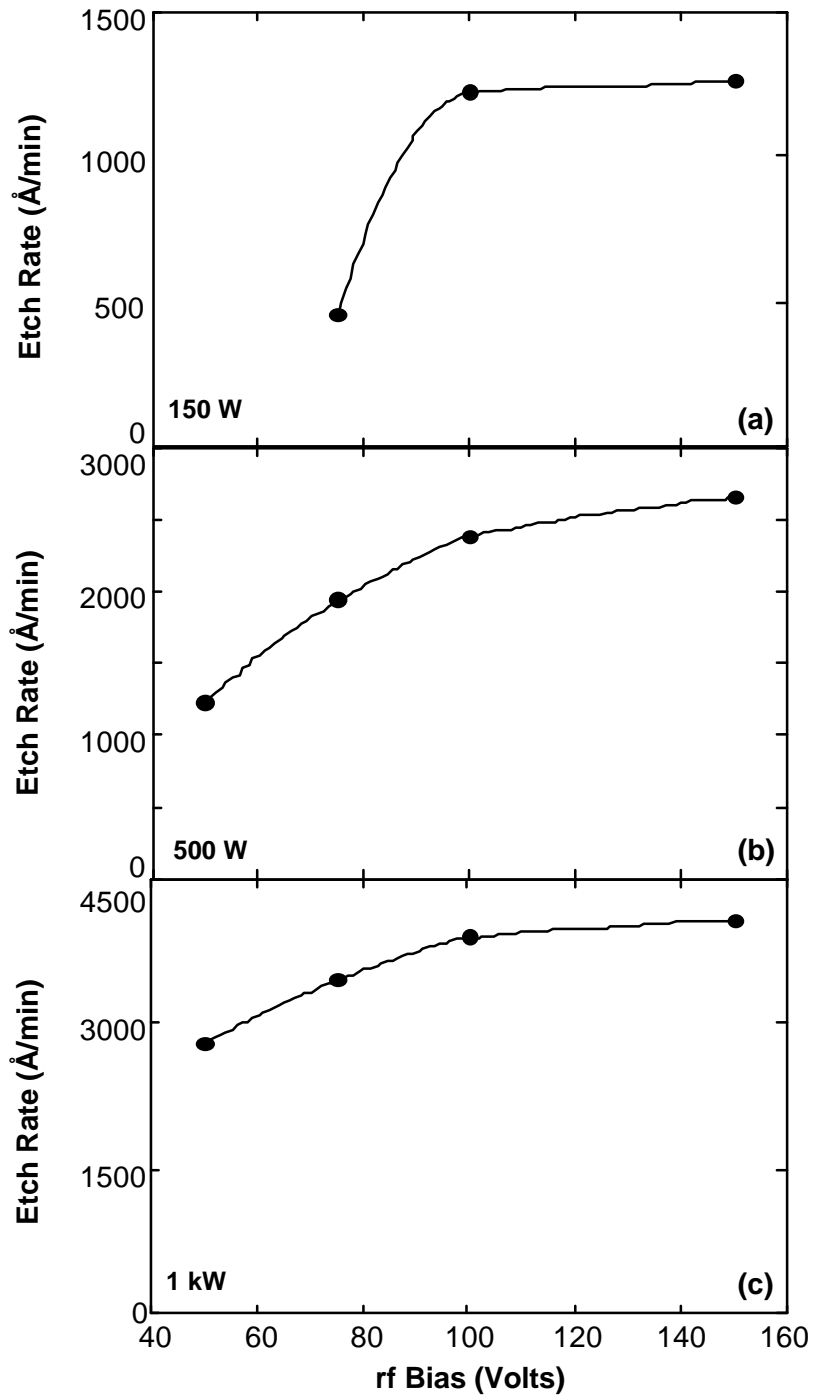


Fig. 3.6. Etch rates versus RF bias amplitude of the wafer for (a) 150 W, (b) 500 W, and (c) 1 kW.

3.4. References

1. R. J. Hoekstra, *A Plasma Chemistry Monte Carlo Model for Ion and Radical Fluxes and Energy Distributions in Inductively Coupled Plasma Etching Reactors*, (University of Illinois Urbana-Champaign, Urbana, 1995).
2. R. J. Hoekstra and M. J. Kushner, *J. Appl. Phys.* **77**, 3668 (1995).
3. R. A. Svehla, NASA Technical Report No. R-132, (1962).
4. D. Dane and T. D. Mantei, *Appl. Phys. Lett.* **65**, 478 (1994).
5. M. Born and E. Wolf, *Principles of Optics*, 5th ed. (Pergamon Press, Oxford, 1975), p. 182.
6. J. A. O'Neill, M. S. Barnes, and J. H. Keller, *Appl. Phys. Lett.* **62**, 2622 (1993).
7. J. Hopwood, *Appl. Phys. Lett.* **62**, 940 (1993).
8. U. Kortshagen, *Plasma Sources Sci. Technol.* **4**, 172 (1995).
9. J. Zheng, R. P. Brinkman, and J. P. McVittie, *J. Vac. Sci. Technol A* **13**, 859 (1995).
10. C. C. Cheng, K. V. Guin, V. M. Donnelly, and I. P. Herman, *J. Vac. Sci. Technol. A* **12**, 2630 (1994).
11. P. K. Leichner and R. J. Ericson, *Phys. Rev. A* **9**, 251 (1974).
12. R. E. Olson, J. R. Peterson, and J. Moseley, *J. Chem. Phys.* **53**, 3391, (1970).
13. J. Velazco, J. Holts, and D. W. Setzer, *J. Chem. Phys.* **65**, 3468 (1976).
14. N. L. Bassett and D. L. Economu, *J. Appl. Phys.* **75**, 1931 (1994).
15. D. L. King, L. G. Piper, and D. W. Setzer, *Soc. Faraday Trans.* **2**, 73, 177 (1976).
16. D. Smith, N. G. Adams, and E. Alge, *J. Phys. B* **17**, 461 (1984).
17. NIST Chemical Kinetics Database Version 5.0, (National Institute of Standards and Technology, Gaithersburg, MD, 1993).

18. Y. Ikezoe, S. Matsuoka, M. Takebe, and A. Viggiano, *Gas-Phase Ion-Molecule Reaction Rate Constants Through 1986* (Maruzen Company, Tokyo, 1987); analogy to O₂, D₂, and H₂.
19. H. Bohringer, M. Durup-Ferguson, and D. W. Fahey, *J. Chem. Phys.* **79**, 1974 (1983).

4. MONTE CARLO FEATURE PROFILE MODEL

4.1. Introduction

The Monte Carlo Feature Profile Model (MC-FPM) has been developed to allow self-consistent determination of topographical feature evolution for semiconductor processing in plasma reactors. To date, the model has been focused on etching but has the generality and capability to include deposition processes as well for plasma assisted chemical vapor deposition (PACVD), physical vapor deposition (PVD), and ionized physical vapor deposition (IPVD). The MC-FPM is integrated with the Hybrid Plasma Equipment Model (HPEM) and Plasma Chemistry Monte Carlo Model (PCMCM) through the use of particle energy and angular distributions produced by the PCMCM for arbitrary radial location on the substrate. The processes of chlorine etching of silicon and polysilicon have been examined based on rates and dependencies from experimental results, and comparison to experimental feature profiles has been favorable.

4.2. Description of the Model

The MC-FPM is a Monte Carlo model which simulates the use of statistically weighted pseudoparticles representative of the fluxes of active species to the feature surface. Through ballistic transport and interaction with the mesh delineated surface, time integrated surface evolution is obtained. Ion-enhanced plasma etching, specifically chlorine etching of polysilicon in inductively coupled plasma (ICP) reactors, has been the focus of study for this model.

4.2.1. Computational mesh

The MCFPM resolves wafer features on the submicron scale utilizing a rectilinear mesh. For the majority of two-dimensional (2D) results shown here, the feature will be an

infinitely long trench in polysilicon. The mesh spacing is typically 200 cells for 1- μm length, whereas currently the maximum resolution obtained has been 0.02- μm cell width. Each computational cell is therefore about 15×15 or fewer atoms. Each cell is assigned a material identity (e.g., poly-Si, photoresist, SiO_2 , plasma) which may change during the simulation. Solid species, including adsorbates or passivation, are represented by the identity of the computational cell. Each mesh cell represents a weighting larger than the gas species by some multiple, in most cases equal to 20. Initially, the mesh cell begins half filled by the material selected in the input file. Resulting removal or deposition decreases or increases the number of gas weighting species within the cell. As the mesh cell weighting reaches lower or high thresholds, the remaining or excess weighting is distributed to neighboring cells with a probability proportional to the neighboring cells weighting. This allows for much greater statistical significance of individual mesh points and alleviates noise issues related to low proportional weight cells. Fig. 4.1. illustrates an initial profile for a 2D infinite trench in polysilicon with a hard oxide mask and an oxide etch stop. For three-dimensional (3D) features, finite-length trenches or via holes are examined and, due to computation lengths, the resolution is reduced to 100 cells for 1- μm length. For all cases, a thin oxide mask was used to define the trench region and for some cases an oxide etch stop was used at the bottom of the feature.

4.2.2. Particle initialization

Gas phase species (i.e., radicals and ions) are represented by computational pseudoparticles. The MC-FPM begins by launching pseudoparticles representing radicals and ions towards the surface with initial trajectories (energy and angle) randomly chosen from the PEADs provided by the PCMCM. The PEADs produced by the PCMCM are flux weighted probability distribution functions (PDFs) which must be converted and normalized as cumulative distribution functions (CDFs).

$$CDF_{E_i, \mathbf{q}_j} = \frac{\sum_{ii=0}^i \sum_{jj=0}^j PDF_{E_{ii}, \mathbf{q}_{jj}}}{\sum_{all E} \sum_{all \mathbf{q}} PDF_{E_{ii}, \mathbf{q}_{jj}}} . \quad (4.1)$$

The pseudoparticles are launched with a frequency computed from the total flux of radicals or ions incident onto the substrate so that each pseudoparticle represents a fraction of the number of atoms in a mesh cell based on the gas-to-material weighting ratio.

$$Wt_g = \frac{1}{\mathbf{g}_{gs}} Wt_s , \quad (4.2)$$

where Wt_g is the gas particle weighting, Wt_s is the mesh or surface cell weighting, and \mathbf{g}_{gs} is the gas-to-surface ratio usually set to 20.

4.2.3. Particle motion

The pseudoparticle trajectories are advanced in time where the calculation of position and velocity are separated allowing solution of two linear equations:

$$\mathbf{v}_i = \mathbf{v}_{i-1} + \frac{q\mathbf{E}}{m} \Delta t \quad \text{and} \quad \mathbf{x}_i = \mathbf{x}_{i-1} + \mathbf{v}_i \Delta t , \quad (4.3)$$

where \mathbf{v} and \mathbf{x} represent the velocity and position of the particle, and the subscripts indicate the former or current velocity and position; q and m indicate the charge and mass

of the particle, respectively; and Dt indicates the time-step taken by the particle. This method is used because under the majority of cases the effects of charging are ignored and the electric field E is set to zero, allowing solution of the second linear equation only. The initial time-step of a particle is determined by the time required to move the minimum distance to a surface. After the particle has moved, the time-step is reset. If the distance to a surface is still greater than one mesh cell, this new distance is used to calculate the timestep. If the particle is within one mesh cell of a surface, it is moved the distance of one mesh cell width until a material containing cell is occluded. At this point, the particle is moved back to the last position, the time-step is halved, and the particle is moved again. This process is iterated until the particle moves within a fraction of the material containing cell, generally $0.05 \times (\text{Cell Width})$.

The effects of surface charging on the profile evolution can be addressed. Electron trajectories can be simulated as low-temperature isotropic fluxes which impinge upon the feature during the low-potential swing of the sheath. This macroscopically balances the current due to the ions. To resolve the electric fields due to the charged surfaces of the feature, an iterative explicit solution of Poisson's equation

$$\nabla \cdot e \nabla \mathbf{f}^{t+\Delta t} = -\mathbf{r}^t \quad (4.4)$$

is determined utilizing successive overrelaxation (SOR). SOR is used to accelerate solution by multiplying the calculated $D\mathbf{f}$ by an overrelaxation factor greater than one. Neumann boundary conditions are used at the top and bottom of the feature by assuming that the electric field above the feature matches the sheath field from the fluid-chemical kinetics simulation (FKS) and that the electric field below the feature is approximately

zero. The left and right boundaries are assumed to follow a periodic Dirichlet condition. An example case including self-consistent surface charging is presented in Section 5.6.

4.2.4. Surface interaction

A generalized reaction scheme for interaction of the ions and neutrals with the surface is used in the MC-FPM which allows for any reactant-product combination and for an energy dependence of the interaction. These processes are input to the MC-FPM through a file which lists the reactions in conventional chemical notation (e.g., $\text{Cl(g)} + \text{Si(s)} \rightarrow \text{SiCl(s)}$). This file is preprocessed to construct probability arrays for the reaction of pseudoparticle plasma species with surface species. The classes of reactions in the model include adsorption, passivation, ion activated etching, thermal etching, sputtering, ion or neutral reflection, and re-emission. When a pseudoparticle impacts on a surface, first a surface species is determined by random sampling weighted by the relative fractions of species represented in the cell, after which the reaction which occurs is chosen from the probability arrays using Monte Carlo techniques. Based on this reaction, the material identity of the chosen species in the computational cell at the site of impact is appropriately changed. Particles which are desorbed or re-emitted from the surface are generally given thermal speeds and launched with a Lambertian angular distribution. In the case of high-energy ions which impact at large angles with the normal of the surface, specular reflection can occur. The fraction of specular reflected energy retained by the ion is calculated as a function of energy and angle to the normal:

$$frac_{spec} = \min\left(1, \frac{E}{E_{th}}\right) \cdot \frac{\mathbf{q} - \mathbf{q}_{cutoff}}{90^\circ - \mathbf{q}_{cutoff}}, \quad (4.5)$$

where $frac_{spec}$ is the fraction of retained specular energy, E is the incoming particle energy, E_{th} is the threshold for complete specular reflection set to 100 eV, \mathbf{q} is the incoming particle's trajectory angle to the surface normal, and \mathbf{q}_{cutoff} is the lower cutoff angle for specular reflection set to 60° . These dependencies were chosen somewhat arbitrarily due to limited theoretical or experimental results indicating these values. The trajectory of etch or re-emission products are then tracked as pseudoparticles in the manner described by the reaction mechanism

4.2.5. Chlorine etching of polysilicon

The polysilicon etch mechanism we have adopted is based on the works of Cheng *et al.*¹ and Meeks *et al.*² Etching takes place by first successively chlorinating the polysilicon surface, forming $SiCl_n$ (i.e., SiCl followed by $SiCl_2$, and so on). This chlorination is dominantly accomplished by neutral Cl atoms but can also be achieved by Cl^+ and Cl_2^+ incorporation. For this model the effects of chlorine ion incorporation are ignored due to the large ratio (10s to 100s) of neutral flux to ion flux, producing an “ion-starved” regime. Etching of the poly-Si, and evolution of the $SiCl_n$ etch product then occurs through subsequent ion bombardment. A summary of the reaction scheme and reaction probabilities used in the model appears in Table 4.1. The probability for an ion of energy ϵ activating an etch scales as $(\epsilon - \epsilon_0)^{1/2}$, where ϵ_0 is a threshold energy where the threshold energy and slope of the yield is based on Donnelly *et al.*¹ In addition to the reactions appearing in Table 4.1, we also allowed there to be inhibitor fluxes which deposit on surfaces, thereby blocking the etch. The inhibitor is removed by ion bombardment or a purely physical sputter mechanism. The inhibitor flux is intended to represent polymerization which may be produced from sputtered mask material or other gas phase species. We also allow the polysilicon to be thermally etched by Cl atoms in the absence of ion bombardment, as may occur at high doping levels. The silicon dioxide

underlayer to the poly-Si is etched with an arbitrarily chosen selectivity of 1:50 relative to poly-Si. This is achieved by using an analogous reaction mechanism to that for poly-Si with reduced etch probabilities. Cl can also reassociate on chlorinated surfaces in the trench to produce Cl_2 ; however, for the cases presented here, Cl reassociation was not included. We did run test cases with this process using reaction probabilities of 0.02 for SiCl_2 and 0.08 for SiCl_3 based on the work of Meeks *et al.*² Including Cl reassociation in the trench has a negligible effect on the etching characteristics due to its low rate compared to silicon chlorination and etching.

4.3. Typical Results

The geometry used in this study is an ICP reactor using a flat spiral four-turn coil set on a quartz window (See Fig. 2.1). This reactor is described in detail in Chapter 2. The process parameters are an $\text{Ar}/\text{Cl}_2 = 70/30$ gas mixture flowing at 150 sccm with 1 kW of ICP power at 13.56 MHz and a 150-V bias also at 13.56 MHz applied to the substrate. The gas phase plasma chemistry reaction mechanisms used are described in Ventzek *et al.*³ and Chapter 3 of this paper, as are typical plasma conditions. The 20-c-diameter wafer is modeled as silicon with a specified conductivity, a thin over coating of SiO_2 , polysilicon, and photo-resist. The subwafer structure is a dielectric ring with permittivity of $\epsilon/\epsilon_0 = 1.0$ located beneath and in contact with the wafer between radii of 4.5 and 6.25 cm. The superwafer topography is a clamp covering the outer 0.25 cm of the wafer. The dielectric ring approximates the effect of subwafer structures such as cooling channels or as might be used in the construction of an electrostatic chuck. Etch properties will be discussed at the three radial locations: (1) an open field site at a radius of $r = 3$ cm which is not affected by topography, (2) near the outer radius of the subwafer dielectric at $r = 6.0$ cm, and (3) near the clamp at $r = 9.625$ cm. Etch profiles were simulated for a resist opening of $0.6 \mu\text{m}$, a hard mask thickness of 0.2 mm , a 0.7-mm poly-Si layer, and an oxide etch

stop layer of 0.1 μm , as schematically shown in Fig. 4.1. The aspect ratio was increased by 2 or 3 for several simulations.

4.3.1. Plasma species flux distributions

The total ion and chlorine radical fluxes incident onto the wafer are shown in Fig. 4.2 as a function of radius. Their values at the inspection points and the corresponding etch rates are shown in Table 4.2. The etch rate is an average value given by the vertical distance etched divided by the etch time. Due to significant dissociation of the chlorine feedstock, the major ion incident onto the wafer is Cl^+ . As a result of its higher ionization potential and rapid charge exchange to Cl_2^+ and Cl^+ , the flux of Ar^+ is only 10% of the total. The magnitudes of the ion and radical fluxes are uniform to within about 10% to a radius beyond the dielectric ring. Adjacent to the clamp, the ion flux falls to approximately half its peak value, while the Cl atom flux decreases by 20%. There is a small peak in the ion flux at a radius of 5-6 cm due to the maximum in power deposition by the toroidal electric field. The PAD and PED for Cl atoms is essentially uniform across the radius with a small decrease in magnitude near the clamp due to shadowing. This results from the low reactive sticking coefficient (< 0.01) for Cl on nonsilicon surfaces. The PED is essentially thermal with a small high-energy tail extending to a few eV resulting from charge exchange with energetic ions. The PAD is essentially isotropic. The Cl radical flux is composed of 10% excited states although our etch mechanism is not sensitive to the excitation state of the radical.

The PED and PAD for the total ion flux striking the wafer at the three inspection points are shown in Fig. 4.3. For these cases, the wafer is treated as a perfect dielectric. The PED in the open field has the characteristic double-peaked shape associated with the thin sheaths encountered in high plasma density reactors.⁴ The ions acquire 0.5-1.0 eV of transverse energy crossing the presheath,⁵ which then requires ion acceleration across the

sheath of > 10 s V depth to straighten into anisotropic trajectories. The PAD is therefore generally broader at the lower energies of the PED where insufficient ion acceleration has occurred to counter the transverse component of ion energy entering the sheath. The major consequence of the subwafer dielectric is to reduce the sheath potential in the plasma at the surface of the wafer above the dielectric, thereby reducing the average ion energy to the substrate (see Table 4.2). As discussed in Hoekstra *et al.*,⁶ the subwafer dielectric acts as a capacitor which charges and discharges during the RF cycle, thereby garnering voltage which would have otherwise been dropped across the wafer or across the sheath. The sheath potential is therefore smaller above the dielectric, which then shifts the PED to lower energies. For these conditions, the drop in average ion energy is from 68 eV (at locations far from the dielectric) to 49 eV (above the dielectric). In principle, the subwafer dielectric should not have a major effect on the PAD, since the remaining sheath potential is generally sufficient to redirect ions vertically into the substrate. The 2D nature of the presheath, though, causes significant perturbations to the PED and PAD.

The ion PAD/PED for the location above the subwafer dielectric shown in Fig. 4.3(b) is asymmetric, having an offset to negative angles. It is also somewhat broader than that at the open field location. The broadening of the PAD results from the lower ion energy caused by the reduced sheath potential as described above. The asymmetry results from radial gradients in the presheath. The location at which this PAD is recorded is towards the outer edge of the subwafer dielectric. The sheath potential is lowest at the midpoint of the dielectric and increases to its open field value towards the edges of the dielectric. As a result, the sheath potential has a radial gradient, which in turn produces a transverse electric field in the presheath. The ions therefore enter the sheath with a net positive radial velocity. (On the inner side of the subwafer dielectric, the presheath produces a net negative radial ion velocity.) The asymmetry we observe in the PAD results from there being insufficient sheath voltage to straighten the ion trajectories to the

vertical. For this reason the angular offset is most prominent at low ion energies, and less severe at higher energies where additional sheath voltage is available to straighten the trajectories. The PAD/PED near the clamp has an even more severe asymmetry for essentially the same reason. The vertical clamp face produces a net radial electric field in the presheath which results in a net positive radial velocity for ions entering the sheath.

4.3.2. Predicted etch trench profiles

Predicted poly-Si etch profiles obtained with the MC-FPM after 500 s of etching are shown in Figs. 4.4(a), (b), and (c) for the open field, over the subwafer dielectric, and near the clamp, respectively. For these cases, there is no inhibitor flux. The etch profile in the open field is anisotropic with straight walls and clean corners. The etch rate at this location is 1800 Å/min. Our etch mechanism proceeds through an intermediate step where Cl atoms chlorinate the surface, forming SiCl_x species shown in yellow. SiCl_x is removed from the surface by ion bombardment and is therefore less prevalent near the bottom of the trench. This profile is representative of all wafer locations more than 1 cm distant from either the subwafer dielectric or the wafer clamp.

Product fluxes returning to the plasma from the trench were examined at the 3.0-cm radial location. In all cases, the fluxes returning to the plasma are dominated by Cl atoms resulting from either Cl which did not react on the surface or from the neutralized products of ion recombination. Early during the etch, the reactivity of Cl is high due to chlorination of the surface, and the ratio of the Cl flux to the SiCl_x flux leaving the trench is 40:1. After the surface is chlorinated, the ratio increases to as large as 600:1. When the oxide layer is reached there is a decrease in SiCl_x flux (some etching of the side wall continues to produce SiCl_x), and a small SiO_xCl_y flux appears as the oxide layer begins to etch at a lower rate. At this point the product flux ratios for Cl: SiCl_x : SiO_xCl_y are 2000:2:1.

The reduced ion energy at locations above the dielectric lowers the etch rate compared to the open field position, in this case to 1350 Å/min. The etch has had insufficient time to reach the SiO₂. If the polysilicon is doped n-type, the thermal etch rate by Cl atoms will be large. Since the Cl radical flux above the dielectric is essentially the same as that for the open field, the lower ion energy above the dielectric results in a lower vertical to horizontal etch rate, dropping to as low as 5:1 in the absence of side wall passivation. This produces rounded side walls, as shown in Fig. 4.4(b). An analogous situation occurs near the wafer clamp where the etch rate is still lower, 760 Å/min. Here the reduced etch rate results dominantly from a lower ion flux (as opposed to lower ion energy), approximately half that near the center of the wafer. The etch profiles for the above dielectric and near clamp locations after 500 s show indications of some increased undercutting due to the broadening of the PAD and an asymmetry due to the angular offset in the PAD.

The lower etch rates over the dielectric and near the wafer clamp require longer times to clear the bottom of the trench. The etch profiles obtained at these sites when the width of the trench at its base is approximately equal to the resist opening are shown in Figs. 4.5(a) and (b). The etch times are 720 s and 1050 s, respectively. Since the width of the PAD is not overtly perturbed by the subwafer dielectric, the width of the etch profile over the dielectric is similar to that of the open field with some small amount of additional undercutting due to the reduction in the vertical-to-horizontal etch rate. However, the angular offset of the PAD produces an asymmetric etch profile with more undercutting on the wall at the outer radius. The effect is more severe near the wafer clamp where the angular offset in the ion flux is more pronounced. The addition of an inhibitor flux can help lower the horizontal etch rate and narrow the profile. However the improvement is not as dramatic as at open field locations since there is now an increased ion flux to the sidewalls which removes the inhibitor. Deposition of inhibitor on the base of the trench

does also occur, which decreases the vertical etch rates leading to longer etch times, but the effect is not large due to the more rapid rate of removal by ion bombardment.

The degree of asymmetry of the etch profile above the subwafer dielectric increases with increasing etch depth. For example, etch profiles are shown in Fig. 4.6 in the open field ($r = 3$ cm) and above the subwafer dielectric ($r = 6$ cm) for trench depths of $0.7 \mu\text{m}$, $1.4 \mu\text{m}$, and $2.1 \mu\text{m}$. In all cases, the etch profile in the open field remains anisotropic, with a small amount of bowing for the deepest trench due to an uninhibited lateral thermal etch. Above the subwafer dielectric where the PAD/PED is perturbed and asymmetric, the etch profile is increasingly offset as the depth increases, though the slope of the inner wall is essentially the same. With increasing depth and etch time, the outer wall becomes increasingly more bowed.

The perturbation of the ion flux by subwafer dielectrics is a function, in part, of the electrical properties of a wafer. For example, a highly conductive wafer would appear to be an equipotential plane which electrically shields the plasma from structures below the wafer. The consequences of subwafer dielectrics are, then, most severe for lightly doped wafers having largely dielectric properties. As a demonstration of this effect, the total ion PAD/PED and etch profiles above the dielectric ring are shown in Fig. 4.7 for a perfect dielectric wafer and for a wafer conductivity of $0.05 \Omega^{-1}\text{cm}^{-1}$ without the use of an inhibitor flux. With the higher-conductivity wafer, the plasma is largely electrically shielded from the subwafer topography. As a result there is less perturbation of the sheath and presheath. The PAD and PED more closely resemble the open field distributions though there is still an angular offset. Although there is some undercutting, the larger ion energy obtained with the more conductive wafers increases the vertical etch rate to the open field value and recoups the anisotropic nature of the etch in spite of the uninhibited lateral thermal etch rate. However, there does remain a small asymmetry due to capacitive perturbation of the sheath and presheath.

The spontaneous thermal etching of n-type poly-Si can produce a significant undercutting of the mask and broadening of the etch profile. For example, the etch profile at $r = 6.0$ cm (above the dielectric) is shown in Fig. 4.8(a) for a dielectric wafer, without an inhibitor flux and without thermal etching. In Fig. 4.8(b), the spontaneous thermal etch probability by Cl atoms is 0.5%, which causes an increase in undercutting due to the broad PAD of the Cl atom flux. The anisotropic etch profile is recouped with an inhibitor flux which is 0.1% that of the Cl atom flux, as shown in Fig. 4.8(c).

The requirement for an inhibitor flux to produce anisotropic profiles is ultimately a function of the lateral-to-vertical etch rate, which in turn is a function of the PED/PAD and thermal etch rates. For a given thermal etch rate, however, there is an inhibitor flux producing side wall passivation which yields straight wall features. To illustrate this relationship, we defined a lateral etch ratio R as (average trench width)/(mask opening width). Ratio R as a function of thermal etch probability and inhibitor flux is shown in Fig. 4.9(a). When the lateral etch is large due to high thermal etch rates, R is large due to undercutting. Increasing inhibitor fluxes recoups the straight wall feature ($R = 1$). However, large inhibitor fluxes eventually cause loss of critical dimension, leading to narrowed features as seen in Fig. 4.9(b). We found that for a small thermal etch probability, an inhibitor flux 0.1% of the Cl atom flux gives the most satisfactory trench profiles.

Table 4.1. Surface Reactions for poly-Si Etch Mechanism

<u>Reaction</u> ^a	<u>Probability for Reaction</u> ^b	<u>Ref.</u>
$\text{Si}_{(s)} + \text{Cl}_{(g)} \rightarrow \text{SiCl}_{(s)}$	0.99	13
$\text{SiCl}_{(s)} + \text{Cl}_{(g)} \rightarrow \text{SiCl}_{2(s)}$	0.20	13
$\text{SiCl}_{2(s)} + \text{Cl}_{(g)} \rightarrow \text{SiCl}_{3(s)}$	0.15	13
$\text{SiCl}_{3(s)} + \text{Cl}_{(g)} \rightarrow \text{SiCl}_{4(s)}$	0.0001	13,c
$\text{Si}_{(s)} + \text{SiCl}_{2(g)} \rightarrow \text{Si}_{(s)} + \text{SiCl}_{2(s)}$	0.8	13
$\text{SiCl}_{(s)} + \text{SiCl}_{2(g)} \rightarrow \text{SiCl}_{(s)} + \text{SiCl}_{2(s)}$	0.5	13
$\text{SiCl}_{2(s)} + \text{SiCl}_{2(g)} \rightarrow \text{SiCl}_{2(s)} + \text{SiCl}_{2(s)}$	0.3	13
$\text{SiCl}_{3(s)} + \text{SiCl}_{2(g)} \rightarrow \text{SiCl}_{3(s)} + \text{SiCl}_{2(s)}$	0.1	13
$\text{SiCl}_{2(s)} + \text{Ar}^+ \rightarrow \text{SiCl}_{2(g)} + \text{Ar}_{(g)}$	$0.16 \sqrt{(\mathbf{e} - \mathbf{e}_o) / \mathbf{e}_o}$	12,d
$\text{SiCl}_{3(s)} + \text{Ar}^+ \rightarrow \text{SiCl}_{3(g)} + \text{Ar}_{(g)}$	$0.16 \sqrt{(\mathbf{e} - \mathbf{e}_o) / \mathbf{e}_o}$	12,d
$\text{SiCl}_{(s)} + \text{Cl}^+ \rightarrow \text{SiCl}_{2(g)}$	$0.13 \sqrt{(\mathbf{e} - \mathbf{e}_o) / \mathbf{e}_o}$	12,d
$\text{SiCl}_{2(s)} + \text{Si}_{(s)} + \text{Cl}^+ \rightarrow \text{SiCl}_{2(g)} + \text{SiCl}_{(s)}$	$0.16 \sqrt{(\mathbf{e} - \mathbf{e}_o) / \mathbf{e}_o}$	12,d
$\text{SiCl}_{3(s)} + \text{Cl}^+ \rightarrow \text{SiCl}_{4(g)}$	$0.19 \sqrt{(\mathbf{e} - \mathbf{e}_o) / \mathbf{e}_o}$	12,d
$\text{Si}_{(s)} + \text{Cl}_2^+ \rightarrow \text{SiCl}_{2(g)}$	$0.13 \sqrt{(\mathbf{e} - \mathbf{e}_o) / \mathbf{e}_o}$	12,d
$\text{SiCl}_{(s)} + \text{Si}_{(s)} + \text{Cl}_2^+ \rightarrow \text{SiCl}_{2(g)} + \text{SiCl}_{(s)}$	$0.16 \sqrt{(\mathbf{e} - \mathbf{e}_o) / \mathbf{e}_o}$	12,d
$\text{SiCl}_{2(s)} + \text{Si}_{(s)} + \text{Cl}_2^+ \rightarrow \text{SiCl}_{2(g)} + \text{SiCl}_{2(s)}$	$0.16 \sqrt{(\mathbf{e} - \mathbf{e}_o) / \mathbf{e}_o}$	12,d
$\text{SiCl}_{3(s)} + \text{Si}_{(s)} + \text{Cl}_2^+ \rightarrow \text{SiCl}_{4(g)} + \text{SiCl}_{(s)}$	$0.19 \sqrt{(\mathbf{e} - \mathbf{e}_o) / \mathbf{e}_o}$	12,d

^aSubscript (s) denotes a surface species. Subscript (g) denotes a gas or plasma species.

^b \mathbf{e} is the ion energy. $\mathbf{e}_o = 10$ eV unless noted otherwise.

^cThermal etch probability was varied for some cases as noted.

^dReaction mechanism was derived from the cited reference. The precise values for probabilities have been modified.

Table 4.2: Reactant and Etch Characteristics at the Inspection Points

	Radius (cm)		
	3.0	6.0	9.625
Total Ion Flux ($\text{cm}^{-2}\text{s}^{-1}$)	2.2×10^{16}	2.3×10^{16}	1.2×10^{16}
Average Ion Energy (eV)	68	49	69
Cl Atom Flux ($\text{cm}^{-2}\text{s}^{-1}$)	5.6×10^{17}	5.4×10^{17}	3.9×10^{17}
poly-Si Etch Rate (Å/min)	1800	1350	760

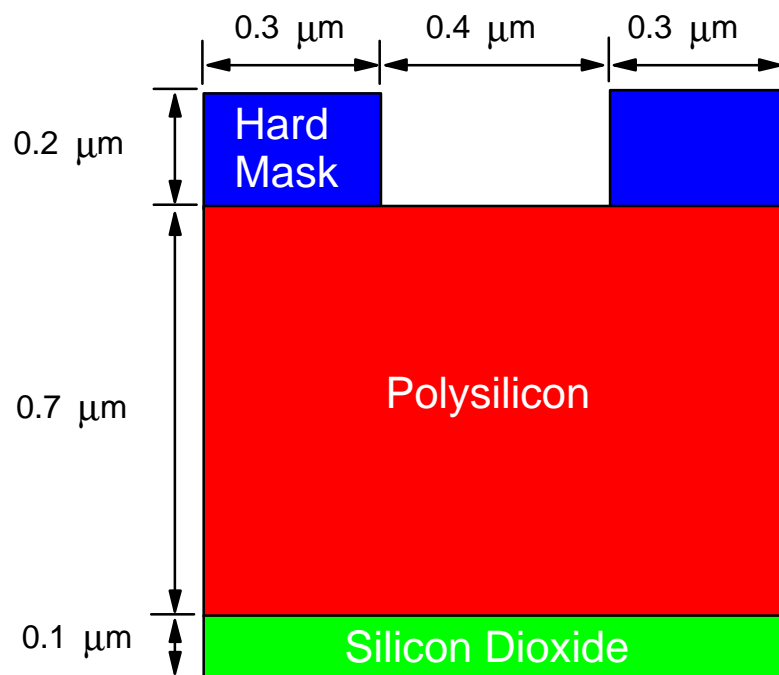


Fig. 4.1. Initial feature profile used for 1:1 aspect ratio cases.

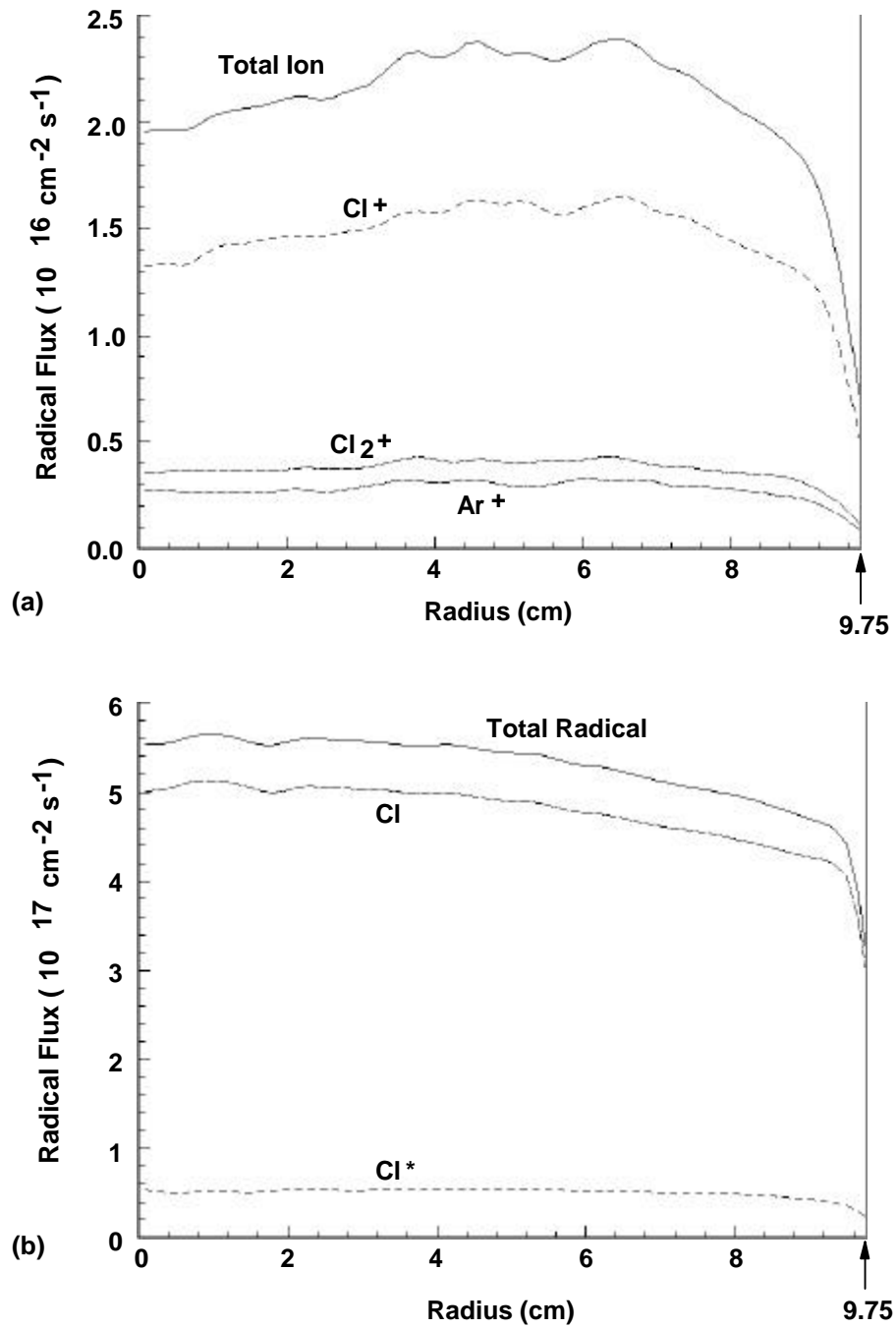


Fig. 4.2. (a) Ion and (b) Cl radical fluxes striking the wafer as a function of radius for an ICP reactor, Ar/Cl₂(70/30), 10 mTorr, 1-kW ICP power, and 150-V bias on the substrate.

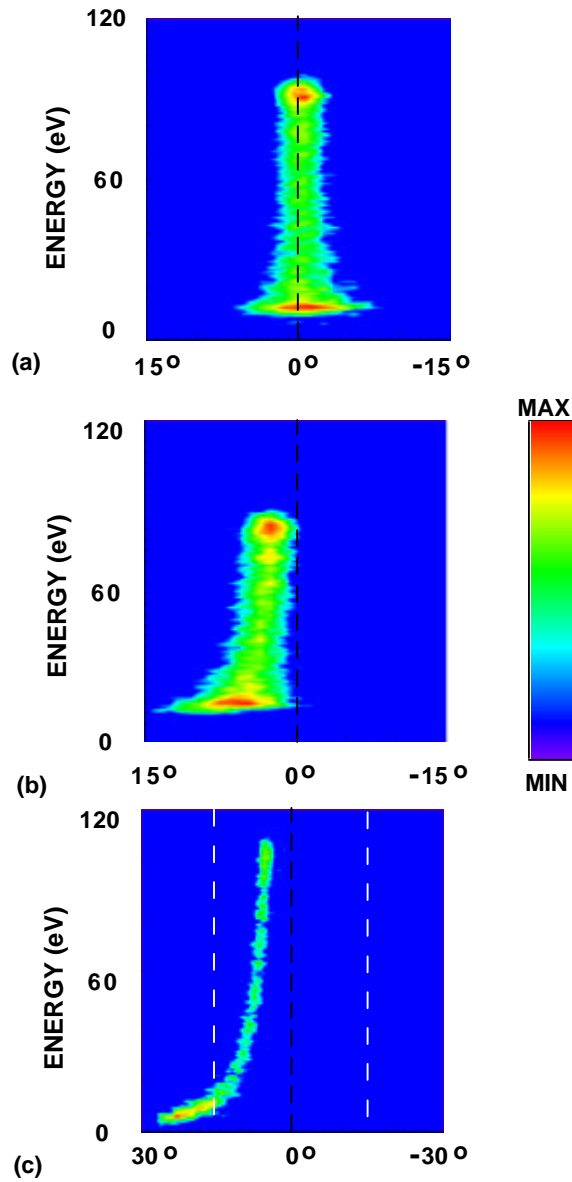


Fig. 4.3. Total ion energy and angular distributions striking the wafer for (a) the open field ($r=3$ cm), (b) above the subwafer dielectric ($r=6$ cm), and (c) adjacent to the wafer clamp ($r=9.625$ cm). Due to the voltage division between the sheath and the subwafer dielectric, the ion energy is reduced. The angular distributions above the dielectric and near the clamp are asymmetric due to presheath perturbation.

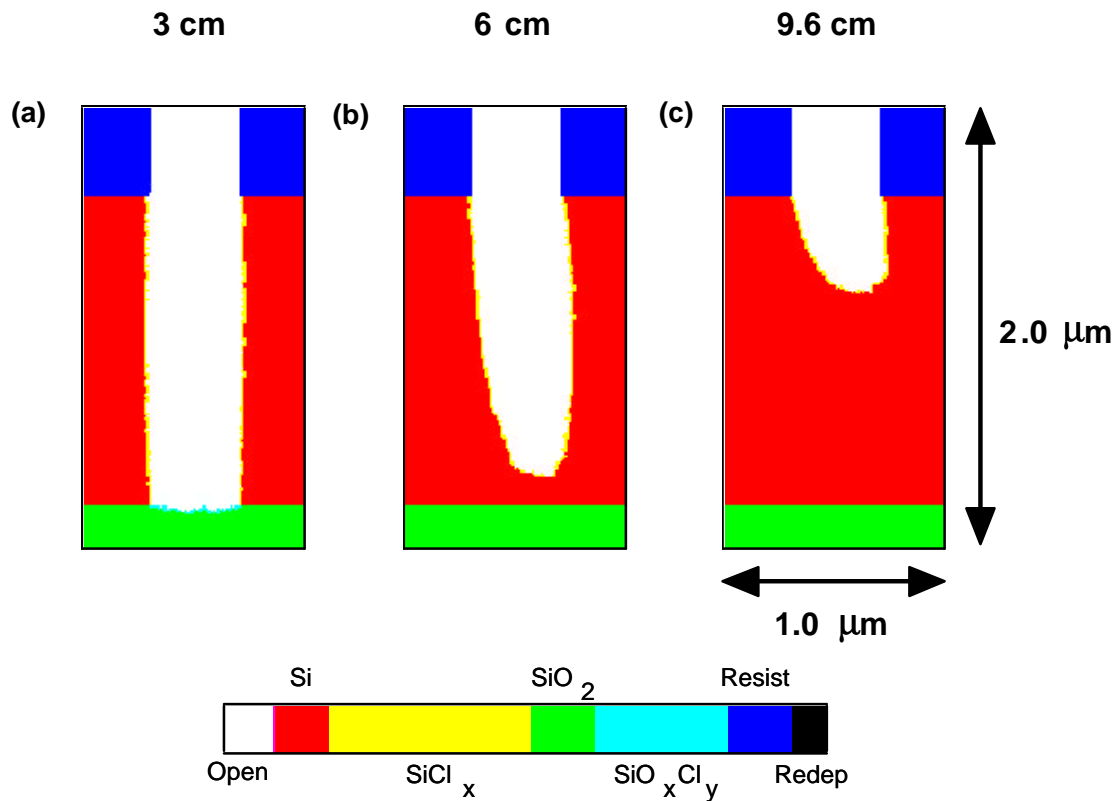


Fig. 4.4. Polysilicon feature profiles after a 500-s etch at radii of (a) 3, (b) 6, and (c) 9.625 cm. The etch rates are decreased and asymmetries occur above the dielectric and near the clamp.

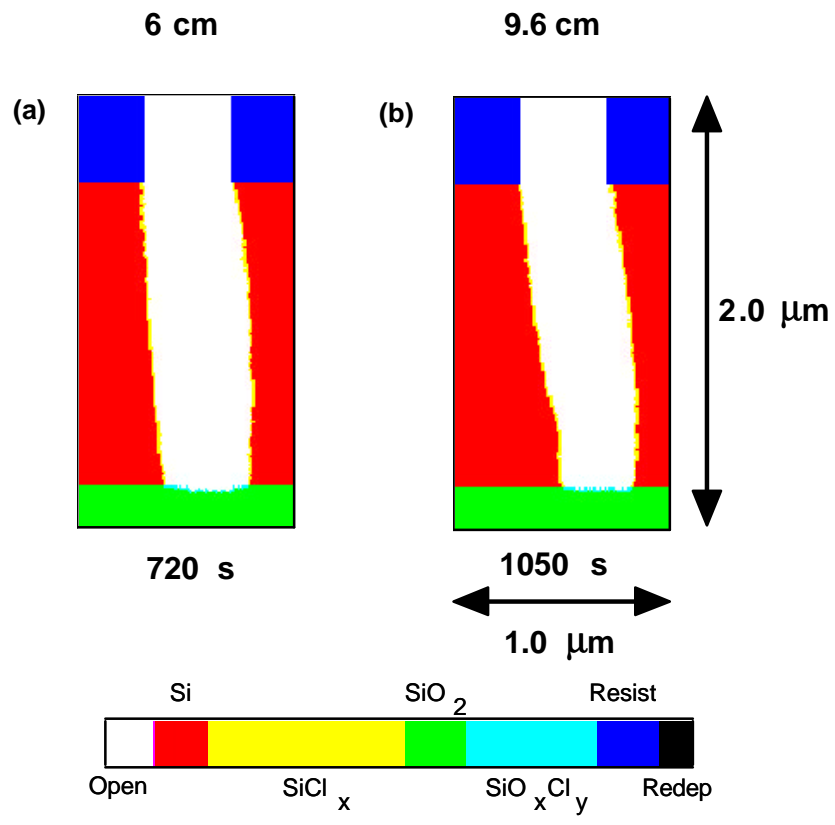


Fig. 4.5. Etch profiles for (a) $r = 6$ cm, $t = 720$ s and (b) $r = 9.625$ cm, $t = 1050$ s demonstrating the necessary overetch to clear features in these regions.

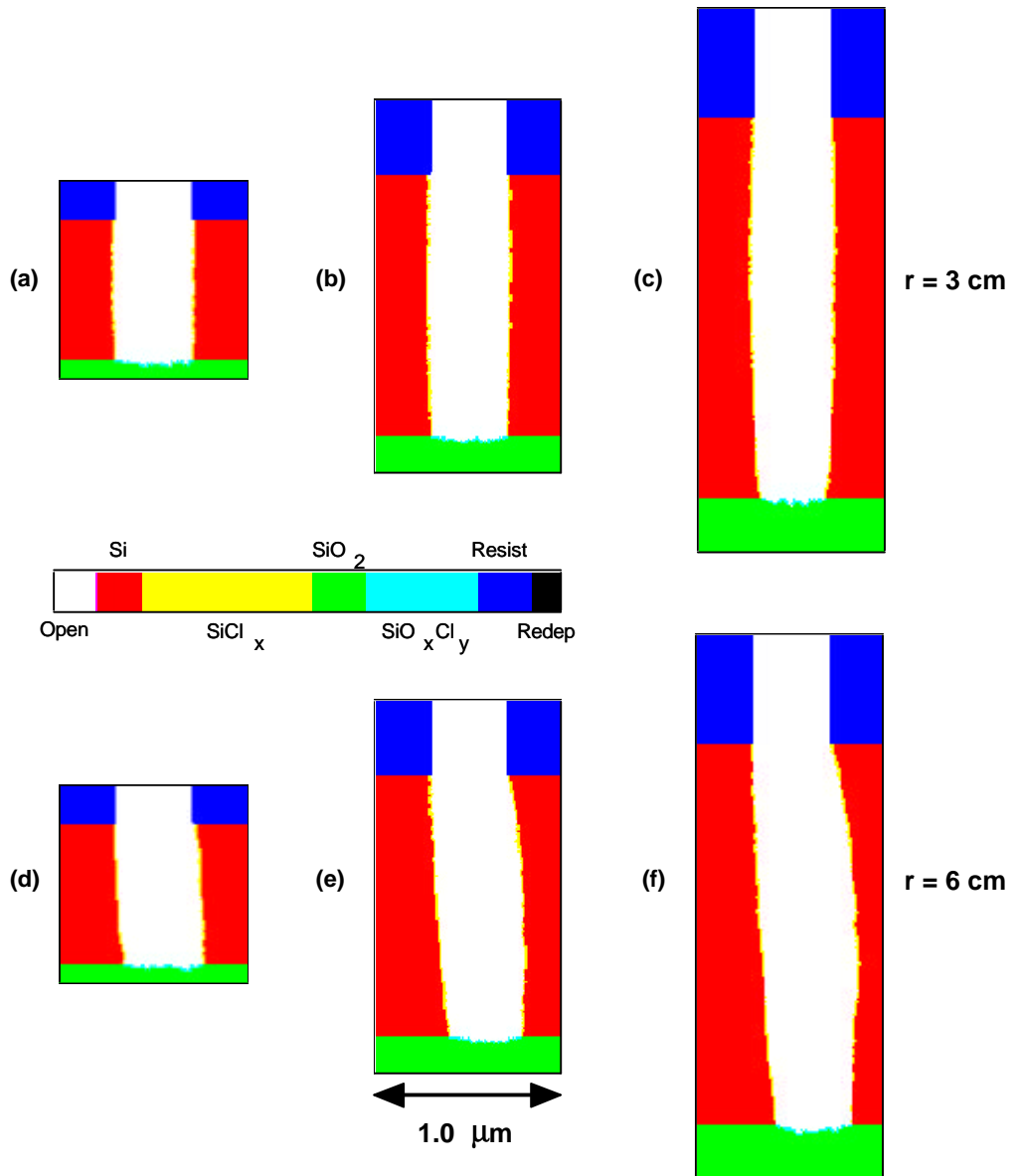


Fig. 4.6. Etch profiles at $r = 3$ cm (open field) for aspect ratios of (a) 1:1, (b) 1:2, and (c) 1:3 and etch profiles at $r = 6$ cm (above the dielectric) for aspect ratios of (d) 1:1, (e) 1:2, and (f) 1:3.

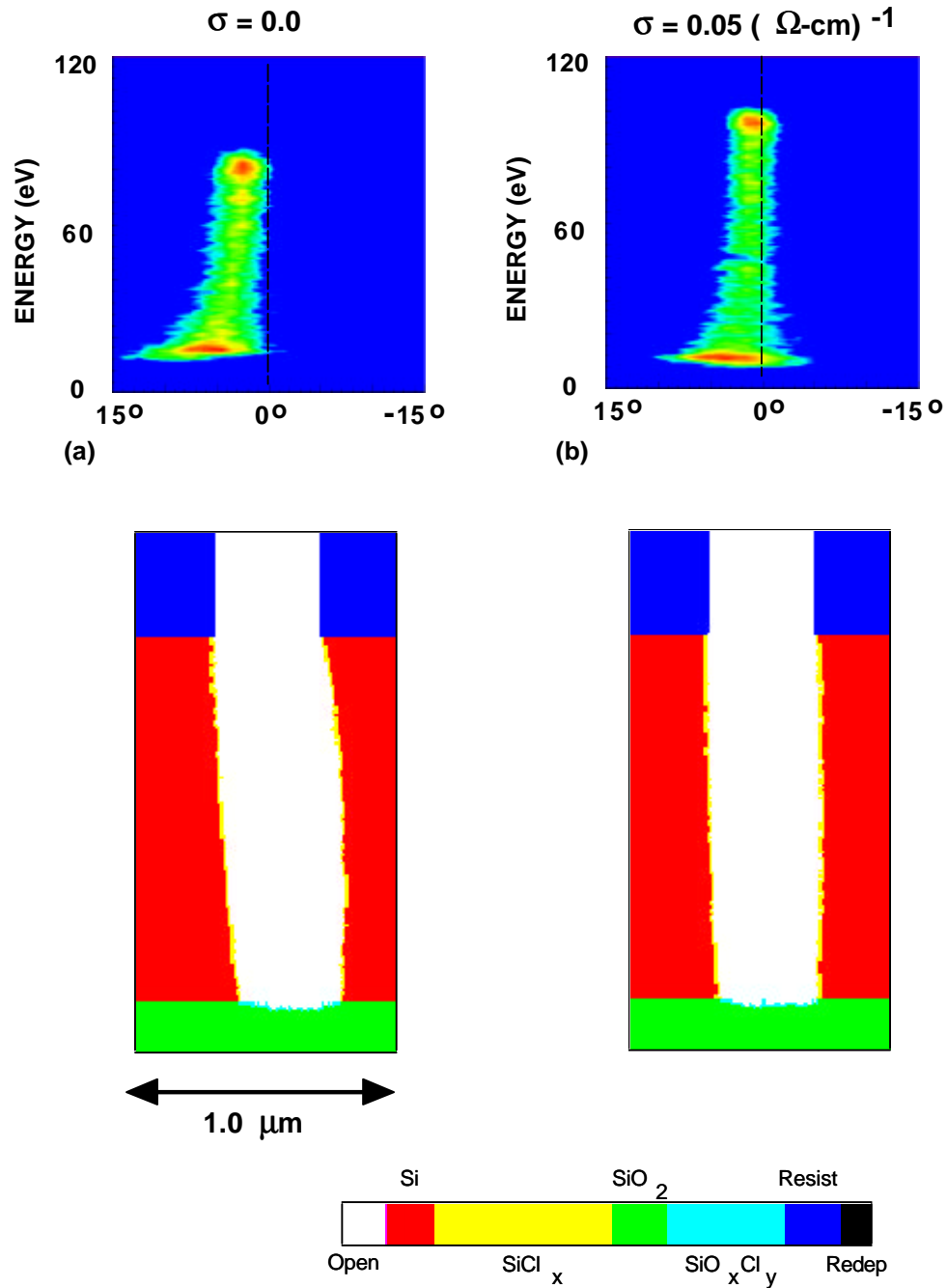


Fig. 4.7. Comparison of etch profiles and total ion PEAD above the subwafer dielectric, $r = 6 \text{ cm}$, for (a) a perfect dielectric wafer and (b) a wafer with conductivity of $0.05 \text{ }\Omega^{-1}\text{cm}^{-1}$. The finite conductivity “shields” the plasma from electrical nonuniformities below the wafer.

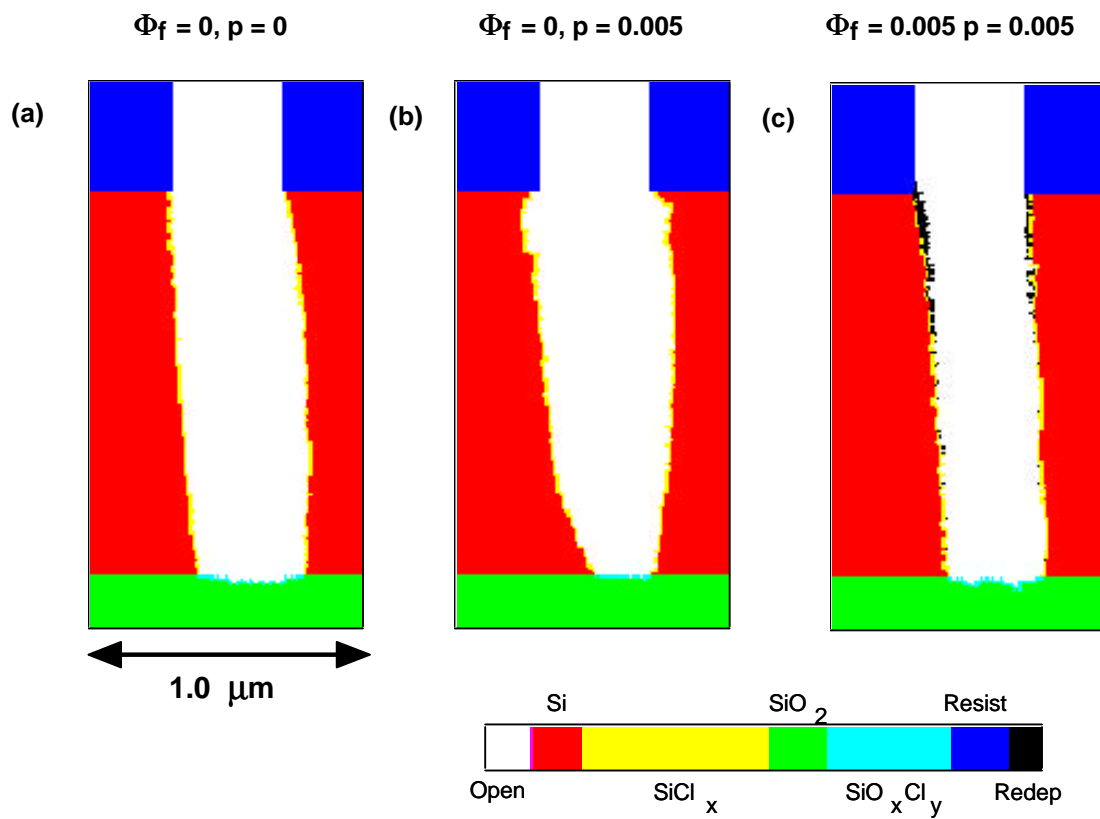
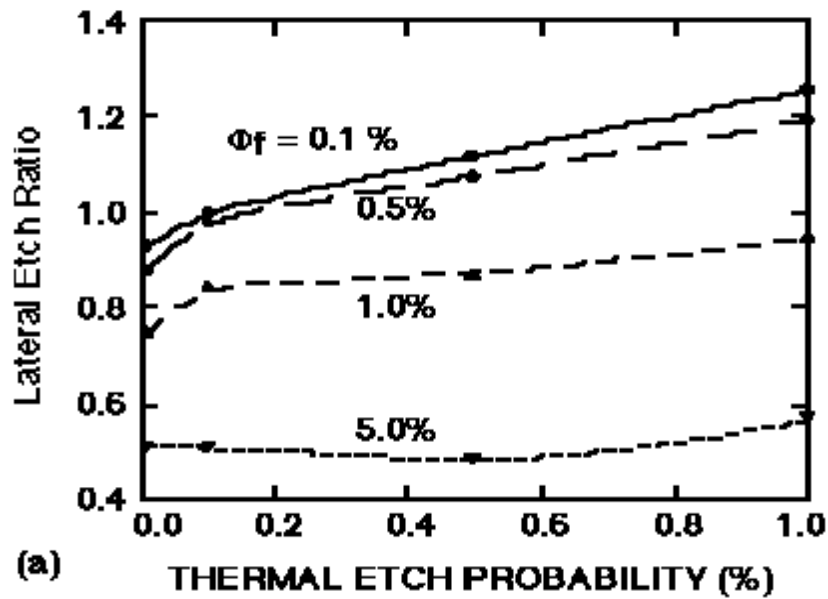
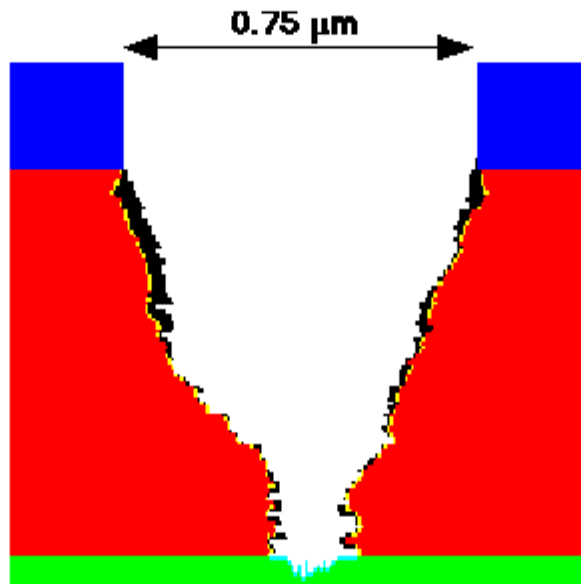


Fig. 4.8. Etch profiles above the subwafer dielectric ($r = 6$ cm) for different combinations of the inhibitor flux ϕ_f , and the thermal Cl etch probability p . Flux ϕ_f is expressed as a fraction of the Cl radical flux, (a) $\phi_f = 0.0, p = 0.0$, (b) $\phi_f = 0.0, p = 0.005$, and (c) $\phi_f = 0.001, p = 0.005$.



(a)



(b)

Fig. 4.9. (a) Etch profile shape factor (avg. feature width)/mask opening width) as a function of the Cl radical thermal etch probability. Shape factors are shown for different values of the inhibitor flux ϕ_f . (b) For large fluxes of inhibitor, the feature profile begins to choke off due to the rapid inward taper of the sidewalls.

4.4. References

1. C. C. Cheng, K. V. Guin, V. M. Donnelly, and I. P. Herman, *J. Vac. Sci. Technol. A* **12**, 2630 (1994).
2. E. Meeks, Sandia National Laboratory, private communication, 1995.
3. P. L. G. Ventzek, M. J. Grapperhaus, and M. J. Kushner, *J. Vac. Sci. Technol. B* **16**, 3118 (1994).
4. R. J. Hoekstra and M. J. Kushner, *J. Appl. Phys.* **77**, 3668 (1995).
5. J. Zheng, R. P. Brinkman, and J. P. McVittie, *J. Vac. Sci. Tech. A* **13**, 859 (1995).
6. R. J. Hoekstra and M. J. Kushner, *J. Appl. Phys.* **79**, 2275 (1996).

5. PROCESSES IN PLASMA ETCHING OF SILICON

5.1. Introduction

As computational plasma equipment models have matured, the ability to predict etch effects at the feature level has increased. For these small feature sizes (0.25 μm and below), the shape of the etched profile (sidewall slope, trench bottom shape, etc.) can have a dramatic effect on the device performance and yield. Using feature profile models, prediction of these profile shapes based on plasma and reactor parameters has become possible by coupling the profile model with a plasma equipment model. Models have been used to predict profile evolution for polysilicon etching as well as other systems.¹⁻³

In this chapter, important processes involved in plasma etching of silicon are examined. This includes the effects of energy and angle of incoming plasma species upon the ion-enhanced etch process. Based on experimental results described in Section 5.2, comparison of profile evolution for different angular dependencies of etch yield is presented. The process of specular reflection and its role in flux enhancement near sidewalls are described in Section 5.3. Currently, there is a lack of information on the energy and angular dependence of specular reflection although both molecular dynamics simulations⁴ and VFTRIM⁵ show promising results for low energy (10s-100s eV) grazing angle ($>60^\circ$) impacts. Parameterization of these dependencies is described in Section 5.4 to determine their effect on sidewall slope and relative microtrench depth and width. Utilizing the energy and angular dependence as well as including the specular reflection allows comparison to experimental results, showing good agreement for time evolution and substrate bias variation in Section 5.5. Finally in Section 5.6, initial results are presented for self-consistent charging of the profile and resulting perturbation of the profile.

5.2. Specular Reflection

The phenomenon of “microtrenching” has become an issue as industry has moved to high-density plasma (HDP) etching systems to increase yield and throughput. For these systems, the relative ion flux to the surface is greater and has larger average energies. The impact of these high-energy particles at grazing angles ($< 10^\circ$) can lead to specular reflection depicted in Fig. 5.1(a), where the particle retains a large fraction ($>90\%$) of its energy and directionality. This effect leads to “focusing” of the high-energy particles at the bottom of features near the sidewalls of the feature. This “focusing” produces enhanced etching in these regions and leads to what is commonly known as microtrenching. This effect was first seen by Nguyen *et al.*,⁶ and the concept of specular reflection as a cause was first presented by Dalton *et al.*⁷ Microtrenching can lead to large differences in etch depth across the bottom of features and the possibility of “punch-through” on etch stops or other thin layers such as gate oxide in the microtrenched regions of the feature.

In this section, the MCFPM coupled with the HPEM was used to examine the effects of specular reflection of high-energy grazing angle impacts on etch profile evolution. All experimental and model results included in this paper were produced for an inductively coupled LAM 9400SC type reactor. The reactor parameters were as follows: 600-W ICP, 100-W chuck bias, 10 mTorr, and 60-sccm chlorine. The main subfeature examined was the generation of “microtrenching” at the corners of the two-dimensional (2D) resolved trench. The experimental beam results by Chang *et al.*⁸ for the angular etch yield dependence of chlorine atomic ions on silicon described in Section 5.3 and the assumption that ions retain as much as 99% of their energy when reflecting at grazing angles ($<10^\circ$ from surface tangent), based on the molecular dynamics results of Helmer and Graves,⁴ are utilized in the Monte Carlo Feature Profile Model (MCFPM). In Fig. 5.2,

the effect is demonstrated for specular reflection in a trench with perfectly vertical sidewalls shown in Fig. 5.1(b). With the addition of the flux due to specularly reflected ions, the flux near the corners of the trench is increased to be comparable with the flux at the center of the trench, indicating the “mirror-like” boundary condition at the sidewall. For self-consistently etched profiles including the specular reflection, the development of the sidewall slope can produce a “focusing” of the ion flux and dramatically enhance the flux to the corners, thereby producing microtrenching. The total ion energy and angular distributions (IEAD) are shown in Fig 5.3(a,b) for 100-W and 60-W RF bias, indicating the broad range of energies for incoming ions (10-110 eV and 10-70 eV) as well as the narrow angular distribution ($<5^\circ$). In Fig. 5.3(c,b), the total ion energy distributions (IEDs) are seen to have broadened, double-peaked distributions described in Chapter 3.

To demonstrate the dependence of “microtrenching” on specular reflection, the fraction of grazing ions allowed to retain their energy was varied from 0 to 95%. In Fig 5.4, the resulting profiles show a dramatic change in trench bottom morphology. As the fraction of spectral reflection is increased, the trench corners advance from being very rounded at 0%, to sharp and square at 50%, and to “microtrenched” at 95% as seen in experiments. This change in the corner development of the profiles is a direct result of ion reflection at the sidewalls leading to “focusing” or enhancement of the ion flux in these regions and an increased relative etch rate.

The slope of the resist sidewall can play a strong role in the initial development of microtrenching in these trenches. A finite slope allows a greater relative area for the incoming flux to reflect from and increases the resulting ion flux at the trench corners. Fig. 5.5 demonstrates the effect of increasing the resist sidewall slope from 0° to 4° . As the sidewall slope is increased the microtrenching becomes more pronounced. As the trench depth increases, the relative sidewall area of the resist decreases in relation to the

etched trench sidewall. This results in a decrease in the effect of resist sidewall slope for deeper etch features.

5.3. Angular-Dependent Etch Yield

The general sputter yield dependence on incident angle has been shown to be depressed at near normal angles and at a maximum for $\sim 60^\circ$. The molecular dynamics results by Hanson *et al.*⁹ agree with this dependence. However, the experimental beam results by Chang *et al.*⁷ show a broad maximum in etch yield from 0° to 40° with a gradual roll-off approaching 90° . This points to the mechanism for ion-enhanced etching differing from simple sputtering. In Fig. 5.6, the effects of angular-dependent etch yield on profile shape, specifically microtrenching, are shown. The resist sidewalls are sloped by 2° , allowing greater reflected ion flux and increasing the focusing effect. In part (a), with no angular dependence of the yield, the sidewalls of the trench “bow” outward decreasing the effect of specular focusing and producing no microtrenching. Using the results of Hanson *et al.*⁹ results in microtrench formation, which is broadened and almost vertical sidewalls as shown in part (b). The profile produced in part (c) resulted from the Chang *et al.*⁶ results and created the strongest microtrenching and well as the greatest sidewall slope due to the decrease in yield at high incident angles.

5.4. Angular and Energy Dependence of Specular Reflection

To determine the relative effects of the energy and angular dependence of specular reflection of ions, the MC-FPM was used to determine the resulting trench profiles produced for various energy and angular cutoffs. The cutoff angle for specular reflection was varied from 10° to 80° to determine what angular fraction of ions were specular reflecting. The cutoff energy was varied from 50 eV to 100 eV, where specular energy

retained was equal to 100% above the cutoff energy and decreased linearly to 0% at 0 eV. These angular and energy dependencies are shown graphically in Fig. 5.7.

Fig. 5.8 indicates the resulting profiles produced for the given ranges of cutoff angle and energy. For simulations where the ions were allowed to specularly reflect for angles less than 50° from the surface normal, the microtrench formation is much larger than seen in experiment. As the cutoff angle is increased beyond 60° , the microtrench formation is strongly reduced. Also, for large cutoff energies (>75 eV), the microtrenching decreases dramatically. This suggests that the angular cutoff for specular reflection is in the range of 30 - 60° and the cutoff energy is well below 75 eV, on the order of 50 eV or less.

5.5. Comparison to Experiment

Initial efforts have been made to compare the model results to experiment. In Fig. 5.9, profiles generated by the model are compared to experimental SEMs from LSI Logic Corporation for the same reactor conditions of 600 -W ICP power, 50 -W RF bias power at 10 mTorr of chlorine. The model utilized a 0.4 - μm resist layer which was not allowed to etch while the experimental profiles used a 0.2 - μm hard mask which etched at a rate approximately 5% that of the silicon. As can be seen from the results, the etch rate and evolution of the microtrenches for the model qualitatively follow those of the experiment. As the trench deepens, the model shows more dramatic broadening of the microtrenches, most probably due to the finite resolution of the model versus the continuum nature of the experimental results.

The effects of variation of RF biasing of the wafer chuck have also been compared for the model and experimental SEM results from LSI Logic Corporation. For the same conditions as described above the bias was varied from 0 W to 50 W to 100 W. As expected, the etch rate shown in both the model and experiment increases dramatically as

the bias is increased from 0 W. The experimental and modeled trench depths for all three biases compare well, as seen in Fig. 5.10. However, as the bias increases to 100 W, the experimental profile shows a dramatic increase in microtrench depth, whereas the model produces a smaller degree of microtrenching. The dramatic increase in microtrench depth for the experimental results can likely be attributed to the development of the interior sidewall of the microtrench. This region acts in the same fashion as the trench sidewall, increasing the focused flux at the bottom of the trench and enhancing the microtrenching rate. For the model, the resolution of the case did not allow formation of this interior sidewall to produce enhanced microtrenching due to noise considerations.

5.6. Surface Charging and Perturbation of Feature Evolution

As described in Chapter 4, the effects of surface charging and the resulting electric fields on profile evolution have been incorporated into the model. Due to the relatively long convergence time of the Poisson solution, few cases have been examined and only at low resolution (50×100 cells). Fig. 5.11 demonstrates the effect of nonuniform charging without the addition of a self-consistent electric field. Due to the broad angular distribution of the electrons and the narrow angular distribution of the ions, the edges of the resist become negatively charged and the bottom of the resist becomes positively charged.

For self-consistent electric fields and charge motion, where the charge diffusion coefficient was defined as $100 \text{ cm}^2/\text{s}$ for the silicon material and $10 \text{ cm}^2/\text{s}$ for the oxide and photoresist, the perturbation of the charged particle motion and the resulting change in feature evolution can be seen in Fig. 5.12. The positively charged ions are pushed to the trench corners by the effects of the positive charge buildup at the bottom of the trench, producing the beginnings of an hourglass shape as predicted by Gottscho *et al.*¹⁰ In Fig. 5.13, the potential distribution and the electric fields due to the nonuniform charging of

the material are shown, indicating the effect of the electric field on motion of charged species.

5.7. Summary

In conclusion, the profile evolution of etch features for chlorine etching of silicon has been examined to determine the relative effects of several processes on the resulting profile shape. The angular dependence of etch yield has shown that the results by Chang *et al.*,⁷ which have decreased etch yields for grazing angle ions, increase the inward taper of sidewalls and lead to microtrench development when included with the specular reflection process. The specular reflection process and the angular-dependent etch yield combine to “focus” ions at the corners of the profile, producing etch enhancement and microtrenching. The energy and angular dependence of specular reflection control the evolution of the resulting microtrenching. Parameterization of these dependencies has lead to the determination of probable ranges of 30-60° for an angular cutoff and a energy cutoff less than or equal to 50 eV. Comparison to experimental SEMs shows very good agreement with the model results for both substrate bias variation and time evolution. Limited examination of charging effects for these trenches has also been examined, indicating the possible perturbations of profile development that are possible due to non-uniform charging of the profile surface.

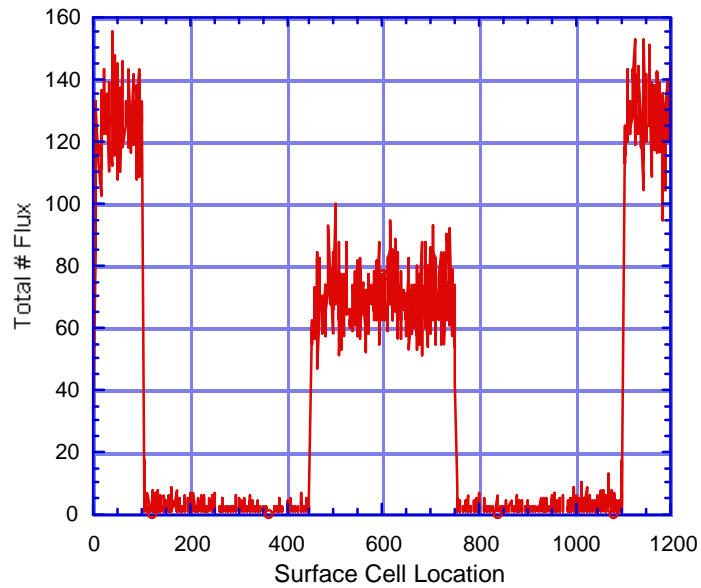
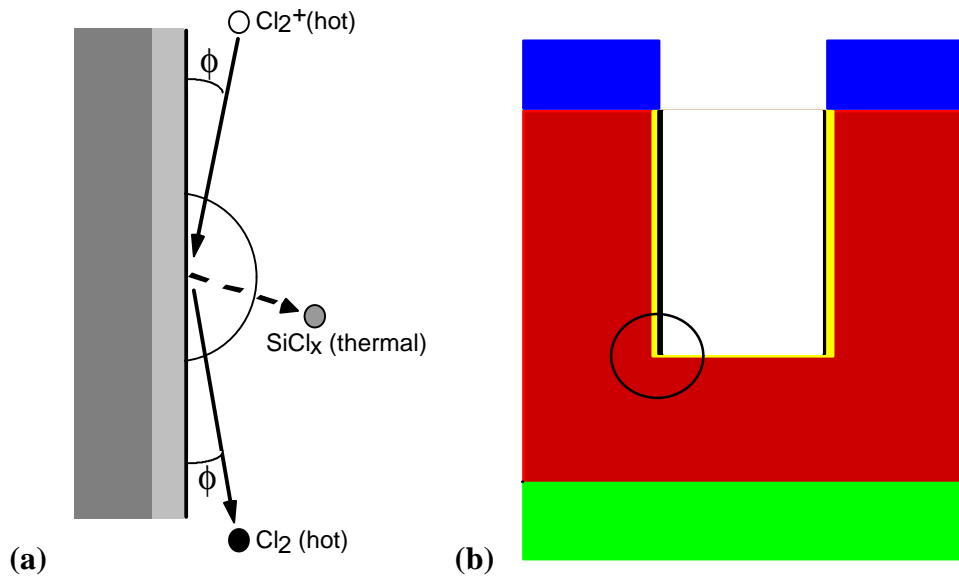


Fig. 5.1. (a) High-energy ions are capable of specularly reflecting from surfaces for high incident-angle impacts. (b) This ion-specular reflection can increase the relative flux to the corners of etched trenches. (c) Flux distribution along surface of etch trench. Note that the anisotropic ion flux impacts preferentially on horizontal surfaces.

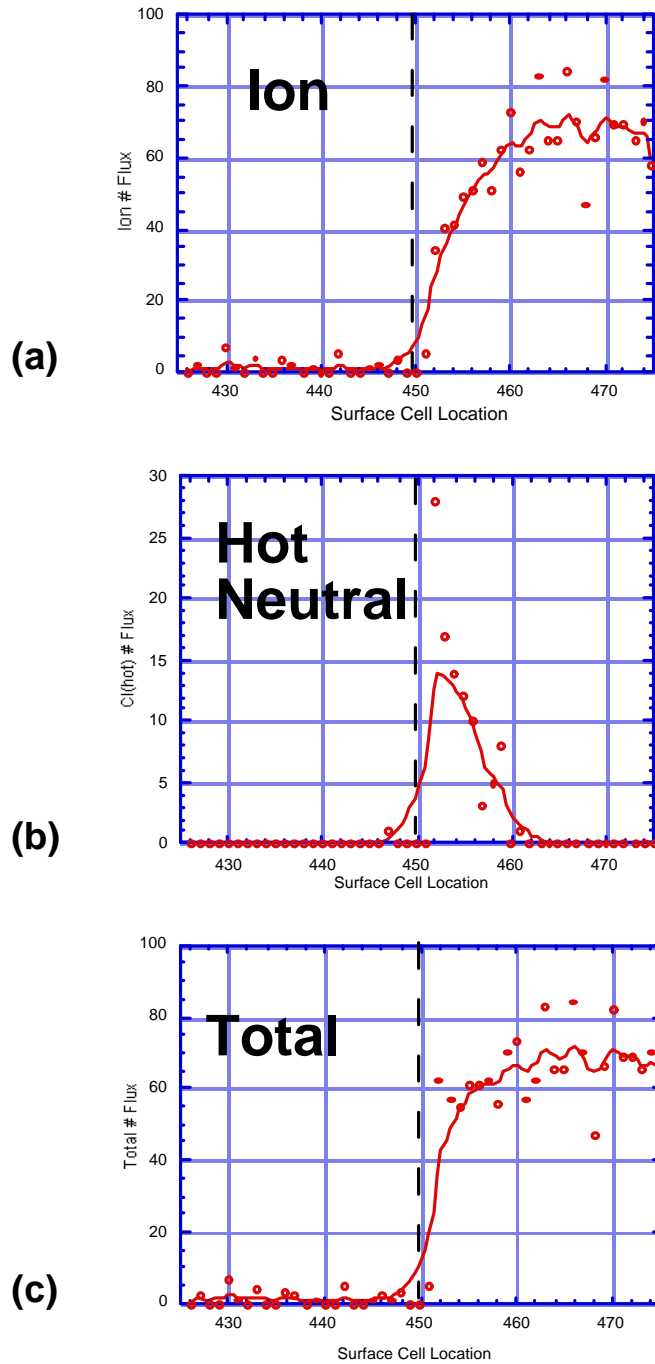


Fig. 5.2. Flux distribution at the trench corner indicated in Fig. 5.1(b) for (a) no specular reflection, (b) the additional flux due to specular reflection, and (c) the total flux. In the corner region, the specularly reflected flux increases the total flux and affects the corner evolution.

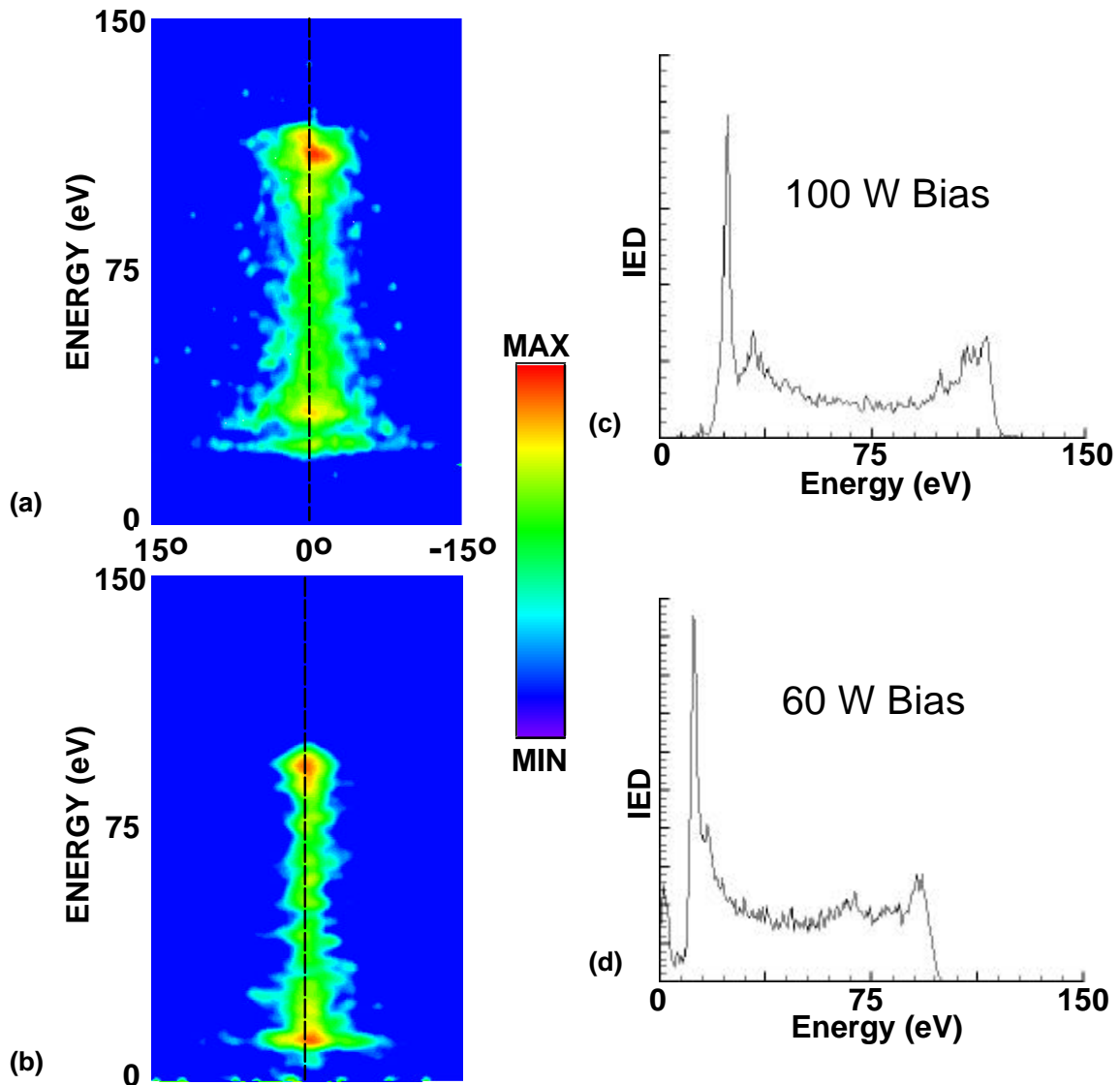


Fig. 5.3. Energy and angular distributions for total ion flux with reactor conditions of 600-W ICP, 10-mTorr Cl_2 , and (a) 100-W and (b) 60-W RF bias. Total ion energy distributions for (c) 100-W and (d) 60-W RF bias.

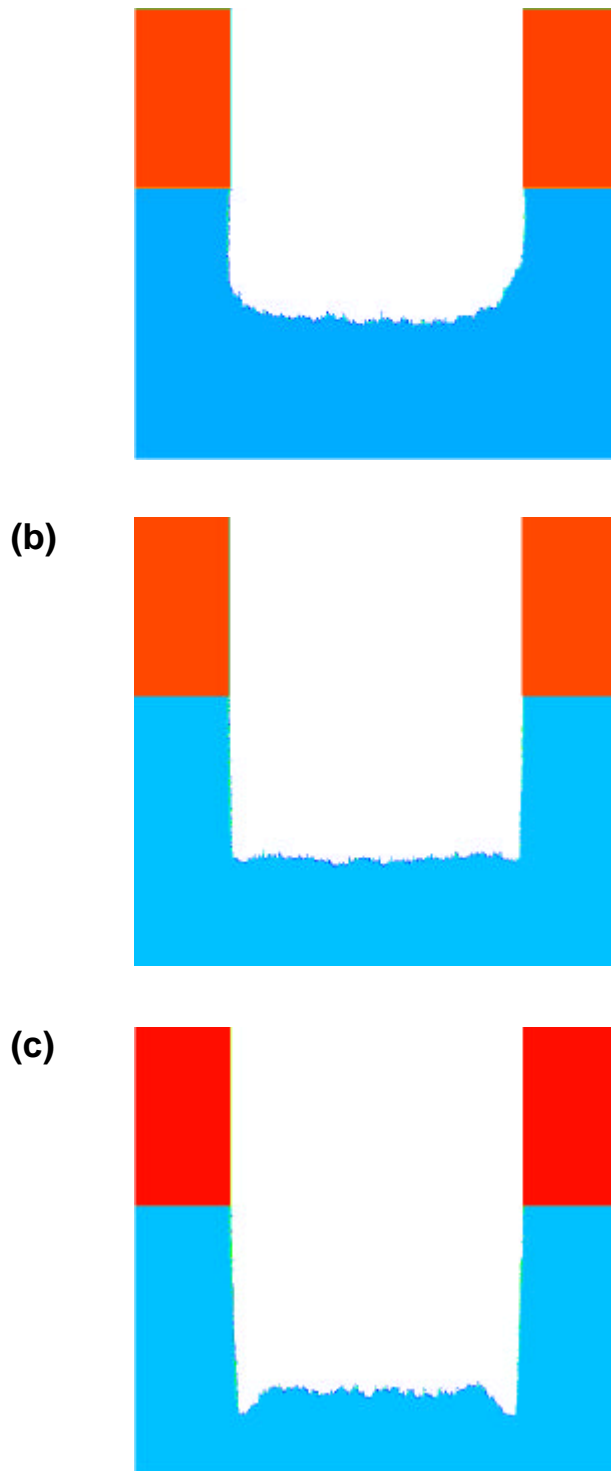


Fig. 5.4. Etch profiles for (a) 0%, (b) 50%, and (c) 95% specular energy retain upon reflection.

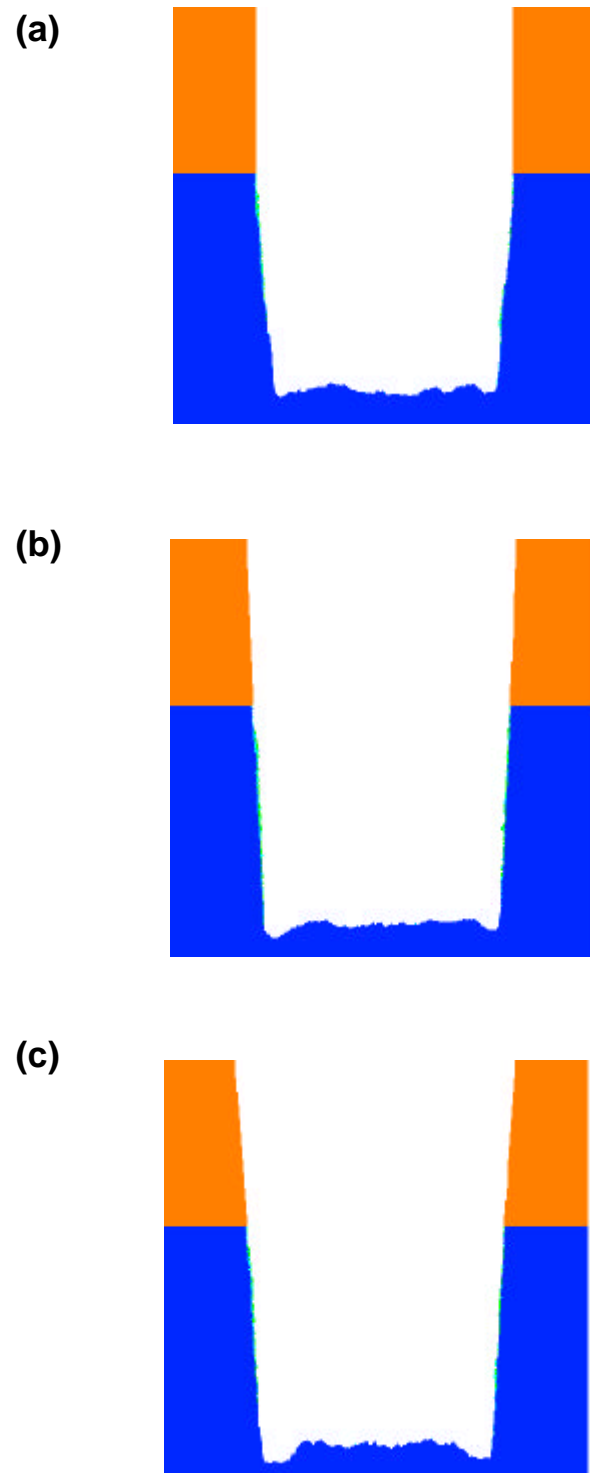


Fig. 5.5. Etch profiles generated for sidewall angles of (a) 0°, (b) 2°, and (c) 4°.

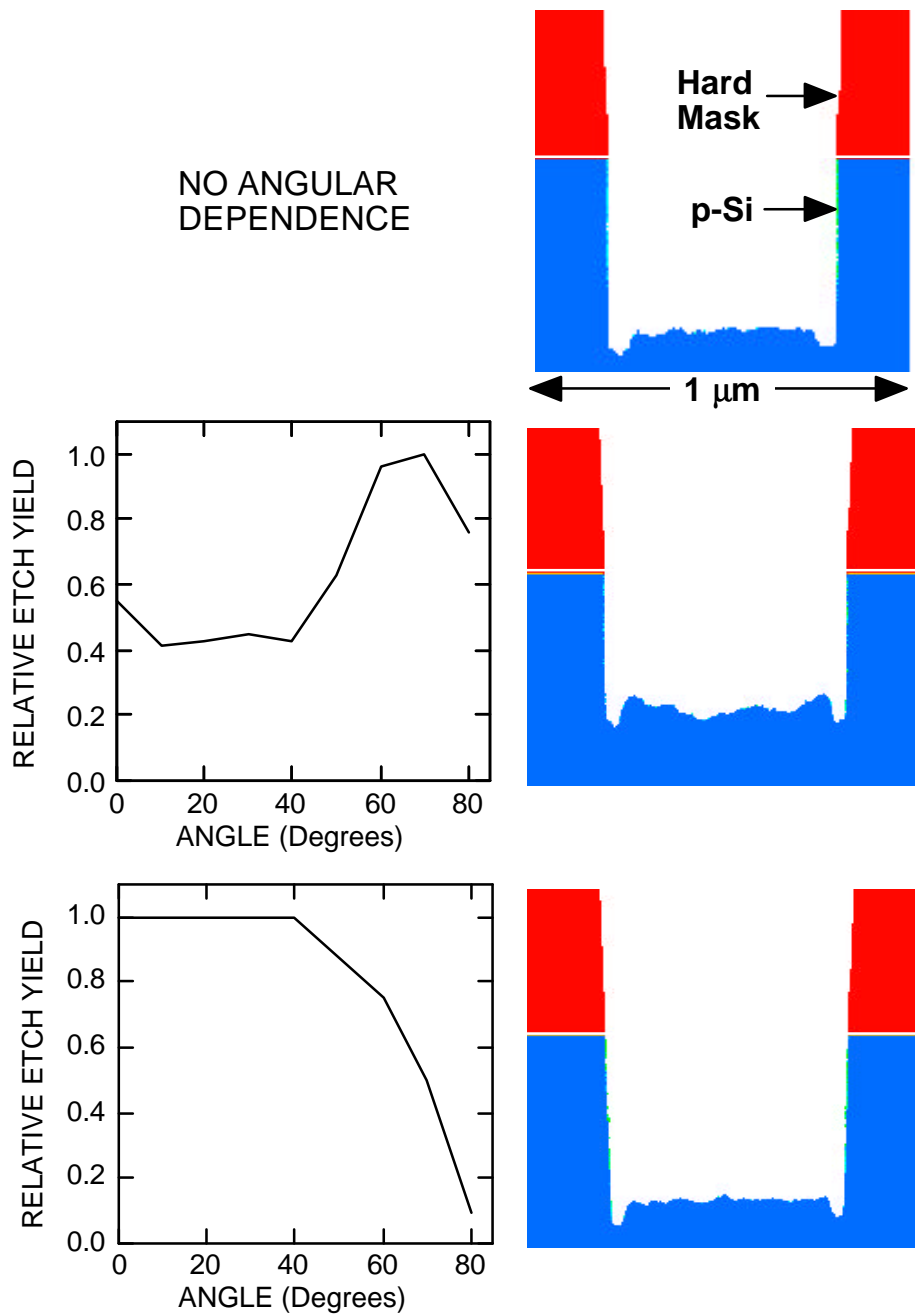


Fig. 5.6. Etch profiles for angular etch yield dependencies of (a) none, (b) sputter type dependence based on Hanson *et al.*⁸ molecular dynamics results, and (c) ion-enhanced etch dependence based on Chang and Sawin⁶ experimental results.

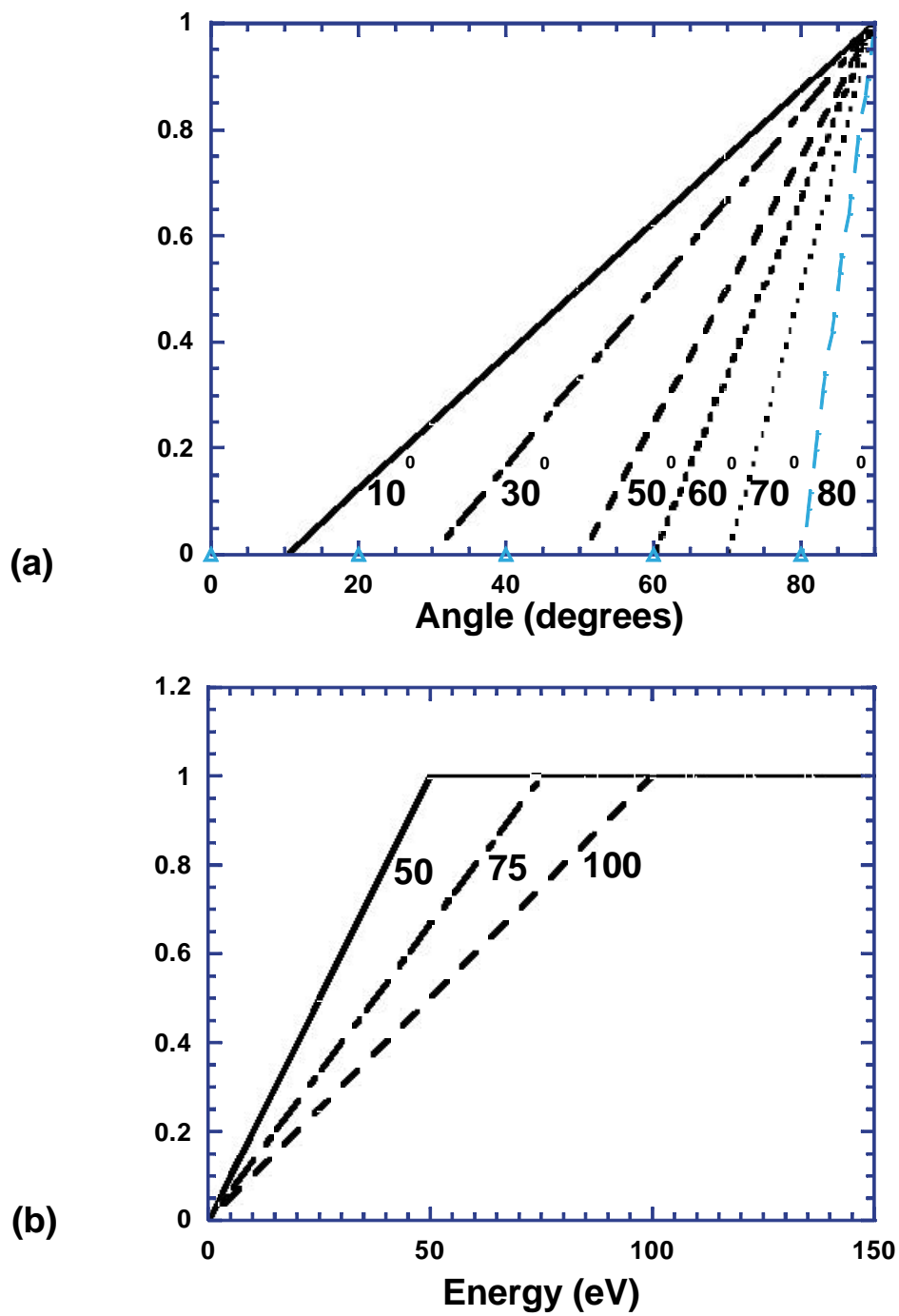


Fig 5.7. Specular reflection energy dependence on incoming (a) angle and (b) energy.

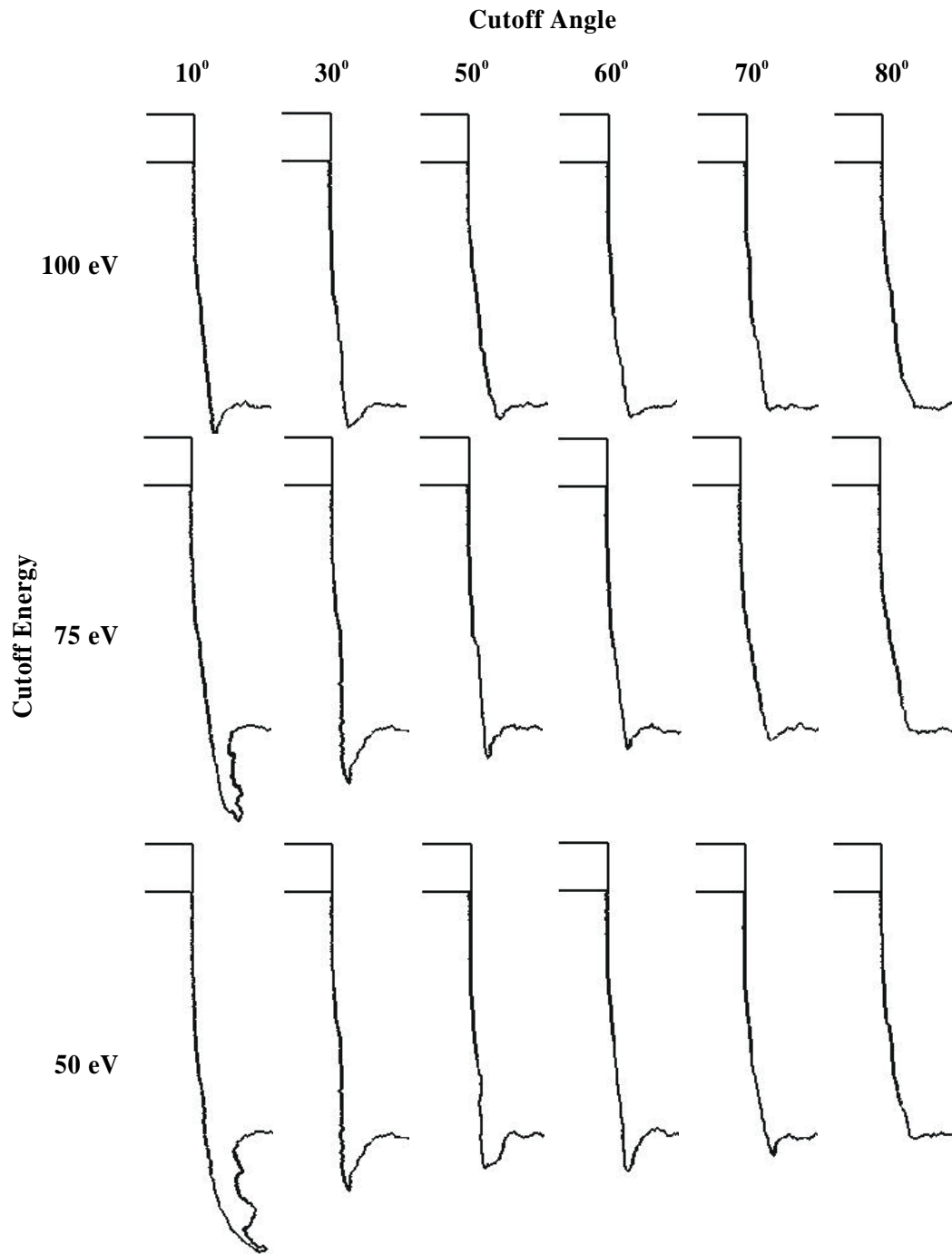


Fig. 5.8. The effects of cutoff energy and angle for specular reflection on the development of microtrenching.

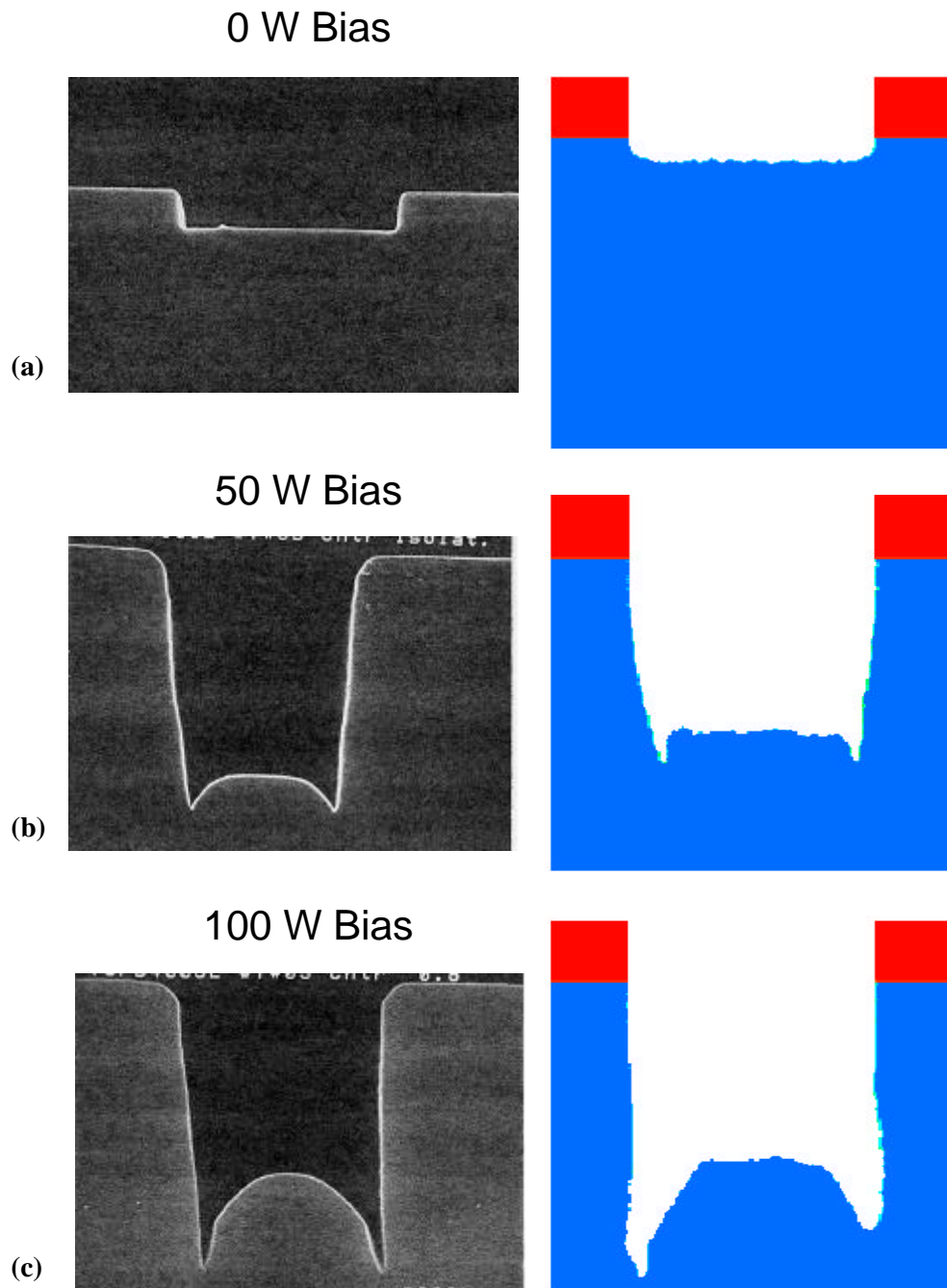


Fig. 5.9. Etch profile comparison of experimental SEMs with model results for (a) 0 W, (b) 50 W, and (c) 100 W RF bias.

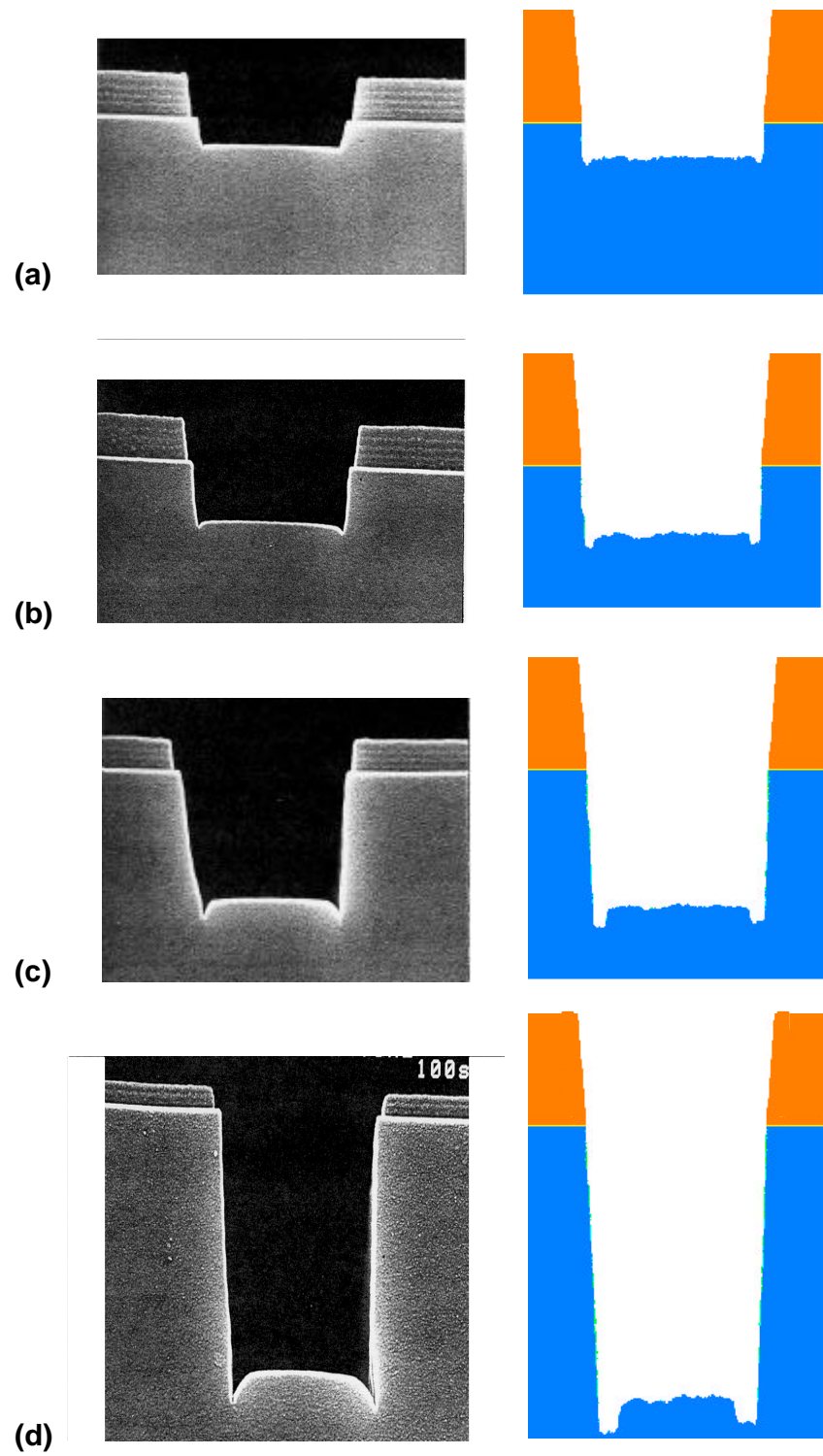


Fig. 5.10. Comparison of experimental SEMs to model results for 600-W ICP, 10-mTorr Cl_2 , and 50-W RF bias for (a) 10, (b) 20, (c) 40, and (d) 80-s etch time.

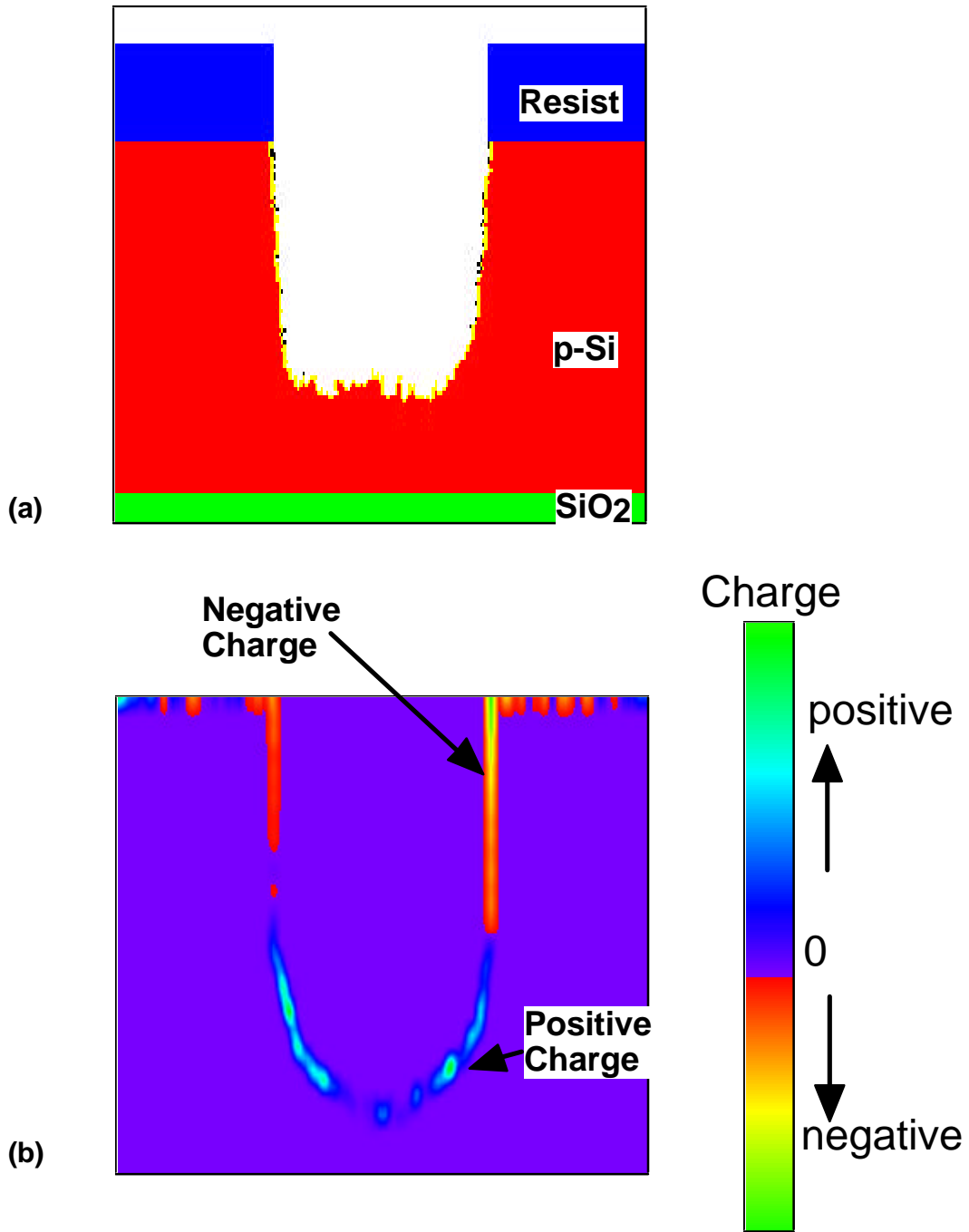


Fig. 5.11. (a) Etch profile with (b) surface charge distribution based on anisotropic ion and isotropic electron flux angular distributions.

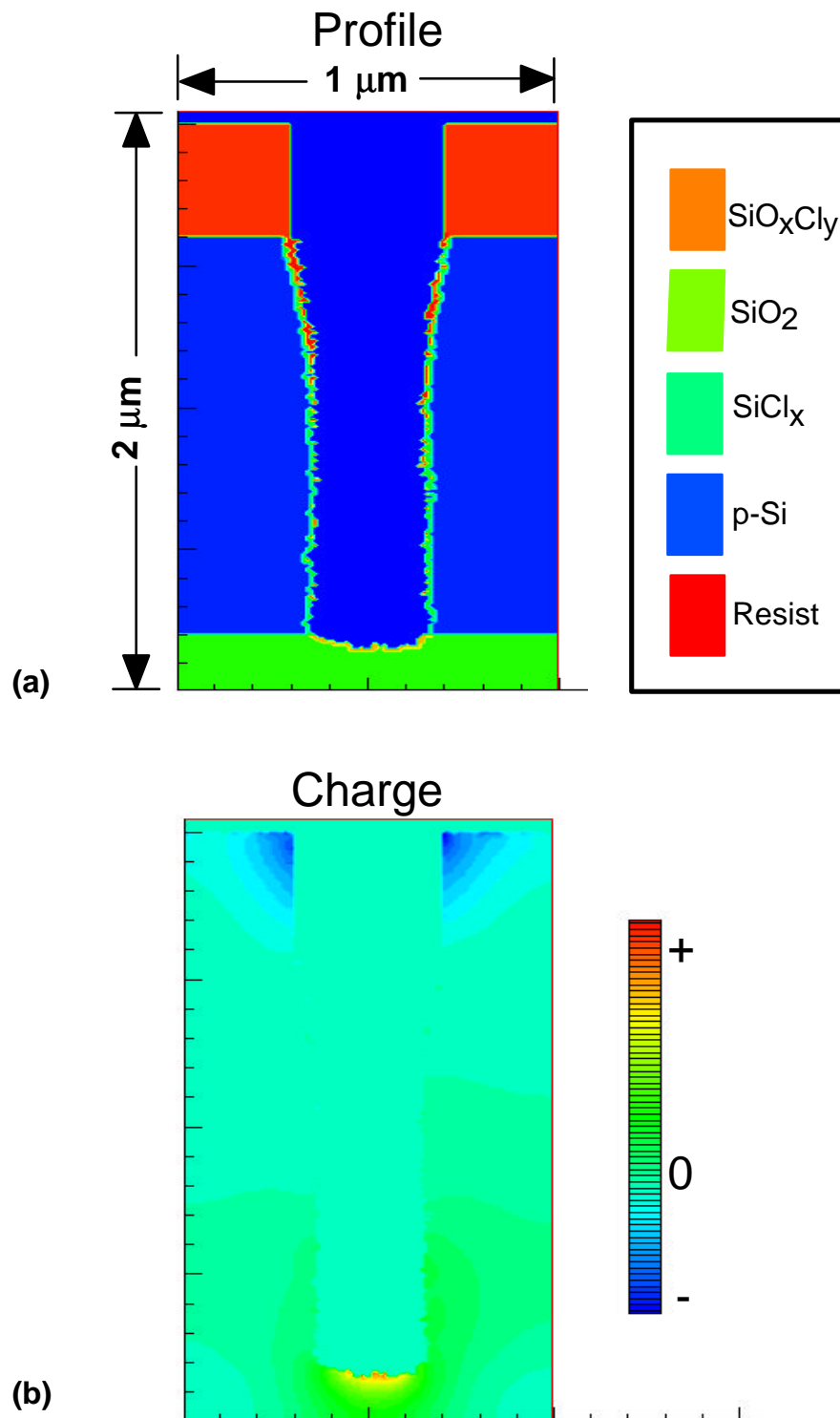


Fig. 5.12. (a) Etch profile and (b) charge distribution for self-consistent electric field solution and bulk diffusion of charge within material.

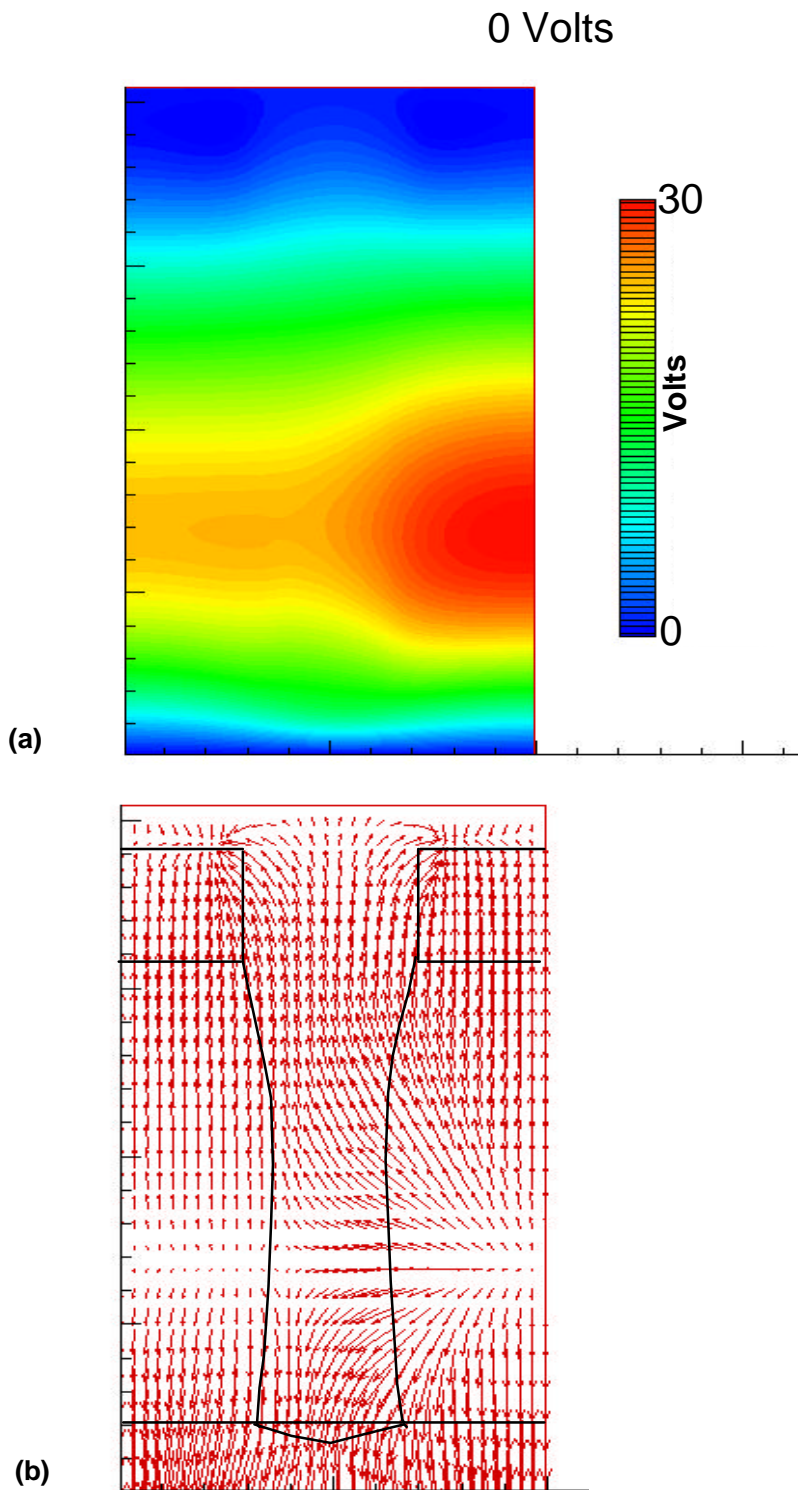


Fig. 5.13. (a) Potential distribution and (b) electric field for self-consistent solution of Poisson's equation and motion of charged species.

5.8. References

1. V. Singh, E. S. G. Shaqfeh, and J. P. McVittie, *J. Vac. Sci. Technol. B* **12**, 2952 (1994).
2. B. Abraham-Strauner, B. and W. Chen, *J. Vac. Sci. Technol. B* **14**, 3492 (1997).
3. N. Hamaguchi and S. M. Rossnagel, *J. Vac. Sci. Technol. B* **13**, 183 (1995).
4. B. A. Helmer and D. B. Graves, 44th Annual Symposium of the American Vacuum Society (San Jose, October 1997), paper PS-ThA10.
5. S. M. Rossnagel, C. Nichols, S. Hamaguchi, D. Ruzic, and R. Turkot, *J. Vac. Sci. Technol. B* **14**, 1819 (1996).
6. S. V. Nguyen., D. Dobuzinsky, S. Stiffler, and G. Chrisman, *J. Electrochem. Soc.* **138**, 1112 (1991).
7. T. J. Dalton, J. C. Arnold, H. H. Sawin, S. Swan, and D. Corliss, *J. Electrochem. Soc.* **140**, 2395 (1993).
8. J. Chang and H. H. Sawin, *J. Vac. Sci. Technol. A* **15**, 610 (1997).
9. D. E. Hanson, A. F. Voter, and J. D. Kress, *J. Appl. Phys.* **82**, 3552 (1997).
10. R. A. Gottscho, C. W. Jurgensen, and D. J. Vitkavage, *J. Vac. Sci. Technol. B* **10**, 2133 (1992).

6. THREE-DIMENSIONAL FEATURE PROFILE EVOLUTION

6.1. Introduction

The development of 2-dimensional (2D) profile simulators to investigate fabrication of microelectronics features during plasma etching has rapidly progressed during recent years.¹⁻³ An increasing sophistication in both the algorithms and physical phenomena captured in these models has enabled their application to a wide range of processes. For example, 2D profile simulators have been applied to analysis of overhang structures to determine reactive sticking coefficients of radicals,² micro-trenching,⁴ ionized metal physical vapor deposition,⁵ analysis of radical beam experiments,⁶ and silicon dioxide deposition from TEOS.⁷ A limited number of 3-dimensional (3D) plasma etch profile models have also been reported.⁸ As expected, 3D models using analytic methods such as string methods are more computationally intensive than 2D models, due in part to the need to repeatedly generate view-factors of incoming plasma species to points along an evolving 3D surface. This requirement is somewhat relaxed by using Monte Carlo simulators in which view-angle factors are not explicitly calculated. However, the computational burden of 3D Monte Carlo models increases from $O(n^2)$ to $O(n^3)$ as compared to 2D models. As a result, using either method, one is motivated to use 2D models whenever possible and apply or extrapolate the results to 3D structures.

Clearly, 2D models are adequate for analyzing long trenches which have an inherently 2D character or for analyzing 3D features which have advantageous symmetry, such as circular vias. However, a quantitative assessment of the appropriateness of extrapolating profiles obtained with 2D simulators to represent 3D features of finite length has not been made in any general fashion. This assessment is particularly important with regard to the use of profile models to analyze the fabrication of finite-length 3D features as may be used in, for example, shallow isolation trenches (SIT). In this chapter, we

discuss results from a study in which a newly developed 3D Monte Carlo (MC) based profile simulator has been used to investigate etch profiles for short trenches produced in polysilicon. These results are compared to profiles obtained with a 2D simulator using identical algorithms to determine under what conditions the 3D representation is required. The study is performed using an integrated model which combines a comprehensive plasma equipment simulator with the MC feature profile model. The purpose of this study is to both investigate the properties of etching 3D features and to make an assessment of when results from 2D simulators can be extrapolated to 3D features. Both the asymmetry and the angular spread of the ion flux distributions are examined to determine their effect on profile evolution and the 3D nature of the feature. The role of redeposited etch products is also examined for these conditions.

6.2. Description of the Three-Dimensional Model

The modeling hierarchy employed in this study has been previously described in Chapter 4 and only the changes to implement the 3D capability will be mentioned here.

The 3D version applied to this study is essentially identical to the 2D model with respect to algorithms and methodology. The Monte Carlo method, as opposed to semi-analytic methods, was chosen for this due to the ease of implementing surface reaction mechanisms of user-defined complexity and which are energy dependent. The MC method also eliminates the need for computing view factors of incoming species since the trajectories of reactants and products, the flux to a point on the surface, and the advance of the surface are statistically determined.

The MC-FPM(3D) resolves the trench region on the wafer (mask and semiconductor) in 3D using a rectilinear mesh. The mesh spacing is typically 200-500 cells for 1- μm length. Each computational cell is therefore as small as 10 atoms on a side. Each cell is assigned a material identity (e.g., polysilicon, photoresist, SiO_2 , plasma) which

may change during the simulation. Gas phase species (i.e., radicals and ions) are represented by computational pseudoparticles. Solid species, including adsorbates or passivation, are represented by the identity of the computational cell. The MC-FPM begins by launching pseudoparticles representing radicals and ions towards the surface with initial trajectories (energy and angle) randomly chosen from the PEDs and PADs provided by the Plasma Chemistry Monte Carlo Model (PCMCM). The pseudoparticles are launched with a frequency computed from the total flux of radicals or ions incident onto the substrate so that each pseudoparticle represents approximately the number of solid atoms in a single computational cell. The effects of surface charging on the profile evolution, an option in the model, are not addressed here since we are primarily interested in etching of fairly conductive materials.

6.3. Profiles for Finite-Length Three-Dimensional Etch Features

The test-feature for this study is an 0.8-*mm*-long by 0.4-*mm*-wide trench having a 0.3-*mm*-thick hard mask. The plasma tool is an inductively coupled plasma (ICP) reactor operating at 10 mTorr of Cl₂, 800 W of inductively coupled power with a 150-V bias (13.56 MHz) on the substrate. The total positive ion flux to the wafer, composed of Cl₂⁺ and Cl⁺, is $4.2 \times 10^{15} \text{ cm}^{-2}\text{s}^{-1}$, while the Cl atom flux is $3.1 \times 10^{18} \text{ cm}^{-2}\text{s}^{-1}$. The first etch profiles will be examined using the perturbed ion energy and angular distribution (IEAD) shown in Fig. 6.1(a). The IEAD has an angular spread of $\sim 3^\circ$ and an asymmetry of $\sim 3^\circ$ produced by an electrically interfering subwafer structure.⁹ This asymmetric IEAD was purposely chosen so that significant over-etching would be required to clear the feature and so the effects being discussed here would be emphasized. The angular asymmetry shown in Fig. 6.1(a) is in the plane perpendicular to the long axis of the trench. The angular distribution in the direction of the long axis is symmetric with a spread of $\sim 3^\circ$.

The etch profile obtained with the 2D model for the asymmetric IEAD is shown in Fig. 6.1(b) for 150 s of etch time. The average etch rate to the time at which the first point on the bottom of the trench is cleared is $4000 \text{ \AA}\cdot\text{min}^{-1}$. At this time, the profile has generally smooth walls with a small slant, approximately 6° , due to the asymmetry in the ion flux. As a result of this asymmetry, the entire bottom of the trench is not simultaneously cleared. An over-etch of 15% is required to completely clear the entire bottom of the trench

Two-dimensional “slices” through the structure in planes perpendicular to the long axis of the trench as predicted by the 3D model are shown in Figs. 6.2(b) and 6.3(a). The locations of these 2D slices (slices 4, 5, and 6) are indicated by the schematic in Fig. 6.2(a). Two-dimensional slices through the structure in planes perpendicular to the short axis of the trench (slices 1, 2, and 3) are shown in Fig. 6.2(c). The etch profile perpendicular to the long axis at the center of the trench (Profile 4, Fig. 6.2(b)) is similar to that predicted by the 2D model. There is, however, somewhat greater bowing of the sidewalls in the profile from the 3D model, indicating an increased sensitivity to the asymmetric IAD. This result suggests that at this location (0.4 μm from the ends of the trench), there are few 3D perturbations produced by the finite length of the trench and, to first order, the 2D model can produce acceptable profiles. Although the profiles are similar, 175 s were required to fully clear the floor of the trench to the oxide underlayer using the 3D model while only 150 s were required using the 2D model. The longer etch time predicted by the 3D model is caused by lower chlorination of the Si surface due to the reduced fluxes of Cl atoms which arrive isotropically at the surface and are shadowed by the ends of the trench.

The effect of the angular asymmetry of the IAD can be more clearly seen in the etch profiles parallel to the long axis of the trench as shown in Fig. 6.2(c). The locations of these profiles are noted in Fig. 6.2(a). Near the “shadowed” side of the trench (Profile 1),

the profile has not fully cleared, whereas near the “unshadowed” side of the trench (Profile 3), the trench has fully cleared and etching of the oxide has begun. The curvature of the profiles at the base of the endwalls is noticeably larger than the curvature at the base of the transverse trench (Profile 1) sidewalls. This disparity is due to the 3D shadowing which is most severe near the ends of the trench near the three-plane corners.

Transverse etch profiles obtained with the 3D are also shown in Fig. 6.3(a) for locations $0.1\ \mu\text{m}$ (Profile 5) and $0.05\ \text{mm}$ (Profile 6) from the end of the feature. Near the edge of the trench, the profile is dramatically underetched, even after a 30% overetch relative to the center of the trench which is fully cleared. There is also a larger side-to-side overetch requirement due to the asymmetry in the IAD. This asymmetry produces a lower etch rate on the side of the trench which is more severely shadowed. Within $0.1\ \text{mm}$ from the endwall, the profiles predicted by the 3D model significantly deviate from those predicted by the 2D model. Shadowing of the IAD in the three-plane corners, which reduces the ion and radical flux, is largely responsible. Proximity to the 3D corners is therefore a measure of the appropriateness of the 2D model.

The importance of the proximity to the three-plane corners for assessing the validity of 2D simulators is shown in Fig. 6.3(b). The normalized widths of the trench at the oxide layer after 175 s of etching are plotted for $0.4\text{-}\mu\text{m} \times 0.8\text{-}\mu\text{m}$ and $0.6\text{-}\mu\text{m} \times 0.8\text{-}\mu\text{m}$ features. (The normalized width is the exposed width of the oxide at the bottom of the trench divided by the width of the mask opening.) The proximity of the three-plane corners is commensurably higher for the $0.4\text{-}\mu\text{m}$ -wide trench than for the $0.6\text{-}\mu\text{m}$ -wide trench. The narrower aspect ratio trench has both a slower etch rate and clears the trench bottom for a smaller fraction of its length along the long axis. It is also more sensitive to the side-to-side asymmetry in the IEAD. These effects are due to the proximity of the three-plane corners and their shadowing of reactants.

An extreme case of proximity of three-plane corners is a square via. For example, profiles of a square 0.4- μm via hole etched for 175 s produced by the 3D model are shown in Fig. 6.4. These profiles clearly exhibit the consequences of three-plane corner shadowing. There is significant tapering of the feature produced by the nearness of 3D plane corners. The asymmetry of the IEAD produces an asymmetry in the profile which is magnified by the proximity of the three-plane corners compared to the longer aspect ratio trenches. These effects result in requiring longer over-etch times (>30%) than would be predicted by the 2D model. The horizontal plane views shown in Fig. 6.4(b) demonstrate the increasing consequences of the finite 3D nature of the feature resulting from the asymmetry of the IEAD as the feature increases in depth.

6.4. Ion Angular Distribution Effects for Finite Length Trenches

In the previous simulations, an IEAD having a $\sim 3^\circ$ angular spread and an off-axis asymmetry was used to demonstrate 3D effects on the etch profiles of finite length trenches. To systematically examine the consequences of the angular distribution on the evolution of these finite-length trenches, a symmetric IEAD from an unperturbed location on the substrate was used as a base distribution. The IEAD, in addition to having a symmetric angular distribution, has a slightly higher maximum energy of 100 eV, but still retains the $\pm 3^\circ$ angular spread. The effects of a narrowing or broadening the angular spread of the IEAD on the 3D etch profile were examined by adjusting this distribution to have an angular spread of $\pm 1.5^\circ$ and $\pm 6^\circ$. These three IEADs are then used with the MC-FPM to simulate the etching of a 0.6- $\mu\text{m} \times 0.8\text{-}\mu\text{m}$ feature.

Etch profiles perpendicular to the long axis of the trench (locations 4, 5, and 6 of Fig. 6.2(a) are shown in Fig. 6.6 for the $\pm 1.5^\circ$, $\pm 3^\circ$, and $\pm 6^\circ$ IEADs. Profiles in the center of the trench along the long axis are shown in Fig. 6.5. Etching was performed until initial contact with the oxide layer. For the 1.5° IEAD, there is a large difference in etch rate

between the center of the profile and near the end of the where the depth is only 80% the depth of the center. This difference can be attributed to the inward slope of the feature sidewall as shown in Fig. 6.5(a). A strongly contributing factor is the redeposition of SiCl_x on the sidewalls with a sticking coefficient of 0.30^{10} as well as the very narrow angular distribution. The sidewall encroaches on the feature, causing the regions near the sidewalls to be underetched. For the 3° IEAD feature, as well as the 6° IEAD feature, the sidewalls encroach less on the trench reducing the differential etch rate between the ends and the center of the feature. The 3° IEAD feature shows an etch rate near the feature ends which is 92% that of the center, while the etch ratio for the 6° IEAD feature is 95%. The effect can be seen in Fig. 6.5 from the decrease in slope of the bottom of the feature from the center to the ends when the angular distribution is broadened.

However, there is also a difference in average trench etch rate due to the changes in the angular distribution. As the angular distribution is broadened, the effects of the width-to-depth aspect ratio have a greater impact on the etch rate of the feature. In Fig. 6.7, the time evolution of the trench depth at the three locations shown in Fig 6.6 is shown. The 6° IEAD feature requires 190 s to reach the oxide while the 1.5° IEAD feature only requires 120 s. This is due to the greater shadowing effect on the 6° IEAD flux as the trench depth increases. The 3° IEAD feature maintains the best balance between overall feature conformity and etch rate, requiring 140 s to reach the oxide. The graphs in Fig. 6.7 also indicate the etch rate differential between the center and ends of the feature. The 6° IEAD feature depth as shown by Fig. 6.7(c) shows a uniform etch rate for all three locations throughout the etch process. The 3° IEAD feature depth progression indicates a small deviation from linear near the end due to the encroaching sidewall, while the 1.5° IEAD feature depth shows the greatest deviation near the feature end which produces an almost asymptotic behavior as the depth increases and the sidewall encroaches to a greater degree on the feature.

As mentioned previously, the sticking coefficient of SiCl_x plays an important role in trench formation. For a coefficient of 0.30 as experimentally shown by Chang *et al.*⁹ for a SiCl_2 beam on silicon, the deposition rate at the sidewalls produces an inward taper which could be exacerbated by other deposition fluxes in etching reactors such as redeposited resist material. Chang *et al.*⁹ also found that the presence of ion and radical fluxes at the surface could lower the sticking coefficient to as low as 0.05. When the sticking coefficient was decreased to 0.10, the sidewalls became almost vertical for even the $\pm 1.5^\circ$ IEAD shown in Fig. 6.8(a), and the difference in etch rate for center to edge decreases to $\sim 5\%$, indicating that the end wall no longer encroaches on the profile (Profile 6). For the $\pm 6^\circ$ IEAD, the profiles become deeply undercut and the differential etch rate is only a few percent.

6.5. Summary

In conclusion, we have compared predictions for etch profiles for finite length trenches obtained from 2D and 3D Monte Carlo simulators for particularly harsh conditions produced by both aspect ratio and asymmetry of the IAD. For the feature with an aspect ratio of 1:2:2.5 (0.4- μm wide, 0.8- μm long, and 1.0- μm deep), the 2D model produces transverse profiles very similar to the 3D model at the center of the long axis, though the 2D model overpredicts the etch rate by approximately 20% due to the lack of large-angle shadowing by the endwalls. The transverse profiles from the 3D model within 0.1 μm of the endwall differ significantly from those of the 2D model. There is more rounding of the corners produced by shading at the three-plane corners and reduced etch rates, thereby requiring longer overetch times than would be predicted by the 2D model. This is particularly evident in profiles parallel to the long axis. As the aspect ratio of the mask opening increases to that of a square via, the shadowing at the three-plane corners overlaps, producing a tapered feature with a fully rounded bottom. Profiles obtained from

2D models for these structures should be scrutinized. The role of the angular spread of the IEAD was also examined. It was found for narrow angular distributions (average angle $<3^\circ$) that the inward taper of the sidewalls at the narrow ends produced a strong differential in etch rate between the ends and center of the feature. For broader distributions, the sidewalls do not encroach on the feature and maintain a more uniform etch rate across the bottom of the feature. This result was dependent on the rate of redeposition of SiCl_x on the sidewalls. As this sticking coefficient was lowered, the angular spread could be reduced without inducing the inward taper of side and end walls. These results indicate that the sidewall slope and corner curvature as well as the differential etch rate over the feature bottom are dependent on the 3D aspect ratio of the feature as well as on the angular spread of the IEAD and the redeposition rate of etch species.

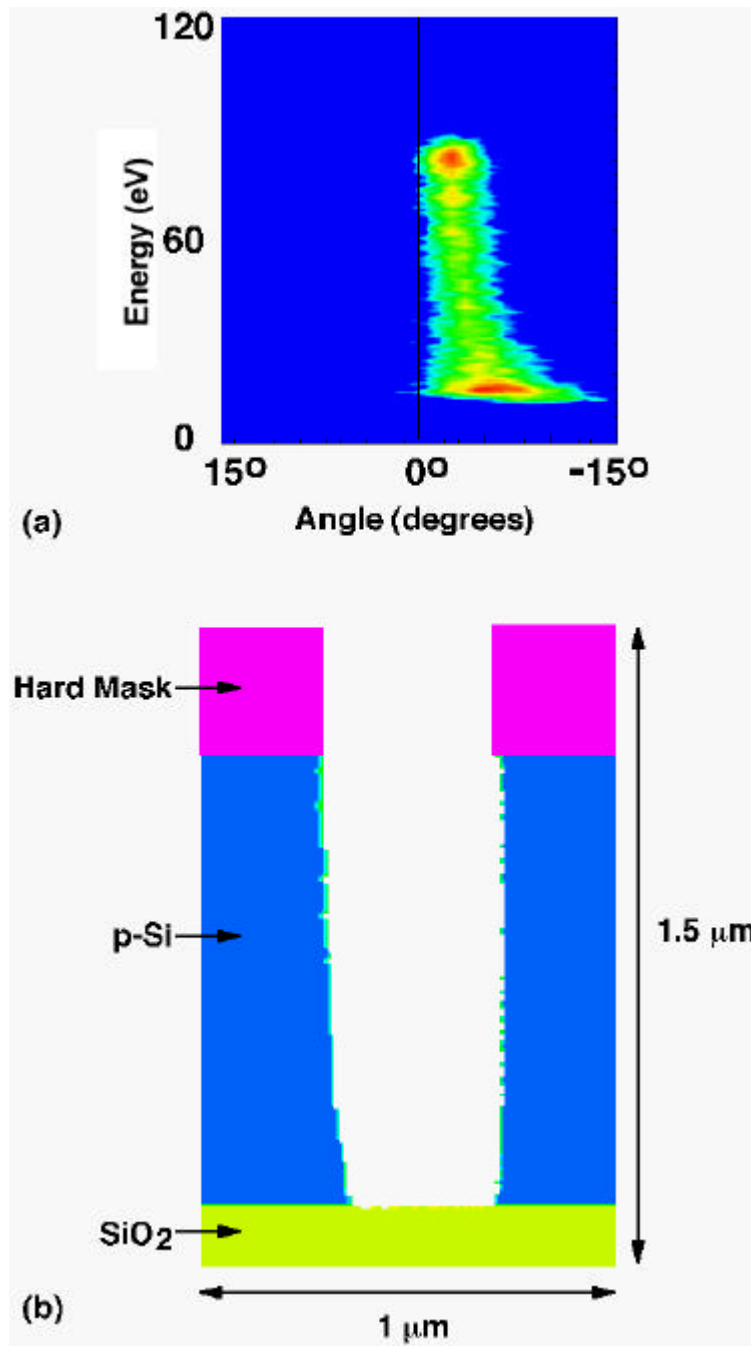


Fig. 6.1. Ion distribution and 2D profile. (a) Ion energy and angular distribution for an ICP reactor obtained with the HPEM and PCMCM. The operating conditions are 10 mTorr, 100-sccm Cl_2 , 800-W ICP, and 150-V chuck bias at 13.56 MHz. (b) Etch profile obtained with the 2D simulator for an infinitely long trench in polysilicon. The mask opening is 0.4 mm. The shading on the walls of the trench indicates chlorinated surfaces (e.g., SiCl_n).

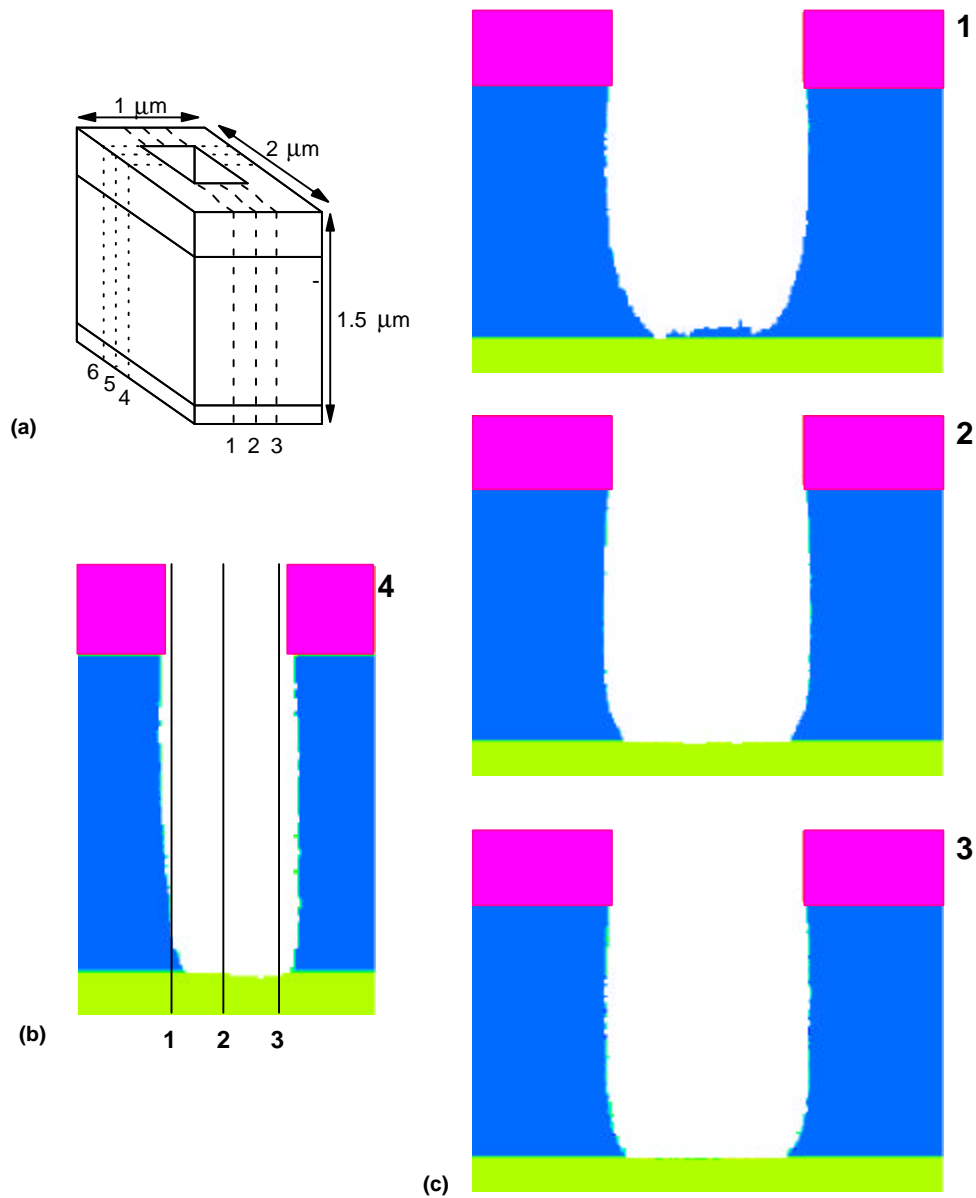


Fig. 6.2. Etch profiles obtained with the 3D model in 2D plane views of a $0.4\text{-}\mu\text{m} \times 0.8\text{-}\mu\text{m}$ long trench. (a) The schematic indicates the locations of the planes views (labeled 1-6). (b) Transverse plane profile perpendicular to the long axis of the trench after a 150 s etch at the center of the feature (location 4). (c) Axial plane profiles parallel to the long axis of the trench at the three locations (1, 2, and 3) indicated by the schematic. The asymmetry in the profile worsens and the etch rate decreases the end wall is approached.

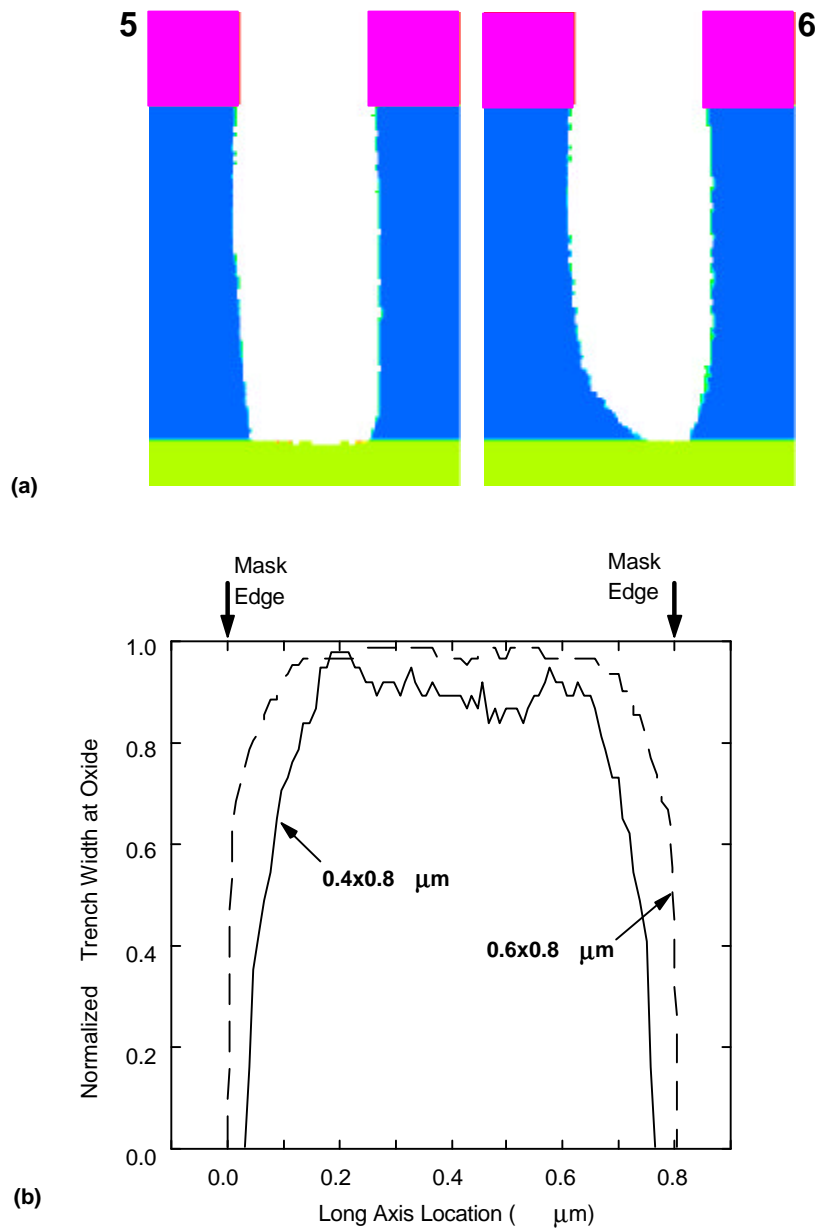


Fig. 6.3. (a) Transverse etch profiles obtained with the 3D model in planes perpendicular to the long axis of a $0.4\text{-}\mu\text{m} \times 0.8\text{-}\mu\text{m}$ long trench at locations 5 and 6 indicated in the schematic (Fig. 6.3(a)). (b) Relative trench width as a function of axial location for $0.4\text{-}\mu\text{m} \times 0.8\text{-}\mu\text{m}$ and $0.6\text{-}\mu\text{m} \times 0.8\text{-}\mu\text{m}$ trenches. The relative trench width is the width of the exposed oxide on the floor of the trench divided by the width of the mask opening. The narrower trench has lower etch rates near the endwalls due to the proximity of the “three-plane” corners.

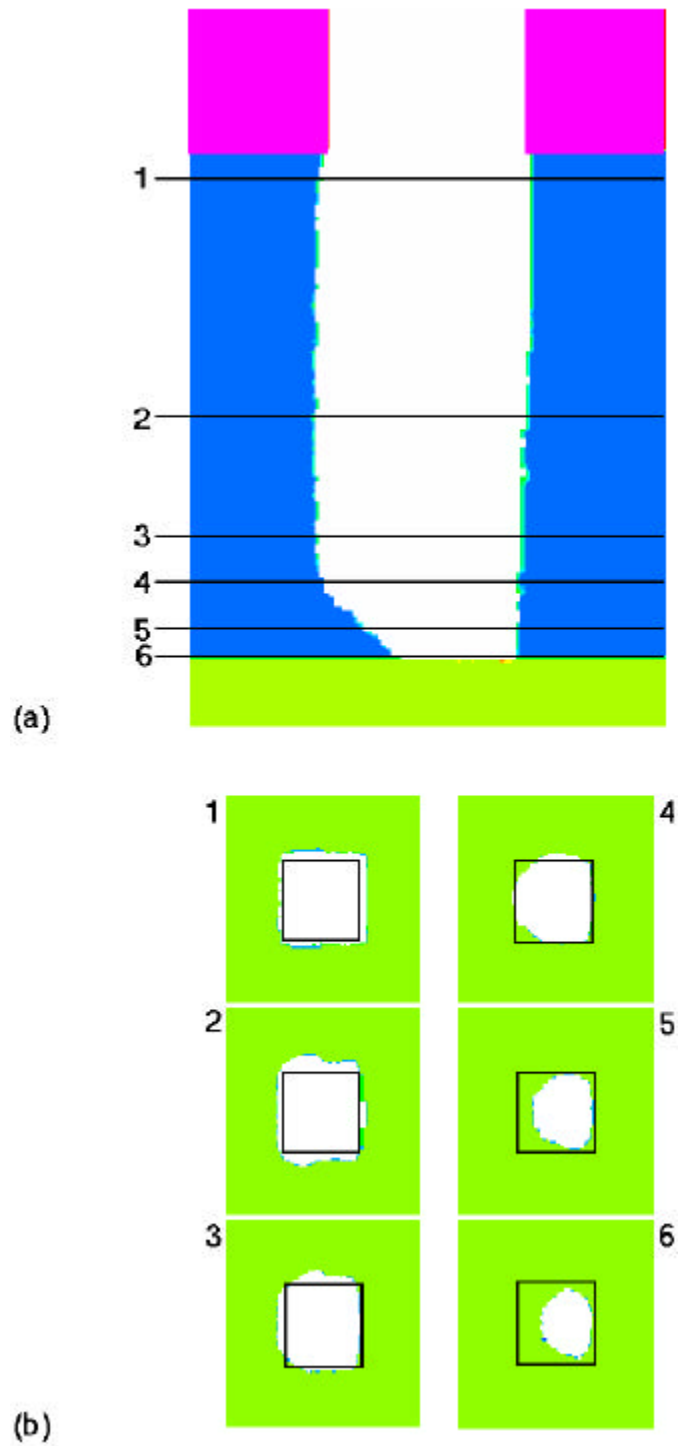


Fig. 6.4. Etch profiles for a square $0.4\text{-mm} \times 0.4\text{-mm}$ via. (a) Transverse etch profile in the plane of the asymmetry of the IEAD. (b) Horizontal slices at heights (locations 1-6) noted in the top figure indicate the increasing effects of the finite 3D nature of the feature and the asymmetric IEAD as the etch depth increases.

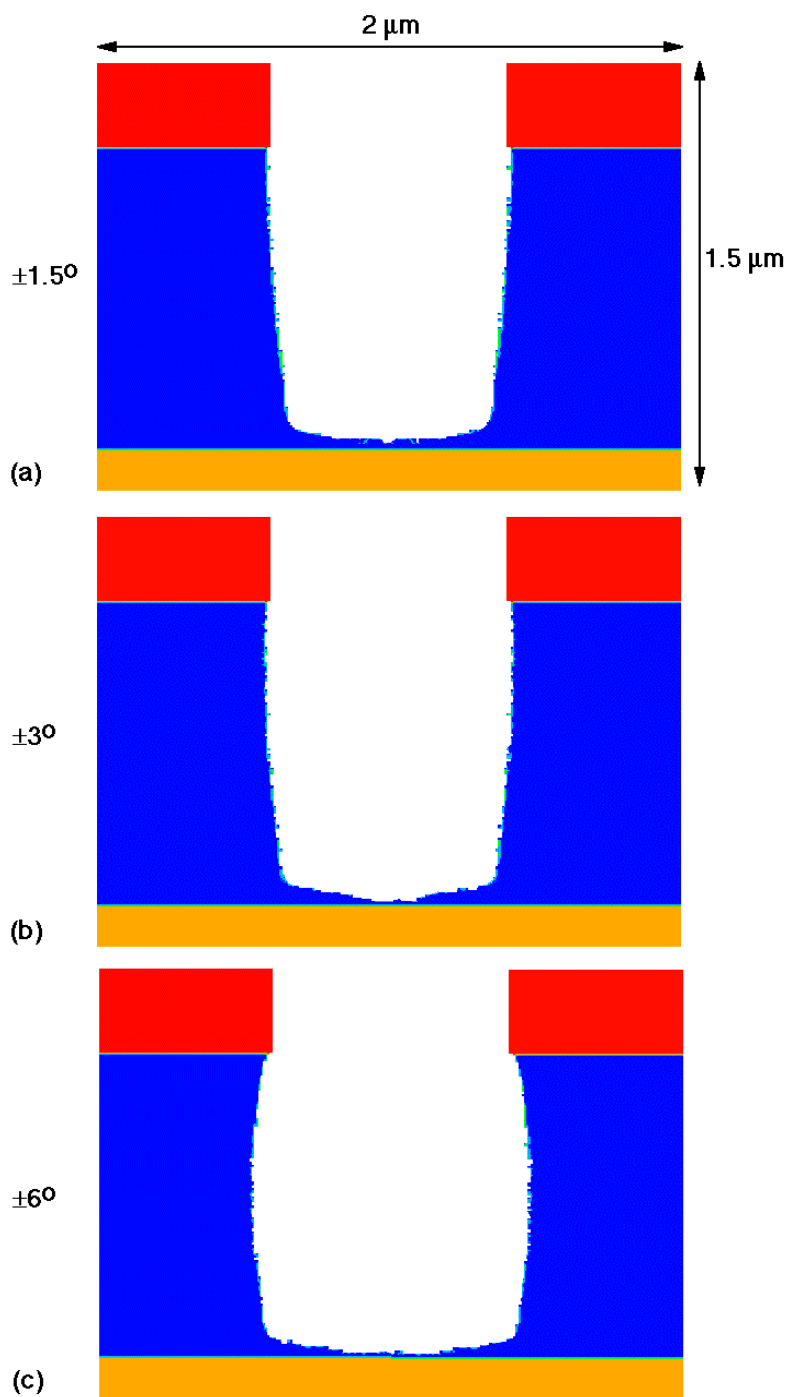


Fig. 6.5. 2D plane profiles perpendicular to the long axis of a $0.6\text{-}\mu\text{m} \times 0.8\text{-}\mu\text{m}$ long trench feature for three locations (4, 5, and 6) noted in Fig. 6.2(a). Three IEADs were used with average angular spreads of (a) 1.5° , (b) 3° , and (c) 6° . For the narrow IEAD, sidewall tapering leads to etch rate decrease near the ends of the feature as large as 20%. This is in part due to a sticking coefficient of 0.30 for redeposited SiCl_x .

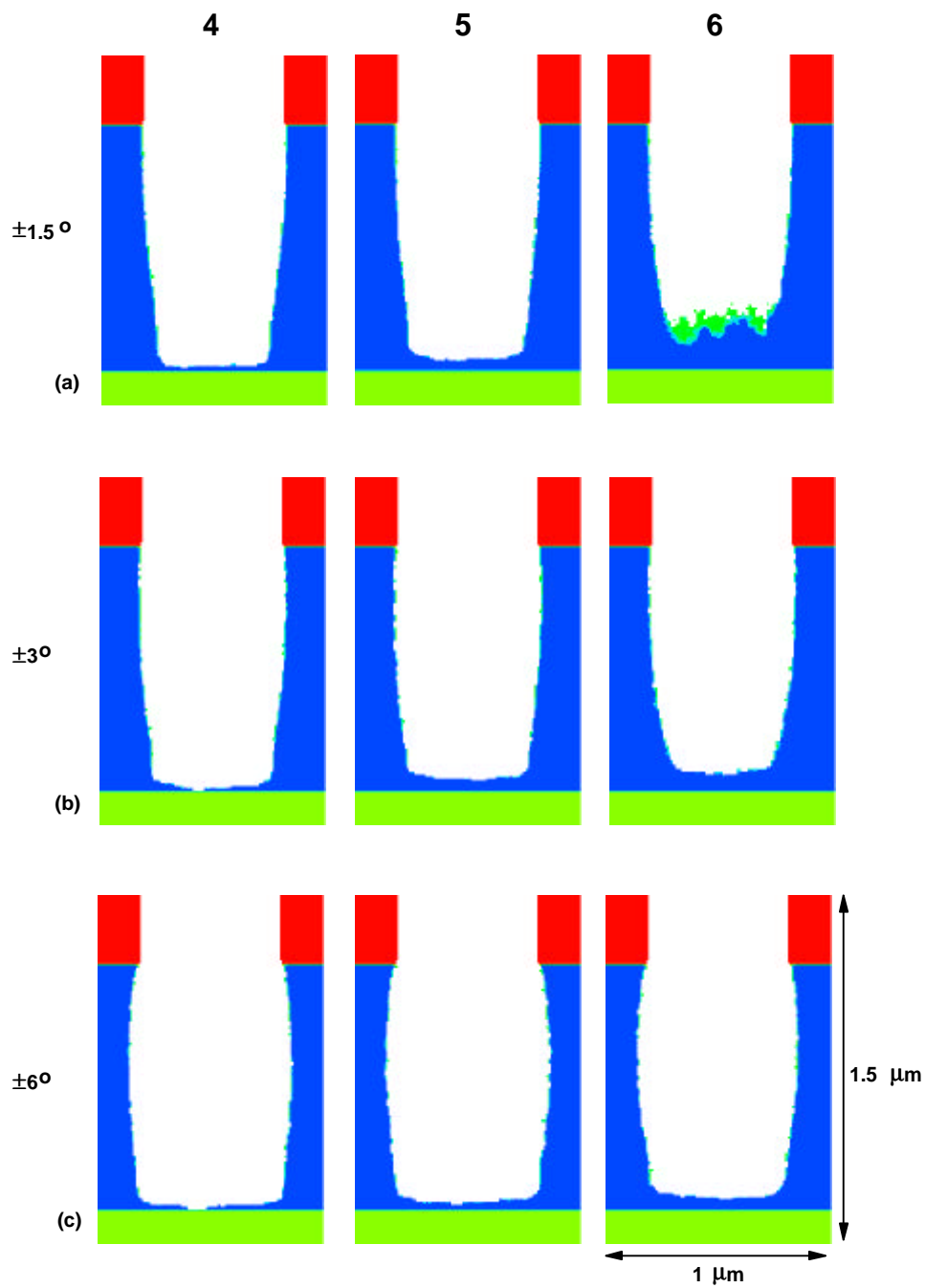


Fig. 6.6. 2D plane profiles parallel to the long axis of the trench and centered along the short axis of the feature for (a) 1.5° , (b) 3° , and (c) 6° angular spread IEADs. The inward taper of the sidewall for the narrow distribution and its effect on the etch rate at the ends can be seen.

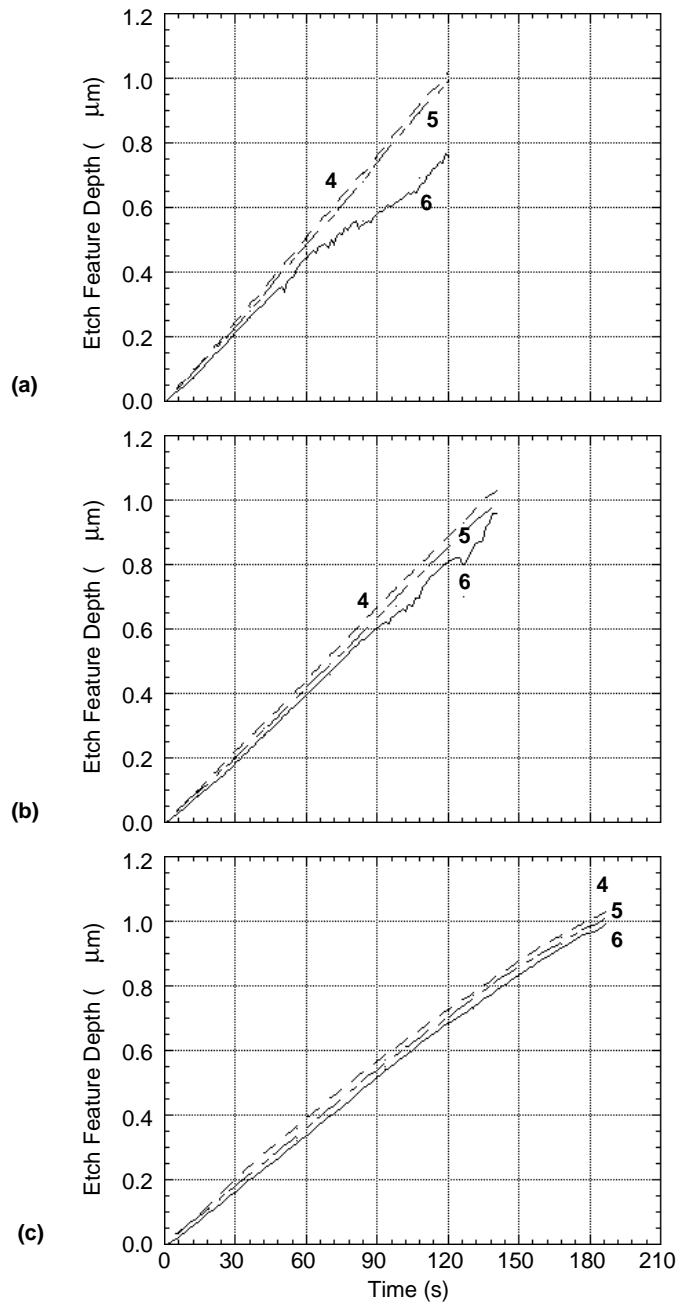


Fig. 6.7. Time evolution of the trench profile depth at the three transverse locations (4, 5, and 6) shown in Fig. 6.2(a) for (a) 1.5°, (b) 3°, and (c) 6° angular spread IEADs. While locations 4 and 5 show a linear etch progress, location 6 for the narrow IEAD shows a decrease in rate. The overall etch rate can also be seen to be inversely dependent on the angular spread of the incoming IEAD.

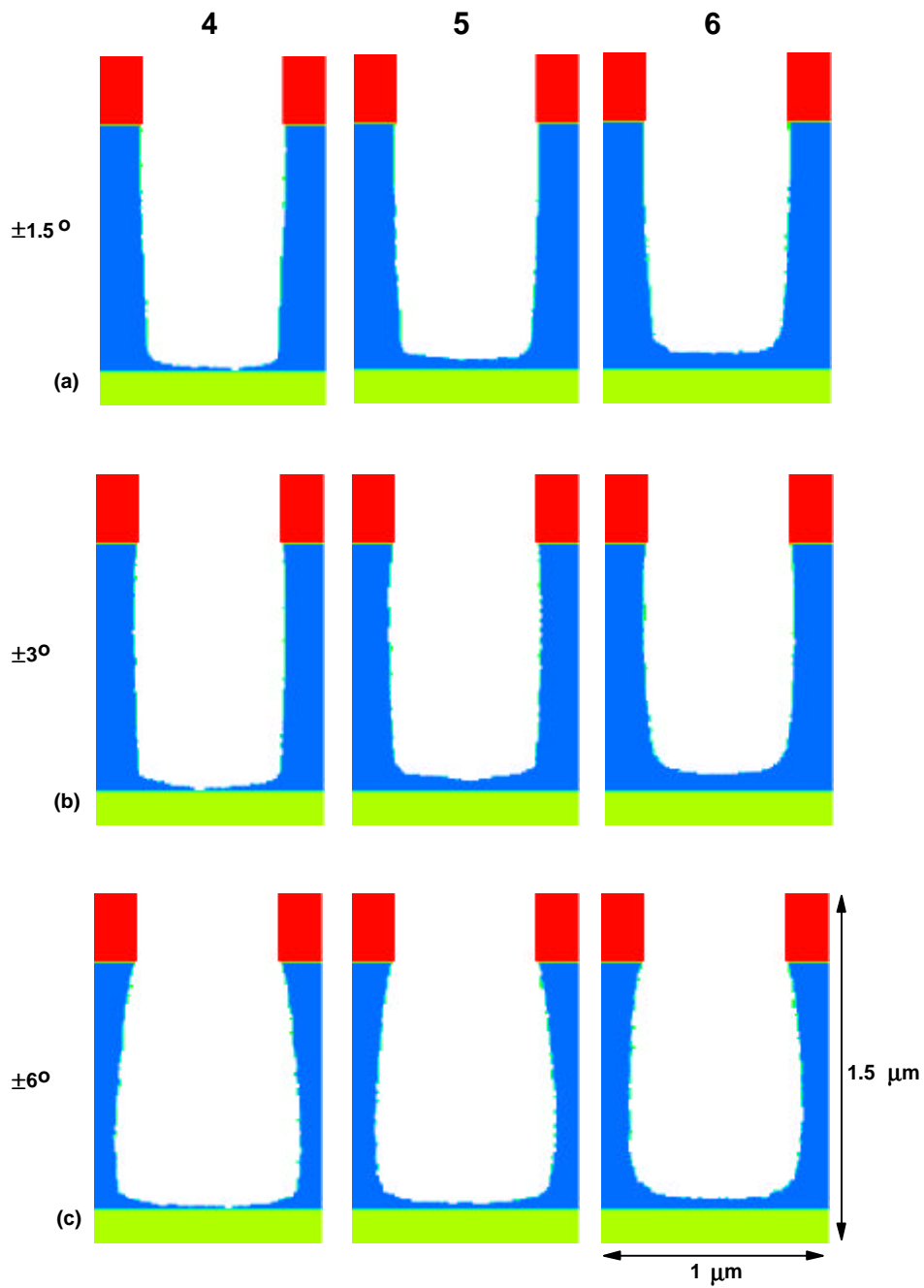


Fig. 6.8. 2D plane profiles perpendicular to the long axis of a $0.6\text{-}\mu\text{m} \times 0.8\text{-}\mu\text{m}$ long trench feature for three locations (4, 5, and 6) noted in Fig 6.2(a). Three IEADs were used with average angular spreads of (a) 1.5° , (b) 3° , and (c) 6° . A sticking coefficient of 0.10 was used for redeposited SiCl_x leading to broadened profiles.

6.6. References

1. S. Hamaguchi and M. Dalvie, *J. Vac. Sci. Technol. A* **12**, 2745 (1994).
2. V. K. Singh, E. S. G. Shaqfeh, and J. P. McVittie, *J. Vac. Sci. Technol. B* **12**, 2952 (1994).
3. B. Abraham-Strauner and W. Chen, *J. Vac. Sci. Technol. B* **14**, 3492 (1997).
4. T. J. Dalton, J. C. Arnold, H. H. Sawin, S. Swan, and D. Corliss, *J. Electrochem. Soc.* **140**, 2395 (1993).
5. S. Hamaguchi and S. M. Rossnagel, *J. Vac. Sci. Technol. B* **13**, 183 (1995).
6. J. P. Chang and H. H. Sawin, *J. Vac. Sci. Technol. A* **15**, 610 (1997).
7. M. Virmani, D. A. Levedakis, G. B. Raupp, and T. S. Cale, *J. Vac. Sci. Technol. A* **14**, 977 (1996).
8. Z. K. Hsiau, E. C. Kan, J. P. McVittie, and R. W. Dutton, *IEEE Trans. Elec. Dev.*, **44**, 1375 (1997).
9. J. P. Chang, A. P. Mahorowala, and H. H. Sawin, *J. Vac. Sci. Technol. A* **16**, 217 (1998).

7. CONCLUSIONS

Plasma etching using high-density plasma (HDP) reactors is becoming predominant in the semiconductor fabrication industry due to its capability to produce highly anisotropic features at current and future linewidths (0.5 to 0.17 μm). The Computational Optical and Discharge Physics Group (CODPG) has developed a modularized computational simulation, Hybrid Plasma Equipment Model (HPEM), to examine these systems. Two offline modules have been developed, the Plasma Chemistry Monte Carlo Model (PCMCM) and the Monte Carlo Feature Profile Model (MC-FPM), to focus on the effect of the plasma on the wafer surface. Using the output from the main plasma simulation, the PCMCM self-consistently determines the energy and angular distributions of all plasma species at the wafer. This distribution information can then be used by the MC-FPM to determine the time evolution of etch features on the wafer based on an energy- and angular-dependent surface chemistry. This chemistry has been developed using experimental results by other researchers as described in this paper. Through initial calibration of these reaction mechanisms, a predictive capability for chlorine etching of polysilicon has been developed starting from reactor parameters such as pressure, power, and geometry to produce the resulting etch profile evolution.

The PCMCM was developed for earlier research and has been utilized to determine the energy and angular flux distributions on plasma species fluxes impinging on the wafer surface. Specifically, chlorine plasmas were examined producing broad ion-energy distributions and narrow angular distributions which were utilized to determine the radially dependent etch rates on the wafer.

The MC-FPM is a Monte Carlo-based simulation for surface evolution in plasma processing systems. The initial use of the MC-FPM has been in the examination of chlorine etching of silicon as used in semiconductor manufacturing processes with inductively coupled reactors. A generalized reaction scheme was used to allow flexibility

in reaction process integration. The effects of superwafer and subwafer topography such as wafer chucks and backside cooling channels were examined indicating large perturbation of the incoming ion flux distributions and producing large asymmetries in the resulting trench etch profiles. For an insulating wafer, the subwafer dielectric capacitively depleted the sheath potential, leading to perturbation of the etch profile. However, for conductive wafers, the effects of the subwafer electrical properties are masked and the etch profiles show little to no effect.

Microtrench formation in chlorine etching of silicon affects the viability of fabricated devices due to oxide “punch-through” and increases in overetch times. Two important factors in the formation of microtrenching are the angular dependence of etch yield for ion-enhanced etching and specular reflection of grazing angle ions. Experimental results have shown that ion-enhanced etching of silicon may not have the same angular dependence as physical sputtering. Simulations indicate that the most important aspect of the angular dependence is the drop-off at grazing angles, which leads to inward tapering of sidewalls. Little is known about the energy or angular dependence of ion specular reflection. Parameterization of these dependencies indicates that the maximum angle for specular reflection should be between 50° and 60° of surface normal to produce the expected microtrenching. The cutoff energy for specular reflection was found to be less than or equal to 50 eV to produce the expected depth of microtrenches. Comparison to experiment indicates that the MC-FPM is capable of predicting etch profiles for standard process parameters in an inductively coupled plasma reactor. For variation of bias power, the model shows reasonable agreement diverging at higher powers with respect to microtrench depth. The model matches experiment well for the time evolution of profile. Initial examination of the effects of nonuniform surface charging was also pursued. The high-energy ion flux verses the isotropic thermal electron flux leads to negative charging of the upper corners of the profile and positive charging of the bottom. This leads to

electric fields which perturb the charged species motion near the feature and the resulting shape of the profile.

The MC-FPM was also extended to simulate the etching of 3D features such as via holes or finite-length trenches. For finite-length trenches, the differences in results produced by the 2D and 3D models were determined. Near the ends of the finite trench, large deviations from the 2D profile were found. The shadowing of the nearby endwall leads to greater corner rounding and a decrease in the relative etch rate, necessitating longer overetch rates. The effects of sidewall taper due to passivator deposition indicate that for small fluxes of passivator, the sidewalls and corners are vertical or undercut, while for moderate fluxes the resulting inward taper of the endwall encroaches on the feature, leading to greater differences in the relative etch rates across the trench bottom.

Physically based numerical modeling of plasma processing has improved to allow prediction of both plasma conditions and the resulting surface effects, most importantly the evolution of features on the wafer. It has been demonstrated that the HPEM, together with the PCMCM and the MC-FPM, is capable of generating etch feature information from reactor parameters including geometry, pressure, power, and flow for chlorine etching of silicon in an inductively coupled plasma reactor. Due to the generalized, physically based character of these coupled models, they should be capable of modeling many plasma processing systems from “cradle to grave” and only lack the complete chemistries for these systems.

VITA

Robert Hoekstra was born in Rockford, Illinois, in 1969. He attended the University of Illinois at Urbana-Champaign, where he received two B.S. degrees in May 1992. He also received his M.S. at the University of Illinois at Urbana-Champaign in January 1995. Under the direction of Professor Mark J. Kushner, he has studied the simulation of plasma processing equipment. His work has resulted in five reviewed papers and eleven conference presentations. He is a member of the American Vacuum Society, the American Physical Society, the Institute of Electrical and Electronics Engineers, the Materials Research Society, and the Electrochemical Society, as well the Tau Beta Pi and Phi Beta Kappa honor societies. In 1994, he received the Technical Excellence Award from the Semiconductor Research Corporation.